



**NIST Technical Note
NIST TN 2323**

Pre-conceptual Design Activities of the NIST Neutron Source

Preliminary Thermal-hydraulics Assessments

Abdullah G. Weiss
Anil Gurgun
Evan R. Bures
Joy S. Shen

This publication is available free of charge from:
<https://doi.org/10.6028/NIST.TN.2323>

**NIST Technical Note
NIST TN 2323**

Pre-conceptual Design Activities of the NIST Neutron Source

Preliminary Thermal-hydraulics Assessments

Abdullah G. Weiss

Anil Gurgen

Joy S. Shen

*Reactor Operations and Engineering
NIST Center for Neutron Research*

Evan R. Bures

Nuclear Engineering Department

Texas A&M University

This publication is available free of charge from:
<https://doi.org/10.6028/NIST.TN.2323>

February 2025



U.S. Department of Commerce
Jeremy Pelter, Acting Secretary of Commerce

National Institute of Standards and Technology
Craig Burkhardt, Acting Under Secretary of Commerce for Standards and Technology and Acting NIST Director

NIST TN 2323
February 2025

Certain commercial equipment, instruments, software, or materials, commercial or non-commercial, are identified in this paper in order to specify the experimental procedure adequately. Such identification does not imply recommendation or endorsement of any product or service by NIST, nor does it imply that the materials or equipment identified are necessarily the best available for the purpose.

NIST Technical Series Policies

[Copyright, Use, and Licensing Statements](#)

[NIST Technical Series Publication Identifier Syntax](#)

Publication History

Approved by the NIST Editorial Review Board on 2024-12-11.

How to Cite this NIST Technical Series Publication

Weiss AG, Gurgun A, Bures ER, Shen JS, (2025) Pre-conceptual Design Activities of the NIST Neutron Source: Preliminary Thermal-hydraulics Assessments. (National Institute of Standards and Technology, Gaithersburg, MD), NIST Technical Note (TN) NIST TN 2323. <https://doi.org/10.6028/NIST.TN.2323>

NIST Author ORCID iDs

Abdullah G. Weiss: 0000-0003-1134-1735

Anil Gurgun: 0000-0002-2304-8061

Joy S. Shen: 0009-0004-8046-8945

Contact Information

abdullah.weiss@nist.gov

anil.gurgun@nist.gov

joy.shen@nist.gov

Abstract

The NIST Neutron Source (NNS) is the proposed reactor for ensuring continued future availability of neutrons for the United States' scientific needs. The NNS would allow the aging National Bureau of Standards Reactor (NBSR) at the NIST Center for Neutron Research (NCNR) to be decommissioned without affecting the availability of neutrons in the United States. This work describes preliminary thermal-hydraulics assessments of the preconceptual design of the NNS, and the NNS's behavior during nominal operating conditions and various accident scenarios. Core-level and system-level analyses are conducted via models using the United States Nuclear Regulatory Commission's (NRC's) TRAC/RELAP Advanced Computational Engine (TRACE) code. The TRACE code allows for an adequate understanding of the thermal and hydraulic characteristics of the reactor and its components during various analyzed conditions. Safety analyses revealed that the proposed NNS operation maintains adequate margins to ONB, OFI, and CHF. In addition, accident analyses indicated that NNS remains within the safety criterion of blistering temperature throughout all analyzed conditions. Computational fluid dynamics (CFD) analyses revealed the opportunity for various design optimizations, including the design of the inlet to the reactor, the fuel assemblies, and the outlet to the reactor for improved performance and enhanced safety margins. The analyses in this work serve as a first step toward defining a holistic understanding of the thermal hydraulics in the NNS, and it provides a valuable reference for future design iterations.

Keywords

NCNR; NNS; Thermal; Hydraulics; TRACE; CFD; Reactor; Nuclear; Safety

Table of Contents

1. Introduction	1
1.1. Overview of the NNS Primary System and Relevant Geometric Details.....	3
2. Power Profiles	5
3. Methodology	7
3.1. Overview of TRACE.....	7
3.2. NNS TRACE Model	8
3.2.1. Core Nodalization.....	8
3.2.2. Reactor Coolant Pumps	10
3.2.3. Heat Exchangers.....	11
3.2.4. Flap Valves	11
3.2.5. Reactor Power.....	12
3.2.6. Reactor Protection System.....	12
3.3. Steady-State Analysis.....	14
3.4. Transient Analysis.....	15
3.5. Computing Safety Margins.....	16
3.5.1. Critical Heat Flux Ratio (CHFR).....	18
3.5.1.1. Mirshak (1959) Correlation	19
3.5.1.2. Updated Sudo-Kaminaga (1998) Correlations	19
3.5.2. Onset of Flow Instability Ratio (OFIR)	20
3.5.2.1. Costa (1969) Correlation	21
3.5.2.2. Saha-Zuber (1974) Correlation.....	21
3.5.3. Onset of Nucleate Boiling Ratio (ONBR)	21
3.5.3.1. Bergles-Rohsenow (1964) Correlation.....	21
3.6. CFD Models.....	22
3.6.1. Identifying Regions of Interest	22
3.6.2. Turbulence Modeling.....	24
3.6.2.1. General RANS Modeling Approach	24
3.6.2.2. Standard $k-\epsilon$ Model.....	25
3.6.2.3. Standard $k-\omega$ Model.....	26
3.6.2.4. $k-\omega$ SST Model	26
3.6.2.5. Realizable $k-\epsilon$ Model.....	27
3.6.2.6. Spalart-Allmaras Model	28
3.6.2.7. Near-wall Modeling.....	29
4. Steady-State NNS Characteristics	30
4.1. Thermal-hydraulic Behavior	30

4.2. Safety Margins.....	34
5. Accident Analyses	35
5.1. Loss of Power Accident	36
5.1.1. PSS.....	36
5.1.2. SSS.....	40
5.2. Loss of Heat Sink Accident	44
5.3. Reactivity Insertion Accidents	49
5.4. Loss of Flow Accidents	54
5.4.1. Seizure of One Pump.....	54
5.4.2. Loss of Two Pumps.....	59
5.5. Loss of Coolant Accidents.....	64
5.5.1. The 0.1 m break	64
5.5.2. The 0.2 m break	68
6. Flow Behavior Assessments.....	73
6.1. Inlet Region Behavior & CFD Modeling.....	73
6.2. Active Height Behavior & CFD Modeling.....	76
6.3. Outlet Region Behavior.....	79
7. Conclusions	81
8. Recommendations for Future Works	82
References	83
Appendix A. Pump Characteristics	88
Appendix B. Behavior of NNS for Accident Scenarios with SSS Applied.....	92
B.1. Loss of Heat Sink Accident with SSS.....	92
B.2. Reactivity Insertion Accident with SSS.....	96
B.3. Loss of Flow Accidents with SSS.....	100
B.3.1. Seizure of One Pump.....	100
B.3.2. Loss of Two Pumps.....	104
Appendix C. Mass Flow Rate in the Hot Channel for the Accidents	108
Appendix D. Power Evolution for the Accidents	110

List of Tables

Table 1. Nominal values for various thermal-hydraulic parameters in the NNS.	2
Table 2. Relevant geometrical constraints for the curved fuel channels in the NNS core.	3
Table 3. Hydraulic diameters for relevant portions of the primary system.	5
Table 4. Considered trips to the reactor protection system.	13
Table 5. The transient evolution of reactivity inserted into the core by the PSS.	13
Table 6. The transient evolution of the reactivity inserted into the core by the SSS.	14
Table 7. The values used for the standard $k-\epsilon$ model in this work.	25
Table 8. The values used for the standard $k-\omega$ model in this work.	26
Table 9. The values used for the $k-\omega$ SST model constants in this work.	27
Table 10. The values used for the Spalart-Allmaras model constants in this work.	28
Table 11. An overview of the hottest temperature values according to both steady-state models.	31
Table 12. An overview of the computed pressure-drop values (ΔP) across the core according to both steady-state models.	32
Table 13. A summary of the safety margins according to both steady-state models in comparison to NBSR safety margins with both HEU- and LEU-fueled NBSR cores. These are all at the hot channels (denoted in Table 11). Z_{hot} is the axial location relative to the center of the fueled zone in the core (negative being below the centerline, and positive being above the centerline).	34
Table 14. An overview of the NNS results for the system model and the core model at various cycle states.	35
Table 15. A companion to Table 14 that shows the axial locations of the hot of the minimum safety margins. Note that the location is Z_{hot} , which is relative to the axial centerline of the fueled zone in the core (negative being below the centerline, and positive above the centerline). All locations are in cm.	35
Table 16. A summary of the minimum ONBR, OFIR, and CHF throughout the loss of power accident.	36
Table 17. A summary of the minimum safety margins throughout the loss of heat sink accident. The minimum margins are all found in the hot channel at the axial location Z_{hot}	45
Table 18. A summary of the minimum safety margins throughout the reactivity insertion accident. The minimum margins are all found in the hot channel at the axial location Z_{hot}	50
Table 19. A summary of the minimum safety margins throughout a seizure of one pump LOFA. The minimum margins are all found in the hot channel at the axial location Z_{hot}	55
Table 20. A summary of the minimum safety margins throughout a loss of two pumps LOFA. The minimum margins are all found in the hot channel at the axial location Z_{hot}	60
Table 21. Pump curve segments for homologous curves (Adapted from [1]).	88
Table 22. Rated values for the NNS pumps.	91

List of Figures

Figure 1. An overview of the NNS geometry.	1
Figure 2. The NNS core (a) exploded view and (b) top-view with different channel types denoted with their respective lines.	2
Figure 3. A diagram of the primary system in the NNS.	4
Figure 4. Relative power distributions from the neutronics model. “FP” is the fuel plate number, “S” is the stripe number with stripes 1-3 going from bottom-to-top, and “Z” is the axial location in cm from the center.	6
Figure 5. The evolution of the power shape of any given stripe in any given FP in the NNS throughout the full cycle length of 40 days. The tick marks on the x-axis are left for convenience (to scale it to any desired power range).....	7
Figure 6. The NNS lumped-core nodalization in the system model.	9
Figure 7. The nodalization adopted in the NNS core model.....	10
Figure 8. A Nukiyama-style boiling curve with added labels relevant to this work.....	17
Figure 9. An illustration of the Ledinegg instability with relevant labels shown.....	18
Figure 10. A section view of the NNS highlighting distinct design features and identified regions of interest for CFD work.	23
Figure 11. Axial temperature distributions in the hot channel according to both the system model and the subchannel model (at startup). Note that axial centerline is at $Z = 0$ cm. The hot channel in the system model was channel 63 in row B. The hot channel in the core model was channel 2 in row A.	30
Figure 12. Axial pressure distributions in any channel in the core according to both the system model (dotted lines) and the subchannel model (dashed lines). Note that axial centerline is at $Z = 0$ cm.	32
Figure 13. The mass flow rate distribution across the core according to the system model (red triangles) and the core model (black circles). Note that the error bars are scaled by a factor of 4×10^5 kg/s to improve graphical visibility.....	33
Figure 14. The temporal evolution of temperatures throughout a loss of power transient with the PSS applied.	37
Figure 15. The temporal evolution of mCHFR throughout a loss of power transient with the PSS applied.	38
Figure 16. The temporal evolution of mOFIR throughout a loss of power transient with the PSS applied.	39
Figure 17. The temporal evolution of mONBR throughout a loss of power transient with the PSS applied.	40
Figure 18. The temporal evolution of temperatures throughout a loss of power transient with the SSS applied.	41
Figure 19. The temporal evolution of mCHFR throughout a loss of power transient with the SSS applied.	42
Figure 20. The temporal evolution of mOFIR throughout a loss of power transient with the SSS applied.	43
Figure 21. The temporal evolution of mONBR throughout a loss of power transient with the SSS applied.	44
Figure 22. The temporal evolution of temperatures throughout a loss of heat sink transient with the PSS applied.	46
Figure 23. The temporal evolution of mCHFR throughout a loss of heat sink transient with the PSS applied.	47
Figure 24. The temporal evolution of mOFIR throughout a loss of heat sink transient with the PSS applied.	48

Figure 25. The temporal evolution of mONBR throughout a loss of heat sink transient with the PSS applied.	49
Figure 26. The temporal evolution of temperatures throughout a reactivity insertion transient with the PSS applied.	51
Figure 27. The temporal evolution of mCHFR throughout a reactivity insertion transient with the PSS getting used.	52
Figure 28. The temporal evolution of mOFIR throughout a reactivity insertion transient with the PSS applied.	53
Figure 29. The temporal evolution of mONBR throughout a reactivity insertion transient with the PSS applied.	54
Figure 30. The temporal evolution of temperatures throughout a seizure of one pump LOFA transient with the PSS applied.	56
Figure 31. The temporal evolution of mCHFR throughout a seizure of one pump LOFA transient with the PSS applied.	57
Figure 32. The temporal evolution of mOFIR throughout a seizure of one pump LOFA transient with the PSS applied.	58
Figure 33. The temporal evolution of mONBR throughout a seizure of one pump LOFA transient with the PSS applied.	59
Figure 34. The temporal evolution of temperatures throughout a loss of two pumps LOFA transient with the PSS applied.	61
Figure 35. The temporal evolution of mCHFR throughout a loss of two pumps LOFA transient with the PSS applied.	62
Figure 36. The temporal evolution of mOFIR throughout a loss of two pumps LOFA transient with the PSS applied.	63
Figure 37. The temporal evolution of mONBR throughout a loss of two pumps LOFA transient with the PSS getting used.	64
Figure 38. The temporal evolution of temperatures throughout a LOCA transient (0.1 m break) with the PSS applied. Note that usage of SSS instead of the PSS yields near identical results (no notable variations).	65
Figure 39. The temporal evolution of mCHFR and mass flow rate throughout a LOCA transient (0.1 m break) with the PSS applied. Note that usage of SSS instead of PSS yields near identical results (no notable variations).	66
Figure 40. The temporal evolution of mOFIR and mass flow rate throughout a LOCA transient (0.1 m break) with the SSS applied. Note that usage of SSS instead of PSS yields near identical results, except the Costa correlation predicts a higher mOFIR peak at 350 s (mOFIR _{SSS} ~40; mOFIR _{PSS} ~150).	67
Figure 41. The temporal evolution of mONBR and mass flow rate throughout a LOCA transient (0.1 m break) with the SSS applied. Note that the usage of PSS instead of SSS yields a higher mONBR peak in the coast-down period (mONBR _{SSS} ~21; mOFIR _{PSS} ~25).	68
Figure 42. The temporal evolution of temperatures throughout a LOCA transient with the PSS applied.	69
Figure 43. The temporal evolution of mCHFR and mass flow rate throughout a LOCA transient (0.2 m break) with the PSS applied.	70
Figure 44. The temporal evolution of mOFIR and mass flow rate throughout a LOCA transient (0.2 m break) with the PSS applied.	71
Figure 45. The temporal evolution of mONBR and mass flow rate throughout a LOCA transient (0.2 m break) with the PSS applied.	72
Figure 46. The streamwise and spanwise velocity profiles at the inlet according to the preliminary CFD assessments.	74

Figure 47. Graphical deviation matrices between different RANS models for predictions in streamwise velocity (left) and spanwise velocity (right). Here, deviation is the standard deviation between any two profiles divided by their average.75

Figure 48. The (a) 2D mesh and (b) 3D mesh implemented for the single-channel validation studies.77

Figure 49. A summary of the validations from the findings of the single-channel study. Note the adoption of $Y^* = Y_{distance\ from\ wall} / Width\ of\ channel / 2$ to maintain consistency with the Ha et al. [52] presentation of results.78

Figure 50. An illustration of the predicted flow patterns that could be encountered at the outlet of the NNS.79

Figure 51. NNP Pumps Homologous Curves for Pump Head.....89

Figure 52. NNP Pumps Homologous Curves for Pump Torque.....90

Figure 53. The temporal evolution of temperatures throughout a loss of heat sink transient with the SSS applied.92

Figure 54. The temporal evolution of mCHFR throughout a loss of heat sink transient with the SSS applied.93

Figure 55. The temporal evolution of mOFIR throughout a loss of heat sink transient with the SSS applied.94

Figure 56. The temporal evolution of mONBR throughout a loss of heat sink transient with the SSS applied.95

Figure 57. The temporal evolution of temperatures throughout a reactivity insertion transient with the SSS applied.96

Figure 58. The temporal evolution of mCHFR throughout a reactivity insertion transient with the SSS applied.97

Figure 59. The temporal evolution of mOFIR throughout a reactivity insertion transient with the SSS applied.98

Figure 60. The temporal evolution of mONBR throughout a reactivity insertion transient with the SSS applied.99

Figure 61. The temporal evolution of temperatures throughout a seizure of one pump LOFA transient with the SSS applied.100

Figure 62. The temporal evolution of mCHFR throughout a seizure of one pump LOFA transient with the SSS applied.101

Figure 63. The temporal evolution of mOFIR throughout a seizure of one pump LOFA transient with the SSS applied.102

Figure 64. The temporal evolution of mONBR throughout a seizure of one pump LOFA transient with the SSS applied.103

Figure 65. The temporal evolution of temperatures throughout a loss of two pumps LOFA transient with the SSS applied.104

Figure 66. The temporal evolution of mCHFR throughout a loss of two pumps LOFA transient with the SSS applied.105

Figure 67. The temporal evolution of mOFIR throughout a loss of two pumps LOFA transient with the SSS applied.106

Figure 68. The temporal evolution of mONBR throughout a loss of two pumps LOFA transient with the SSS applied.107

Figure 69. The mass flow rate evolution in each of the analyzed accidents with PSS applied. 108

Figure 70. The mass flow rate evolution in each of the analyzed accidents with SSS applied. 109

Figure 71. The reactor power evolution in each of the analyzed accidents with PSS applied. .110

Figure 72. The reactor power evolution in each of the analyzed accidents with SSS applied. .111

Preface

The new reactor design for the NNS is actively being updated, and the current iteration is not meant to be the finalized form of the design. The finalized design may be significantly different than the current iteration. The authors acknowledge the team of individuals working on the design, which includes current members from the NCNR, contributors outside the NCNR, and past contributors: their names are listed below in alphabetical order.

Current NCNR Members

Mohammed G. Abdoelatef, Osman Ş. Çelikten, Jeremy C. Cook, David J. Diamond, Noura R. Elsalamouny, Peter M. Gehring, Anil Gurgen, John M. Jurns, Hubert E. King, Charles F. Majkrzak, Dan A. Neumann, Thomas H. Newton, Dağistan Şahin, Joy S. Shen, Abdullah G. Weiss

External Contributors

Argonne National Laboratory, Nuclear Science and Engineering Division

Milan Dragas, Mitchell T. Farmer, Thad A. Heltemes, Zhiee J. Ooi, Basar Ozar, Jordi Roglans-Ribas, John G. Stevens, John A. Stillman, Erik H. Wilson, Dhongik S. Yoon, Zhaopeng Zhong

Brookhaven National Laboratory, Nuclear Science and Technology Department

Lap-Yan Cheng, Arantxa Cuadra, Peter Kohut, Cihang Lu, Athi Varuttamaseni

National Nuclear Security Administration

Natraj Iyer, Kyle Sallee

Lithuanian Energy Institute

Mantas Povilaitis

Shimon Peres Negev Nuclear Research Center

Idan R. Baroukh, Eliezer Nahmani, Yaniv Shaposhnik

NIST, Engineering Laboratory, Structures Group

DongHun Yeo

Past NCNR Contributors

Danyal J. Turkoglu (*currently affiliated with USNC-Tech*)

Robert E. Williams

Zeyun Wu (*currently affiliated with Virginia Commonwealth University*)

Interns

Duncan Beauch, Evan Bures, Amir Dajani, Julia Jiang, Patrick Park, Eric Swanson, Iman Syed, Breken Wallar

1. Introduction

The NNS is a nuclear reactor planned to eventually replace the NBSR as a US-based source primarily for out-of-core neutron scattering and irradiation research. The current preconceptual design for the NNS is a compact 20 MW reactor core composed of nine fuel assemblies surrounded by a heavy water reflector tank housing two cold neutron sources. The reactor core geometry is shown in Figure 1 and Figure 2, where emphasis is shown on the coolant paths. The coolant flow paths through the core become clear when looking at a top view of the core as shown in Figure 2(b), where each row in the core contains three fuel assemblies (FAs) with 21 fuel plates (FPs) yielding 64 coolant channels in total throughout the row. Each channel conforms to one of the four types listed below, where the channel gap and length are the main differences between each of the channel types.

- FP-Chimney (marked in **dotted orange**) is the channel formed by the right-most FP's surface in the row and the chimney wall.
- FP-FP (marked in **solid blue**) is the channel formed by two adjacent FPs in the same FA.
- FA-FA (marked in **dash-dotted red**) is the channel formed by two adjacent FPs from different FAs on the same row in the core.
- Chimney-FP (marked in **dashed yellow**) is the channel formed between the chimney wall and the left-most FP's surface in the row.

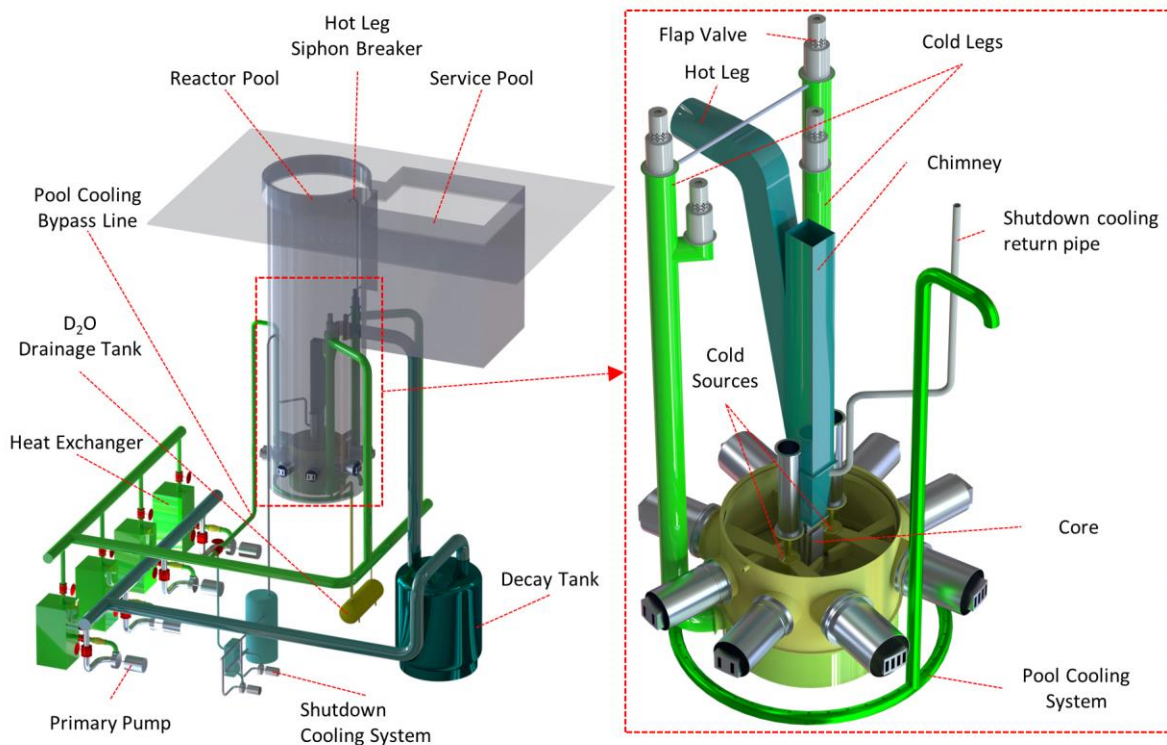


Figure 1. An overview of the NNS geometry.

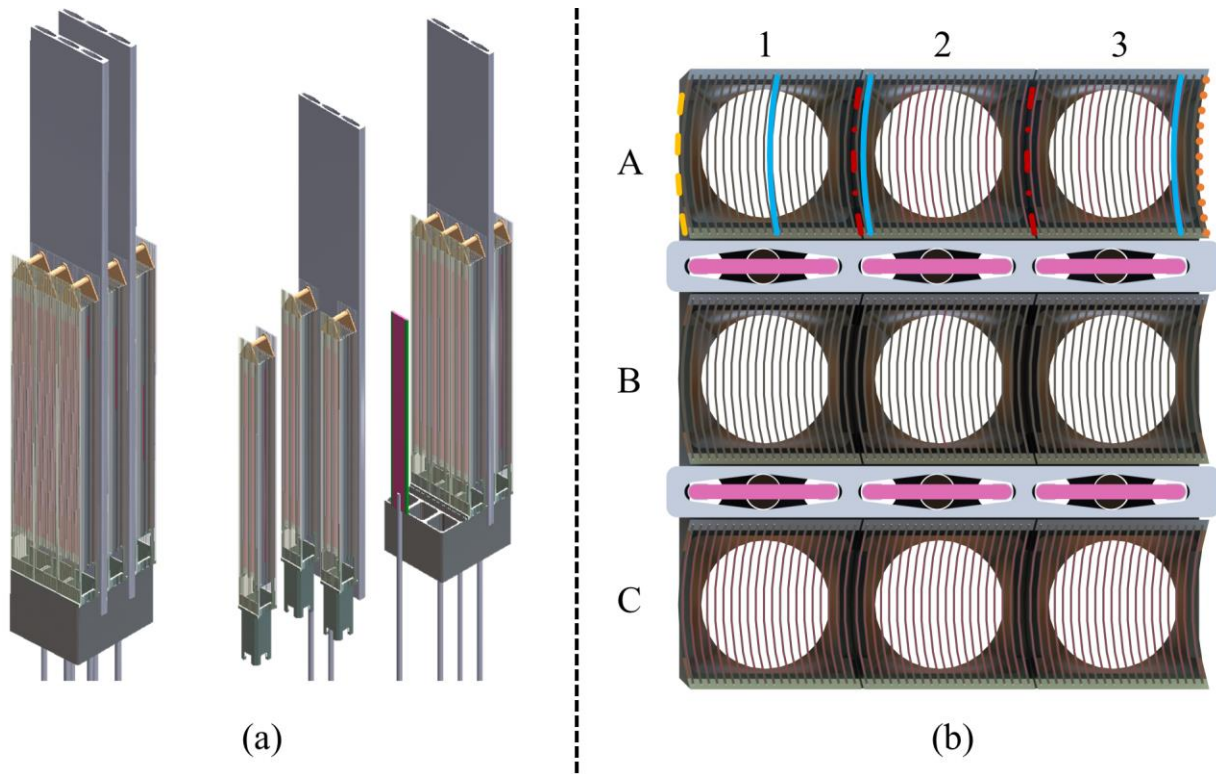


Figure 2. The NNS core (a) exploded view and (b) top-view with different channel types denoted with their respective lines.

This work provides an understanding of the NNS’s thermal-hydraulics safety in steady-state and transient conditions using a variety of thermal-hydraulics models. Steady-state assessments are conducted using results from system code models of the NNS. System code models are developed using the TRAC/RELAP Advanced Computational Engine (TRACE) code [1]. Transient analyses are conducted using the TRACE models of the NNS, which involve understanding the behavior of the core in various postulated accident scenarios. Detailed assessments of the flow behavior are discussed using results from CFD models of various portions of the NNS core. The results and discussions provided in this document serve as a holistic and detailed assessment of the preconceptual design’s thermal and hydraulic adequacy, and they provide recommendations for future works in pursuit of a safer and more efficient design. For the reader’s convenience, a list of nominal parameters for the reactor (as relevant to this work) are in Table 1.

Table 1. Nominal values for various thermal-hydraulic parameters in the NNS.

Nominal Parameter	Core Power (MW)	Temperature (K)		Flow Rate (kg/s)		Pressure Drop (bar)	Pool Level (m)
		Inlet	Outlet	System	Core Inlet		
Value	20	316.5	331	600	540	0.44 ^a	15 ^b

^a This is the pressure drop from the inlet plenum to the outlet plenum (entrance to chimney).

^b The top of the pool is at 15.33 m.

1.1. Overview of the NNS Primary System and Relevant Geometric Details

All relevant geometric constraints for each of the channel types from Figure 2(b) can be found in Table 2, where the reader should note that the FPs are 780 mm long, 75 mm wide, and 1.13 mm thick. Note that the side FPs are 20 mm longer than the rest (bringing their length to 800 mm), where the fuel core in all the plates is identical and occupies a volume of 700 mm in length, 65 mm in width, and 0.25 mm in thickness. Note that the channel widths and inner chord lengths are identical for all the channels in Figure 2(b). Relevant to the discussions herein is the notation used to describe different components in the core. Considering how each FA contains 21 plates, the 1st plate is the left-most plate and the 21st plate is the right-most plate, respectively to Figure 2(b). As such, the left-most channel is the Chimney-FP channel in the 1st column of the core; and the right-most channel is the Chimney-FP channel in the 3rd column of the core.

Table 2. Relevant geometrical constraints for the curved fuel channels in the NNS core.

Constraint (mm)	Channel Type				Curved Channels Guidance Graphic
	FP-FP	FA-FA	Chimney-FP	FP-Chimney	
Inner chord length	69.757				
R1	141.13	141.13	140	141.13	
R2	140	140	140	141.13	
Arcs centers distance ‘c’	3.874	5.39	4.024	4.024	
Channel width	69.757				
Flow area (A_{flow}, mm²)	190.581	297.824	201.043	201.043	
Wetted perimeter (P_{wet})	146.402	140.998	140.984	140.984	
Hydraulic diameter (D_h)	5.207	8.449	5.704	5.704	
Minimal gap	2.707	4.223	2.882	2.882	
Maximal gap	2.744	4.260	2.882	2.882	
Height	780	800	800	800	

Figure 3 illustrates the NNS’s primary system loop. Four primary pumps (PP1-PP4) are included in the system; but only three are needed for operation; the fourth is left on stand-by for redundancy. Each pump is connected to a separate plate-type heat exchanger (HX1-HX4). For simplicity, we assume the primary pumps and heat exchangers used for our analyses are the exact same as the NBSR pumps and heat exchangers [2]. Each of the primary pumps is equipped with a flywheel to help in the coast down of the pump during a loss of power transient. This is a design feature that is common with other pool-type high performance research reactors [3]. All pumps in the primary loop are equipped with check-valves at their discharge lines to prevent backflow.

Note the presence of two cold legs with a pipe connecting them (visible on Figure 1). This connector pipe equalizes the pressure in both cold legs, ensuring the operation of the flap valves (when needed) at the same time in case one of the flap valves fails. Similar to the NBSR [2], the NNS has two centrifugal pumps that provide forced convection cooling to the reactor during shutdown periods (SDP1-SDP2), where only one of the two pumps would be necessary to remove decay heat from the core. The shutdown pumps feed into a shutdown system heat exchanger (SDHX), which send the flow to the pool-cooling bypass line, maintaining cooling in the pool during shutdown periods.

Table 3. Hydraulic diameters for relevant portions of the primary system.

Pipe	Hydraulic Diameter (m)
Pump Discharge Line	0.48
Cold Leg	0.38
Hot Leg	0.59
Chimney	0.46
Cold Leg Connector	0.06
Hot Leg Siphon Breaker	0.06
Pool Cooling Bypass Line	0.20
Pool Cooling System (41 openings over 330° circumference)	0.04 (For each opening)
	4.5 (total)
Pool (15.33 m deep, filled to 15 m)	1.61 (with reflector tank)

2. Power Profiles

This work is part of a series of NIST technical notes describing preconceptual design activities for the NNS. It borrows data from analyses conducted in the preliminary neutronics assessments report [4]. Power profiles are imported directly from the neutronics models described in that report, and they are vital to setting up our analyses and models. In the neutronics analyses, different cycle states were considered from startup to end-of-cycle. Figure 4 shows an assessment of the relative powers' maxima and minima, their locations, and that the 1st and 21st FPs are always the hottest plates in any given FA.

Note the usage of dimensionless relative powers in our analyses, which are relative to average power of a given stripe. The relative power at any location n ($Q_{*,n}$) is presented in Eq. (1), where Q_n is the actual power at that location and N is the total number of locations within the set that n lies such that $\{n \in \mathbb{N} \mid 1 \leq n \leq N\}$. That is, Eq. (1) can be applied to any set of locations that share the same characteristics such as volume. The only relevant characteristic set is that of a set of finite volumes making up the entirety of an FP or a channel. Note, the denominator in Eq. (1) is not the same as the average presented in Figure 4, where that average corresponds to the relative powers average (summing across $Q_{*,n}$) and not necessarily the average of the actual powers (summing across Q_n). It is important to understand how the relative powers are computed because the power results in our analyses will be presented in this dimensionless format to ensure a convenient comparison.

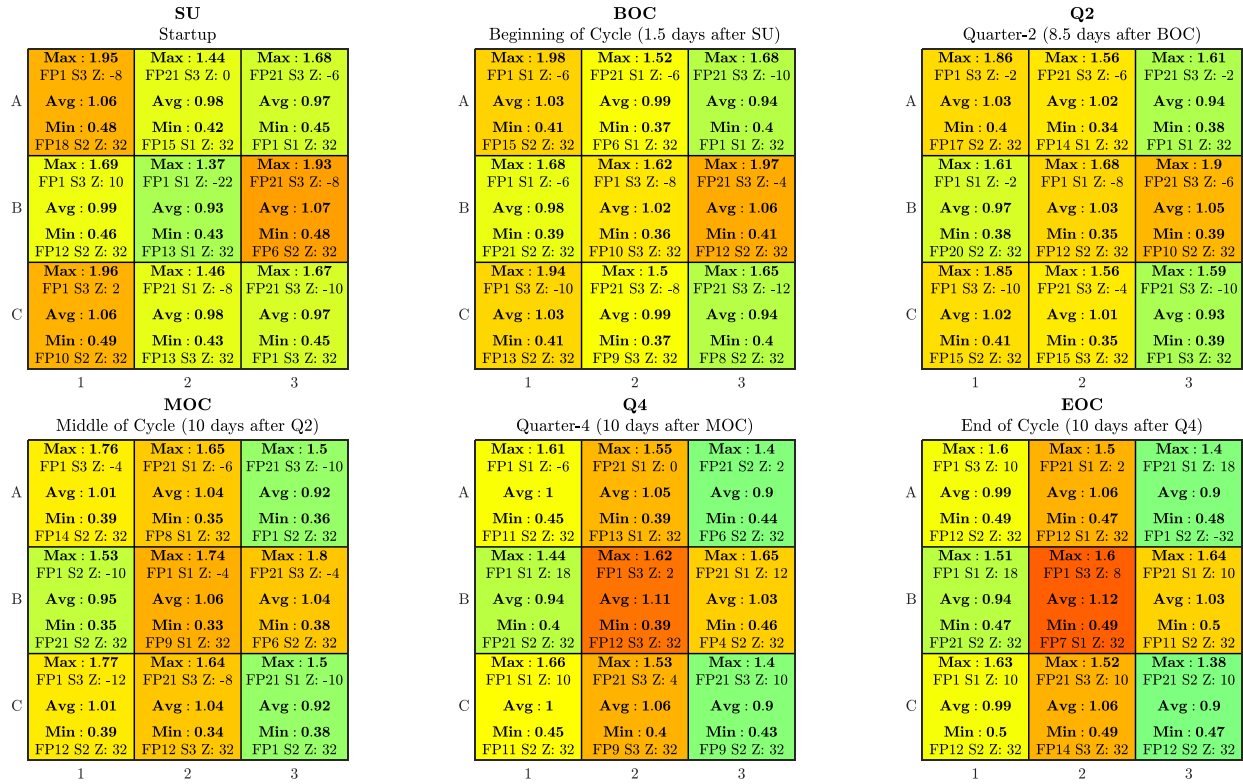


Figure 4. Relative power distributions from the neutronics model. “FP” is the fuel plate number, “S” is the stripe number with stripes 1-3 going from bottom-to-top, and “Z” is the axial location in cm from the center.

$$Q_{*,n} = \frac{Q_n}{\sum_{n=1}^N \left(\frac{Q_n}{N}\right)} \quad (1)$$

Figure 5 shows that the power shape throughout the cycle does not change. Further, Figure 5 shows the NNS starts with a flattened power shape within the center 40 cm of the FPs; then progresses to a chopped cosine biased towards the bottom half of the FPs throughout the first half of the cycle; then becomes more biased towards the top of the FPs. The change in the chopped cosine bias from bottom to top can be correlated to the movement of the shim blades in the core as they are removed slowly from the core. The flat and suppressed power shape at startup (relative to the other cycle states) can be attributed to the cadmium burnable poison wires in the fresh FAs suppressing the power early in the cycle. Cadmium gets burned up as the cycle continues, enabling the observed increase in the power as the cycle progresses. This power shape variation is relevant when considering a certain accident scenario taking place. In most accident scenarios considered, startup is the power shape of interest.

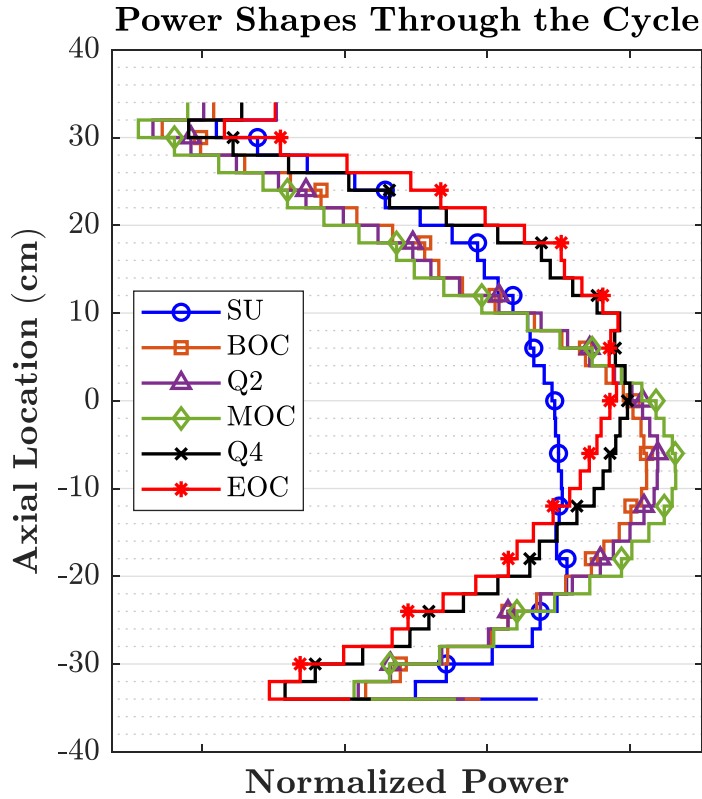


Figure 5. The evolution of the power shape of any given stripe in any given FP in the NNS throughout the full cycle length of 40 days. The tick marks on the x-axis are left for convenience (to scale it to any desired power range).

3. Methodology

3.1. Overview of TRACE

The thermal hydraulics behavior of the core is assessed using the TRACE V5.0 Patch 5 code [1]. The NRC developed the TRACE software tool to provide comprehensive simulation capabilities for analyzing thermal-hydraulic conditions within nuclear reactor systems. TRACE is engineered to model thermal and hydraulics phenomena within nuclear reactors under both normal operational conditions and hypothetical accident scenarios. It incorporates models for reactor core kinetics, decay heat, heat transfer, fluid flow, phase-change phenomena, control logic, and component interactions in both single-phase and two-phase flow dynamics; therefore it offers a robust platform for the safety analysis of water-type reactors. TRACE is utilized for regulatory reviews and safety assessments, and it plays a pivotal role in ensuring nuclear reactors operate within safety limits.

3.2. NNS TRACE Model

We use TRACE for our thermal-hydraulics analysis of the NNS because the code has robust modeling capabilities and a proven track record in nuclear safety analysis. Using TRACE for the thermal-hydraulics analysis of the NNS, we aim to achieve an accurate prediction of the reactor's response to various operational states and accident scenarios. This predictive capability is crucial for ensuring the NNS design meets the necessary safety margins and complies with regulatory standards.

The NNS TRACE model contains the reactor core, primary cooling loops, reactor coolant pumps, heat exchangers, decay tank, and the reactor pool, as shown in Figure 1. This model serves as the foundation for both steady-state and transient analyses and provides insights into potential areas for further optimization.

The physical components of the NNS are modeled in the TRACE model with actual physical dimensions and connections. The only exception to this approach is the NNS's reactor core. The reactor core has a simplified model because it would be too computationally expensive to model every coolant channel. The following sections detail the modeling approach for reactor geometry and components.

3.2.1. Core Nodalization

The NNS's reactor core contains nine fuel assemblies, arranged in three rows and three columns. The fuel assemblies at each row share a coolant channel with the adjacent fuel assembly, and the rows are isolated from the other rows by control blade housings. This arrangement allows the treatment of each row as a grouped fuel assembly. For each row, the FPs near the reflector tank have the highest power peaking factors; therefore these plates are modeled as single FPs. For each row, three FPs at each side are modeled as a single FP, and the remaining 57 inner FPs are lumped into one FP by conserving the total power generation of FPs and total heated area. The coolant channels are also modeled by following the FP pattern. The lumped FP is in a lumped coolant channel with the total flow area conserved. The single FPs are connected to the neighboring coolant channels with the dimensions given in Table 2. The openings of the control blade housing are lumped into a single flow channel, and this single channel models the core bypass flow. The layout of the NNS core model is shown in Figure 3.

For each fuel assembly, the end plates are 80 cm long and the inner plates are 78 cm long. But the fuel core is 70 cm long at each FP. Neutronics analysis of the NNS provides the power profile for each FP separately with 2 cm intervals. To reduce the computational cost of the transient analysis, the fuel core in each FP is divided into seven nodes with 10 cm length each. To represent the accurate power profiles of FPs, each FP's power generation is lumped together with the consideration that the total power generation by each FP is the same as the value calculated by the neutronics analysis. The nodalization of the coolant channels follows the nodalization of FPs, so each node in the FPs is connected to a single node in the coolant channels.

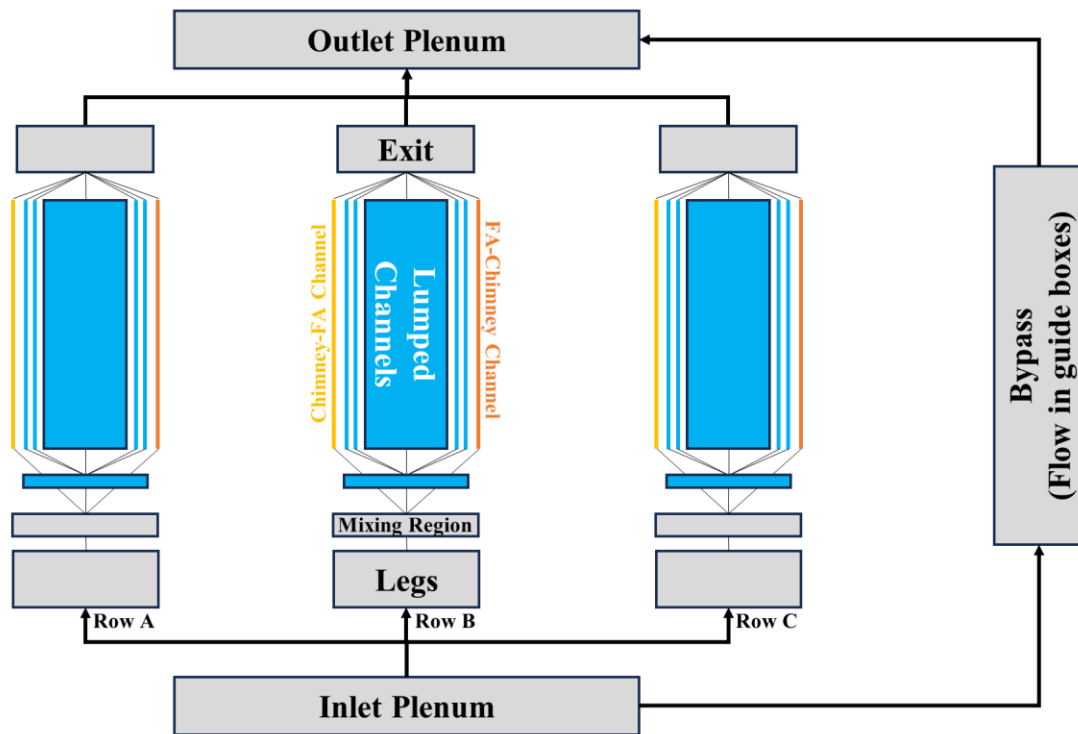


Figure 6. The NNS lumped-core nodalization in the system model.

The simplification of fuel elements into lumped groups reduces the computational cost of transient simulations. However, this approach compromises the precision of core calculations and introduces additional uncertainty to the thermal-hydraulic analysis of the core. To evaluate the impact of this simplification on accuracy, a separate core model of the NNS was constructed using TRACE V5.0 Patch 5. The separate core model eliminated the concerns related to solution approaches to conservation equations and closure relations. This dedicated model provides a better understanding of how lumping thermal and hydraulic components affects the overall core behavior predictions. The core model contains the whole 189 FPs and 192 coolant channels. Neutronics analysis of the NNS provides the power profile for each FP separately with 2 cm intervals; therefore each FP has 35 axial nodes with different power generations. The core model provides detailed velocity, temperature, and pressure profiles of the NNS core to compare with the NNS system model.

The core model focuses on the core components, such as fuel elements and inlet/outlet plenum. To integrate with the NNS system, the core model requires boundary conditions. For coherence, the core inlet mass flow rate and core outlet pressure from the comprehensive system model are replicated in the core model. To ensure uniformity and accuracy across analyses, identical modeling techniques and parameters are used for both the system and core models. This approach guarantees a reliable comparison and uncertainty related to the lumping of core components in the system model. The nodalization adopted in the core model is shown in Figure 7.

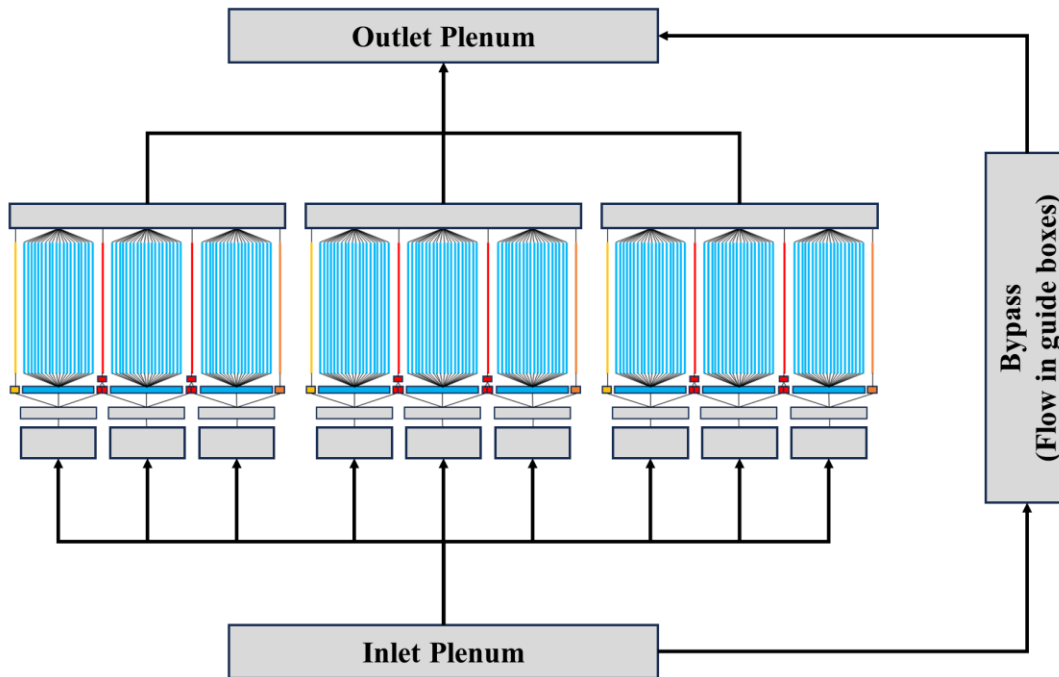


Figure 7. The nodalization adopted in the NNS core model.

3.2.2. Reactor Coolant Pumps

Reactor coolant pumps circulate the coolant water through the system to remove the heat from FPs. Modeling the reactor coolant pumps is important to predict the behavior of the pump and coolant flow during the transients. Since the pump characteristics of the NNS are not determined, existing pump characteristics of the NBSR are used to model the NNS reactor coolant pumps. TRACE models the pump head and torque using homologous curves, which represent the performance of the pump in a normalized format. The parameters of the homologous curves and the rated values for the NNS pumps are given in Appendix A.

Although the pumps used in the NNS are identical to those in the NBSR, the effective moment of inertia of the pumps are distinct. The NNS reactor coolant pumps are equipped with hypothetical inertia flywheels designed to maintain coolant flow to the core after reactor coolant pumps are shut down. The total moment of inertia of reactor coolant pumps, including flywheels, is chosen to be 75 kg/m^2 , which is compatible with the OPAL design [5]. In the TRACE model, three of the four reactor pumps are modeled individually, reflecting operational strategy; wherein the fourth pump is designated as standby, ready to activate as necessary or be offline for maintenance.

In the NNS design, the pump discharge line has an interconnection with the reactor pool that diverts 10% of the total system coolant mass flow to the reactor pool. This flow creates a downward flow in the upper section of the chimney, preventing activated isotopes from reaching the top of the reactor pool. To achieve the 10% flow diversion, a valve is added to the TRACE model and the flow area of the valve is iteratively calibrated to provide the desired 10% flow diversion.

During normal operation, the coolant flow through the reactor coolant pumps is bidirectional. During transient conditions, if one or two pumps are tripped, forced flow from the remaining

energized pumps can create a backflow on tripped pumps that may lead to reverse rotation of the impellers and result in damage to the pumps. To prevent backflow, NNS pumps are equipped with check valves at the location of pump exits. In the TRACE model, the functionality of these check valves is represented by connecting valve components to the corresponding pipe components. The model is designed to reduce the flow area of the valve to zero whenever the liquid water velocity falls below 0.5 m/s at the interface between the valve and pump components. The control logic for the check valves is simulated using TRACE's control systems feature. When activated, this logic reduces the flow area of the valve and isolates the pump from the coolant flow path. The closure time of the check valves is chosen to be 1 second to be compatible with the NBSR nozzle check valves, which are reported to be ~0.7 seconds.

3.2.3. Heat Exchangers

The NNS TRACE model incorporates heat exchangers that reflect the specifications of the NBSR heat exchangers. These modeled heat exchangers feature plates that extend to 1.83 meters in length and collectively offer a total heat transfer area of 422 m² across the primary and secondary loops. Since the specifications of the NNS heat exchangers are not finalized, this gives flexibility to adjust both the heat exchangers and the parameters of the secondary cooling loop. Such adjustment ensures that the model meets the specific inlet temperature of the NNS core.

In a simplification within the NNS TRACE model, the entire secondary cooling loop is represented by a single mass flow rate source and pipes rather than a detailed loop. Through iterations, the secondary coolant mass flow rate has been determined to be 900 kg/s, entering the heat exchangers at a temperature of 302 K. To ensure the system's operational parameters align with the desired reactor core inlet temperature, TRACE employs a steady-state controller. This controller adjusts the total heat transfer area of the heat exchanger, thus enabling the NNS TRACE model to define and maintain steady-state conditions. The NNS TRACE model utilizes this controller to define steady-state parameters.

3.2.4. Flap Valves

A key feature of the NNS is its classification as a pool-type reactor. This design ensures a substantial volume of coolant, which can function as a heat sink during certain abnormal conditions, and the NNS core can be cooled with natural circulation to remove the decay heat. To establish a natural circulation path, the cold legs are equipped with two flap valves that connect the cold leg lines to the reactor pool. Both flap valves are above the upper edge of the chimney: the upper flap valve is located 195 cm above and the lower flap valve is located 65 cm above. In the event of a loss of coolant where the water level of the reactor pool drops, the upper flap valves serve as siphon breakers and prevent the water level from dropping further below the upper flap valve. The lower flap valves will open, thus creating the natural circulation path. If primary cooling pumps are stopped, both flap valves open due to pressure loss of the system and establish the natural circulation path. Both cold legs have separate sets of flap valves. The upper flap valves are connected to each other with a pipe to allow siphon breaking on both cold leg lines if one of the flap valves fails to open.

The flap valves are modeled in the TRACE model using built-in valve components with an actuation trip. The actuation trip is generated based on arithmetic computing blocks that calculate

the hydrostatic and gravitational forces that act on the valve disc. In normal operation, the hydrostatic force is greater than the gravitational force because of the forced flow produced by the reactor cooling pumps. The flap valves are fully closed in this scenario. If the reactor cooling pumps are stopped, the gravitational force becomes greater than the hydrostatic force and the flap valves open in one second. The actuation trip is single-sided, meaning the flap valves are locked once they are open and they cannot be closed even if the hydrostatic force overcomes the gravitational force.

3.2.5. Reactor Power

The reactor power component of the TRACE model is responsible for modeling the heat produced by nuclear fission within the nuclear fuel elements and decay heat. It considers the distribution of power density across the core, which is influenced by factors such as fuel type, geometry, and the arrangements of the fuel elements. The power density distribution of the NNS is calculated in neutronics analysis [4] and the TRACE model uses the calculated power profiles of each FP. The NNS TRACE model has a lumped core, and the power profiles of the FPs are modified to reflect the lumping strategy.

TRACE uses point kinetics equations to calculate the dynamic response of the reactor power to control actions and feedback mechanisms. The reactivity feedback effects—from changes in temperature, coolant density, or other reactor parameters—are neglected and will be included in future design revisions. The point kinetics equation parameters are taken from the neutronics analysis of the NNS [4].

For the decay heat calculations, TRACE has multiple options. We have selected ANS-79 w/ Decay for U239/NP239 [6] to model the decay heat.

3.2.6. Reactor Protection System

The reactor protection system (RPS) is an instrumentation system that initiates actions to safely shutdown the reactor. RPS is modeled using the control logic blocks of the TRACE. The initiator of shutdown systems would be any one or more combinations of RPS trips considered in Table 4. The current design of the NNS has two shutdown systems: (1) the primary shutdown system (PSS) is the insertion of safety blades into the core; (2) the secondary shutdown system (SSS) is dumping the D₂O in the reflector tank. The shutdown systems provide unique transient reactivity feedbacks that depend on their temporal evolution, where the PSS would be able to insert negative reactivity quicker than the SSS because the safety blades can be inserted faster than draining the reflector tank to its halfway level.

Table 4. Considered trips to the reactor protection system.

Trip Name	Trip Value
Reactor Power	125% (25 MW)
Pool Level	1 m below the top of the pool
Reactor ($T_{\infty,out}$)	338 K
Primary Coolant Flow (\dot{m})	370 kg/s
Core Temperature Difference (ΔT_{∞})	13 K
Pressure Difference High (ΔP)	5 bar
Pressure Difference Low (ΔP)	4 bar

In accident conditions, if one or more combinations of RPS trips are generated, the RPS generates the scram signal. The first responder to the scram signal is the PSS and it starts inserting safety blades into the core to shut down the reactor. The safety blades are assumed to start moving after 0.5 seconds once the scram signal is generated, which is based conservatively on the maximum time it takes for the NBSR shim arms to fully insert [2]. In the current design of the NNS, it takes 0.9 seconds for the blades to be fully inserted into the core at a height of 70 cm. The worth of safety blades are calculated in the neutronics analysis [4]. Based on the presumed velocity and integral reactivity of the safety blades, the reactivity feedback inserted into the core by the PSS once the scram signal is generated is in Table 5. The reactivity in Table 5 is inserted into the POWER component of the TRACE model.

Table 5. The transient evolution of reactivity inserted into the core by the PSS.

Time (s)	PSS Reactivity ($\Delta\rho$)	Time (s)	PSS Reactivity ($\Delta\rho$)
0.0	0.0	1.0	-0.067711
0.5	0.0	1.1	-0.09030
0.6	-0.0072333	1.2	-0.11321
0.7	-0.017022	1.3	-0.13167
0.8	-0.030067	1.4	-0.1389
0.9	-0.046789		

The PSS is the first shutdown system that the NNS relies on, but it is not the only one. The SSS can be used to insert sufficient negative reactivity into the core to shut it down without any additional operator interference. The SSS dumps the D₂O from the reflector tank into a D₂O drainage tank. Reactivity as a function of the dump level is computed in the neutronics assessment [4]. However, details of such a shutdown system are not specified. So, we assume that the reflector tank drainage system is identical to that in OPAL. The safety analysis report of OPAL [3] assumes that when the SSS is triggered, approximately half the reflector tank is dumped and replaced with

He in ~10 seconds. The SSS actuates automatically only if the PSS fails (i.e., only if the safety blades are not inserted into the core). Hypothetically, it takes 1.4 seconds for safety blades to be fully inserted into the core. The SSS should detect if the control blades are not fully inserted and start opening the dump valves. We assume it takes one second for the SSS to detect safety blades are not inserted fully and open the dump valves. So, no reactivity insertion occurs prior to opening the valves at the 2.4 seconds mark, yielding the behavior shown in Table 6.

Table 6. The transient evolution of the reactivity inserted into the core by the SSS.

Time (s)	SSS Reactivity ($\Delta\rho$)	Time (s)	SSS Reactivity ($\Delta\rho$)
0.0	0.0	7.4	-0.01643
1.4	0.0	8.4	-0.03755
2.4	0.0	9.4	-0.05422
3.4	-0.00234	10.4	-0.07154
4.4	-0.00384	11.4	-0.09215
5.4	-0.00566	12.4	-0.12315
6.4	-0.00730		

3.3. Steady-State Analysis

The steady-state analysis in the TRACE model illustrates the baseline operational behavior of the NNS under normal operation. This analysis provides a foundational understanding of the reactor’s thermal-hydraulic performance, serving as a benchmark for evaluating deviations during transient scenarios.

The primary objective of the steady-state analysis is to simulate the NNS’s operation at its nominal power level, where all parameters are expected to be stable and within the design considerations. This analysis aims to confirm that the reactor maintains safe temperature profiles, adequate coolant flow rates, and proper pressure levels throughout the system under normal operating conditions. It also serves to validate the effectiveness of the NNS cooling systems in maintaining the core within safe operational limits.

To accurately represent the reactor’s steady-state operation, the TRACE model is configured with predefined operational parameters such as reactor power output, core coolant inlet temperature, and system mass flow rate to correspond to normal operating conditions. The reactor power of the NNS is 20 MW assuming that all the heat is generated in the FPs. The power generation of each FP node is calculated automatically by TRACE with the provided power profiles and the lumping strategy.

The nominal mass flow rate through the NNS core is determined to be ~540 kg/s. Ten percent of the total system coolant mass flow is diverted to the reactor pool, resulting in a total system coolant mass flow rate of 600 kg/s. Since three pumps are working in normal operation, each pump should deliver ~200 kg/s. To achieve the required mass flow rate, TRACE has an internal controller that

modifies the pump impeller velocity. This controller is used to ensure that each reactor cooling pump delivers 200 kg/s.

The TRACE internal controller is used to regulate the temperature of the reactor core inlet. The desired temperature of the reactor core inlet is approximately 316.5 K. The TRACE internal controller adjusts the heat exchanger's heat transfer area until the defined core inlet temperature is achieved. This process involves iterative calculations during which the secondary cooling system parameters are fixed, and the TRACE controller is used to match the reactor core inlet temperature of 316.5 K.

3.4. Transient Analysis

The transient analysis of the NNS is a comprehensive safety and performance evaluation of the reactor. The primary objective of the transient analysis is to assess the robustness and resilience of the NNS design under conditions that differ from the steady-state operation. These conditions are a set of pre-selected potential accident scenarios. The analysis aims to identify the reactor's behavior under such transient conditions, evaluating the effectiveness of its inherent safety features.

The selection of transients is based on a combination of regulatory requirements and engineering judgment. Each of the transient analyses includes two distinct cases. The initial case presumes an orderly shutdown via the PSS. The alternative scenario adopts a more conservative stance, hypothesizing a scenario where the safety blades fail to be inserted. Here, we assume the reactor shuts down via activation of the SSS. The analyzed transient scenarios include:

- **Loss of Power Accident (LOPA):** This scenario examines the implications of a complete electrical power outage at the facility, triggering an automatic reactor shutdown that is independent of the RPS. The de-energization of control rod electromagnets causes the safety blades to drop into the core, marking the onset of the event. Concurrently, the electrical power supply to both the primary cooling pumps and the secondary loop is severed. While the primary pumps decelerate, leveraging the inertia of the flywheels, the flow in the secondary loop ceases within a span of one second.
- **Loss of Heat Sink Accident (LOHSA):** This scenario examines the condition where the reactor faces a complete loss of cooling capability in the secondary loop, rendering the heat exchangers non-functional. The accident starts with the loss of secondary coolant flow within the first second. Following the initiation of the accident, the reactor stays at full power until the RPS is activated, triggering a reactor trip. Throughout this transient period, the primary cooling pumps operate at their maximum capacity to manage the reactor's thermal load.
- **Reactivity Insertion Accident (RIA):** This scenario examines the consequences of the insertion of reactivity into the reactor core. The considered accident for this report is the simultaneous and inadvertent withdrawal of control blades at their maximum feasible velocity of 3.5 mm/s. This rapid removal of the control blades introduces excessive reactivity into the core. Once the RPS trip points are reached, the reactor is tripped, and the withdrawal of the control blades are stopped. Throughout the accident, primary cooling pumps and the secondary cooling system continue to operate at their fullest capacity.

Loss of Flow Accident (LOFA): This scenario examines when one or more primary cooling pumps fail and lose their functionality. The first scenario, termed the pump shaft seizure accident, occurs when the shaft of one of the primary cooling pumps seizes unexpectedly, causing an immediate halt in coolant flow through that pump. Despite this abrupt failure, the remaining two primary pumps persist in operating at their maximum capacity. The reactor is tripped once the RPS trip points are reached and the reactor is shut down by the shutdown systems. The second scenario, termed the pump motor failure accident, occurs when two of the primary cooling pumps motors fail at the same time. This results in a gradual decrease in coolant flow as these pumps coast down, guided by the inertia of their flywheels. The third pump, unaffected by this issue, continues to operate at full capacity. Similar to the first scenario, the reactor is brought to a controlled shutdown upon reaching the RPS trip points. Throughout both types of LOFAs, we assume the secondary cooling loop remains fully operational, with the heat exchangers functioning efficiently to dissipate the residual heat.

- **Loss of Coolant Accident (LOCA):** This accident examines when the primary cooling system is compromised, leading to the escape of coolant from the system. To be conservative, the hypothetical breach is positioned at the primary pump discharge line to increase the loss of coolant. The LOCA scenarios explore varying sizes of breaks at the same location. The reactor is shut down once the RPS trip points are reached. Under normal operational circumstances, the primary coolant pumps are independent of the RPS. However, the current NNS design has not yet finalized the trip system for the primary cooling pumps when the system pressure is disrupted. Therefore, we assume the primary pumps are deactivated once the RPS trip is triggered. The LOCA scenario assumes that the secondary cooling loop remains fully functional and unaffected by the primary system breach.

3.5. Computing Safety Margins

To assess the thermal-hydraulic safety of the NNS, one safety criterion is considered: the blistering temperature. Literature reports a blistering temperature for U-Mo aluminum-clad fuels in the range of 638 K to 823 K [7], and the NBSR adopts a blistering temperature criterion of 723 K [2]. Studies provide correlations for the blistering temperature, with suggested temperature limits based on lower bound of the 95% confidence interval as a function of the maximum fission density in the plates [8]. Based on this data, the literature suggests a safety limit of 645 K through the maximum fission density of $4.5 \times 10^{21} \text{ cm}^{-3}$ relevant for the NNS, which is the ultimate bounding criterion given that exceeding this temperature increases the risk of fuel failure and release of radiation to the staff and the public. Three additional safety margins are also considered: the critical heat flux ratio (CHFR, subsection 3.5.1), the onset of flow instability ratio (OFIR, 3.5.2), and the onset of nucleate boiling ratio (ONBR, 3.5.3). Each of these margins consists of the ratio between a heat flux at which a certain level of boiling occurs and the local heat flux encountered by the flow in the analyzed configuration. In the cases of the critical heat flux (CHF) and the onset of nucleate boiling (ONB), each of those heat fluxes refer to a specific point on the boiling curve pioneered by Shiro Nukiyama [9]. The curve is illustrated in Figure 8 by plotting the heat flux of the wall as a function of the difference between the wall (i.e., the FP surface temperature) and

coolant saturation temperature ($T_{wall} - T_{sat}$). Note that the ONB precedes CHF, and therefore is a more conservative measure of the thermal-hydraulics safety in the coolant channels. Much like the NBSR, the NNS is not a pressurized system (i.e., no pressurizer), and any non-atmospheric pressure conditions are due to either hydrostatic or dynamic pressure loading from the system. So, we expect to see some bubbling in accident scenarios that cause excessive heating. Such bubbling is manageable if it remains below the CHF. If a local channel reaches CHF, it shall experience nearly immediate burnout, essentially making the jump from the CHF point to the burnout point in Figure 8. Although ONBR is the more limiting safety criterion, CHF is the criterion that signifies the NNS reaching highly undesirable and severe operating conditions (i.e., burnout).

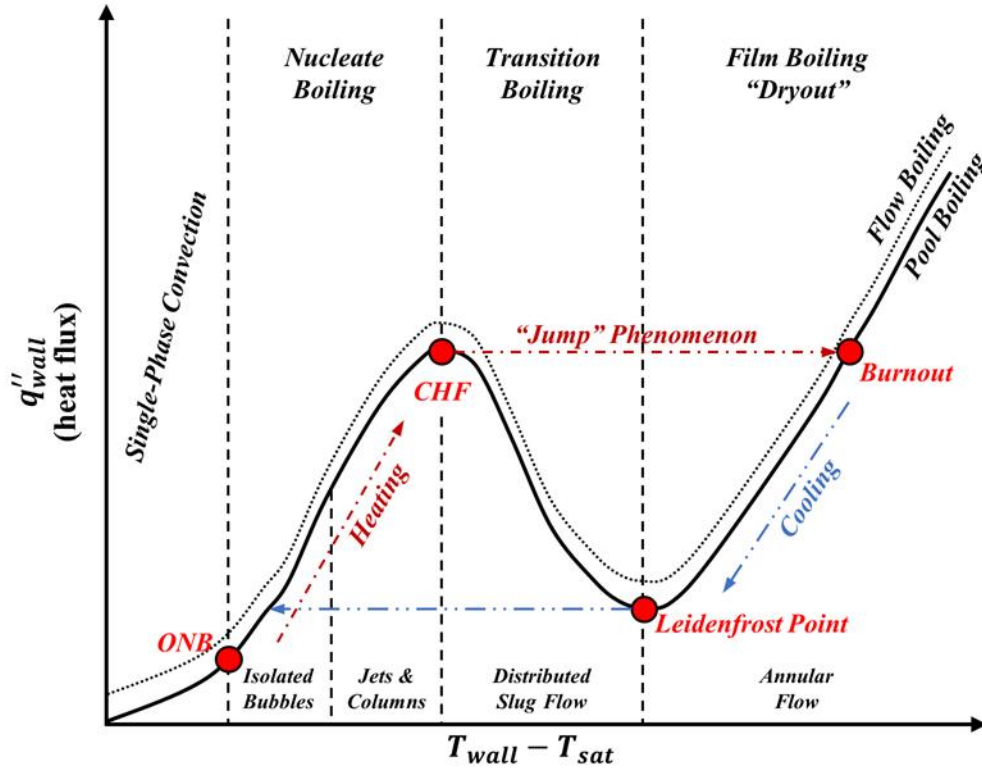


Figure 8. A Nukiyama-style boiling curve with added labels relevant to this work.

When looking for the thermodynamic properties for a given fluid, one must account for both temperature and pressure—meaning the thermal and hydraulic conditions of the fluid must be considered. Although both the FP’s heat flux and its proximity to the coolant saturation temperature (T_{sat}) are relevant, they are not the only relevant parameters. The hydraulic parameters of the coolant’s mass flow rate (\dot{m}) and the pressure drop in the channel (ΔP) are relevant parameters that should be considered when assessing the safety of the NNS. The curve in Figure 9 illustrates the importance of the hydraulic parameters, which notes various points of interest on the curve including ONB. The point of net vapor generation (NVG), also referred to as the onset of significant voiding (OSV), is a relevant parameter usually considered and grouped with the onset of flow instability (OFI). In Figure 9, the ONB is still the most limiting parameter. But OFI is the point at which the flow may experience a Ledinegg static instability [10] causing more severe operating conditions than bubbling.

As the \dot{m} in a channel is reduced, there is a point reached where boiling occurs, which is the ONB. At a later point, significant amounts of vapor will be generated in the channel, which is the OSV or NVG point. This increased presence of vapor will increase the ΔP . When the effect is significant enough, the ΔP increase will overwhelm the ΔP decrease resulting from the flow decrease, which leads to the OFI point. At this point of OFI, the overall ΔP in the heated channel will increase and flow will decrease, causing the Ledinegg flow instability. This results in a rapid loss of adequate cooling for the FPs. Therefore, similar to the CHF-ONBR relationship mentioned earlier, the ONBR is more limiting (conservative) than OFIR. But OFIR is the criterion that signifies the NNS reaching undesirable flow conditions (i.e., the Ledinegg instability).

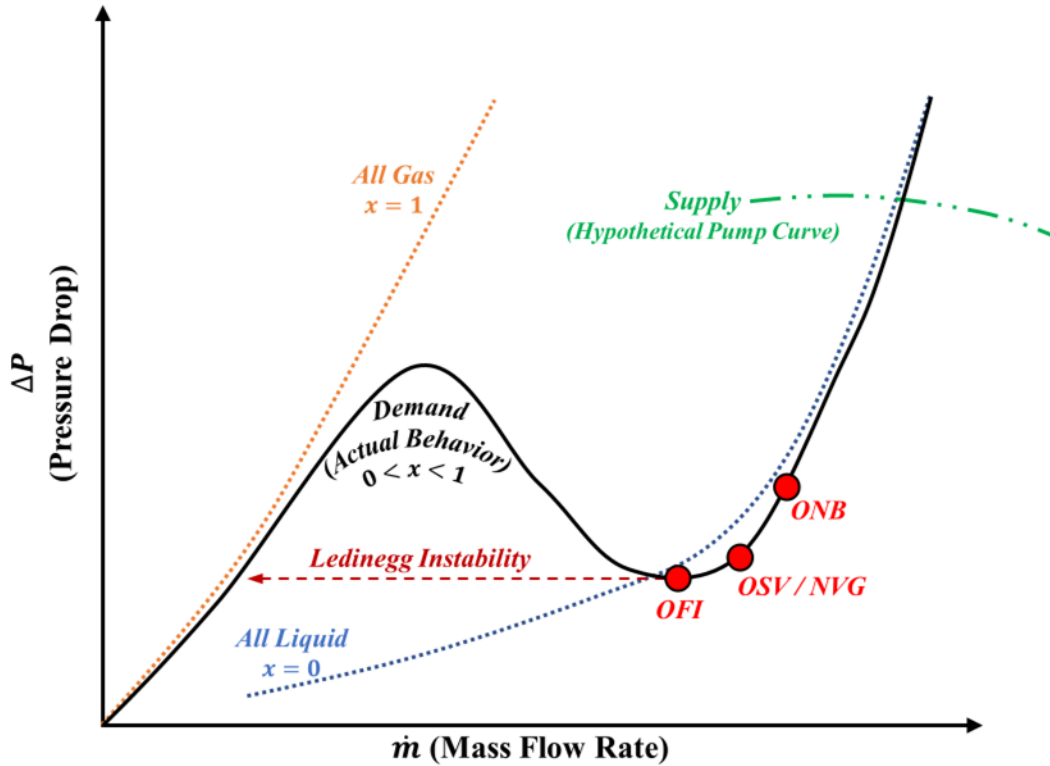


Figure 9. An illustration of the Ledinegg instability with relevant labels shown.

3.5.1. Critical Heat Flux Ratio (CHFR)

The CHFR is defined by Eq. (2), which is the ratio of the critical heat flux (CHF) to the local heat flux q''_n at a location n . n is often the location with the hottest temperature, which is either the hot channel, or the hot stripe (a certain finite volume within a channel). Note that the hot stripe can be in a channel that is colder than other channels, and it is not necessary for it to lie in the hot channel.

$$CHFR_n = \frac{CHF_n}{q''_n} \quad (2)$$

The CHF is obtained via correlations from literature: regarding this work the correlations are from Mirshak [11] and Sudo-Kaminaga [12]. Both have been effective for safety analyses in the NBSR

[2, 13]. Sudo-Kaminaga in particular has been used by other facilities including the MITR [14]. The following parts summarize each of the correlations' approaches to computing CHF.

3.5.1.1. Mirshak (1959) Correlation

The Mirshak correlation is based on fits from water heating data on experiments with downflowing water in rectangular channels. The correlation has Reynolds numbers in the ranges of $9 \times 10^3 - 2 \times 10^5$, with one side of the channel heated electrically to cause burnout and measure CHF. As a result of 65 burnout tests, an empirical correlation for the CHF was found, which can be represented in Eq. (3). In Eq. (3), V_∞ is the flow velocity (in units of m/s), P is the coolant pressure (in units of bar), and T_{sat} and T_∞ are the saturation and coolant temperatures, respectively (in units of °C). This correlation has been used at the NBSR to compute CHF and provides results deemed appropriate for safety assessments.

$$CHF = 1.51 \times 10^6 (1 + 0.1198 V_\infty)(1 + 0.00914[T_{sat} - T_\infty]) (1 + 0.19P) \quad (3)$$

3.5.1.2. Updated Sudo-Kaminaga (1998) Correlations

The Sudo-Kaminaga correlations are a set of correlations that describe the CHF in a rectangular channel with heating on two sides of the channel. They were proposed for the Japanese Research Reactor (JRR-3), and they covered a wide range of coolant flow rates in both upflow and downflow conditions. They rely on a dimensionless mass flux (G^*), which is computed per Eq (4) as a function of the mass flow rate (\dot{m}), the critical wave length (λ), the acceleration due to gravity (g), and the coolant's mass density in liquid and gaseous phases (ρ_l and ρ_g , respectively). Note that λ is a function of the coolant's surface tension (σ_∞). The correlations also rely on the dimensionless subcooling (ΔT_{sub}^*), which is presented in Eq. (5) as a function of the specific heat (c_p) and the latent heat for vaporization (h_{fg}).

$$G^* = \frac{\dot{m}}{A_{flow} \sqrt{\lambda g \rho_g (\rho_l - \rho_g)}}, \quad \lambda = \sqrt{\frac{\sigma_\infty}{g (\rho_l - \rho_g)}} \quad (4)$$

$$\Delta T_{sub}^* = c_p \frac{T_{sat} - T_\infty}{h_{fg}} \quad (5)$$

Depending on the flow conditions, the CHF is computed per one of four different formulae presented in Eq. (7)-(10). Note that A_{flow} and A_{heat} are the flow and heated areas, respectively, while w is the channel width. The factor f_1 from Eq. (6) is used to dimensionalize heat fluxes in physical units.

$$f_1 = h_{fg} \sqrt{\lambda g (\rho_l - \rho_g) \rho_g} \quad (6)$$

$$CHF_1 = 0.005 |G^*|^{0.611} f_1 \quad (7)$$

$$CHF_2 = \frac{A_{flow}}{A_{heat}} |G^*| \Delta T_{sub,in}^* f_1 \quad (8)$$

$$CHF_3 = 0.7 \frac{A_{flow}}{A_{heat}} \frac{\sqrt{w/\lambda}}{1 + \sqrt[4]{\rho_g/\rho_l}} (1 + 3\Delta T_{sub,in}^*) f_1 \quad (9)$$

$$CHF_4 = CHF_1 \left(1 + \frac{5000}{|G^*|} \Delta T_{sub,out}^* \right) \quad (10)$$

The selection of CHF correlation is based on the G^* value and how it relates to two other mass fluxes $G_1^* - G_2^*$ in Eq. (11)-(12), separating low-medium-high mass flux flows. The logic for selection is summarized in Eq. (13).

$$G_1^* = \left(\frac{0.005}{\frac{A_{flow}}{A_{heat}} \Delta T_{sub,in}^*} \right)^{\frac{1}{0.389}} \quad (11)$$

$$G_2^* = \left[140 \frac{A_{flow}}{A_{heat}} \frac{\sqrt{w/\lambda}}{(1 + \sqrt[4]{\rho_g/\rho_l})^2} (1 + 3\Delta T_{sub,in}^*) \right]^{\frac{1}{0.611}} \quad (12)$$

$$CHF = \begin{cases} G^* \leq G_2^*, & CHF_3 \\ G_2^* < G^* < G_1^*, & \begin{cases} CHF_1, & \text{upflow} \\ \max(CHF_2, CHF_3), & \text{downflow} \end{cases} \\ G^* \geq G_1^*, & \min(CHF_2, CHF_4) \end{cases} \quad (13)$$

3.5.2. Onset of Flow Instability Ratio (OFIR)

The onset of flow instability ratio can be computed per Eq. (2), which is the ratio of the relevant heat flux at low flow to the local heat flux q_n'' at a location n . We consider two heat flux correlations: the Costa correlation [15] and the Saha-Zuber correlation [16]. Both of those correlations predict the heat flux at the point of onset of significant voiding (q_{OSV}'') or at the point of net vapor generation (q_{NVG}''), which can be used to compute the OFIR shown in Eq. (14).

$$OFIR_n = \frac{q_{NVG,n}''}{q_n''} \equiv \frac{q_{OSV,n}''}{q_n''} \quad (14)$$

3.5.2.1. Costa (1969) Correlation

The Costa correlation is useful for finding the heat flux at the point of OSV (Figure 9), and it was used for the NBSR and for High Flux Isotope Reactor (HFIR) at the Oak Ridge National Laboratory for their safety analyses. This correlation is only limiting at low flow and low subcooling, where significant amounts of vapor are generated prior to achieving CHF. Being a predictor of this OSV makes it a conservative choice for the OFIR. See the correlation in Eq. (15) as a function of the coolant velocity (V_∞) and the saturation and bulk coolant temperatures (T_{sat} and T_∞ , respectively). All units are in SI units.

$$q''_{OSV} = (T_{sat} - T_\infty) \frac{\sqrt{100 V_\infty}}{1.28} \quad (15)$$

3.5.2.2. Saha-Zuber (1974) Correlation

The Saha-Zuber correlation is useful for predicting the heat flux at the point of NVG (Figure 9), and it was used in other research reactors as well. See the correlation in Eq. (16), where Pe is the Peclet number, k is the thermal conductivity of the coolant, and D_h is the hydraulic diameter of the channel. Note that Pe can be computed as a product of the Reynolds and Prandtl numbers, and it represents the ratio of advective transport rate to the mass diffusion rate. All units are in SI units.

$$q''_{NVG} = \begin{cases} 0.0065 \frac{\dot{m} c_p (T_{sat} - T_\infty)}{A_{flow}}, & Pe \leq 70,000 \\ 455 \frac{k (T_{sat} - T_\infty)}{D_h}, & Pe > 70,000 \end{cases} \quad (16)$$

3.5.3. Onset of Nucleate Boiling Ratio (ONBR)

The ONBR, the most limiting of the three margins, is utilized in some research reactors as a safety criterion. It provides an indication of whether flow is in the liquid phase or if it started bubbling. It is computed per Eq. (17) as the ratio of the heat flux at ONB (q''_{ONB}) to the local heat flux q''_n at a location n . We use the Bergles-Rohsenow [17] correlation to determine q''_{ONB} .

$$ONBR_n = \frac{q''_{ONB,n}}{q''_n} \quad (17)$$

3.5.3.1. Bergles-Rohsenow (1964) Correlation

The Bergles-Rohsenow correlation is based on experiments with water heated by stainless steel and nickel surfaces. The experiments encompassed a range of pressures from 1.02 to 138 bar,

which is within the range of the NNS's expected operating pressure. The correlation is shown in Eq. (18) as a function of pressure (P in bar) and wall temperature (T_{wall} in °C).

$$q''_{ONB} = (1.0829 \times 10^3) P^{1.156} (1.8[T_{wall} - T_{sat}])^{2.16}/P^{0.0234} \quad (18)$$

3.6. CFD Models

Using system codes like TRACE or RELAP [18] is sufficient for light-water research reactors using material test reactor (MTR) type fuel as demonstrated by safety analyses of the NBSR [2], the Open-pool Australian Lightwater reactor (OPAL) [3], and the Massachusetts Institute of Technology Reactor (MITR) [14]. This is true for the NNS as well. However, there are a variety of NNS design features expected to affect the performance and safety of the reactor. Such features include triple-channel mixing at the inlet preceding the FPs, high velocities in the coolant channels, reliance on natural circulation for cooling said channels in some transients, and a buoyancy-affected mixing plenum at the outlet of the core. Such features are discussed further in the following subsection 3.6.1 of the report, and they are the basis for the CFD work on the NNS. Note that CFD tools are not expected to be used for the NNS safety analysis report, but they are used to assist design and optimization efforts. The CFD studies would be supplemental-to and auxiliary-from the NNS safety assessments. The CFD work would be as generic as possible to improve its usage for multiple designs and to assist in understanding the flow behavior primarily from a phenomenological perspective. Additional discussions on the CFD models and relevant physical phenomena are introduced in subsection 3.6.1 and elaborated on in sections 6.1-6.3.

3.6.1. Identifying Regions of Interest

A section view of the current NNS core design is in Figure 10, where three regions are identified. Note that all regions are affected by design features including the cold legs, the lower grid (or legs), the row window in the inlet region leading up to the active height (the coolant channels), the annular reflector tank concentric with the core, and the chimney encasing the flow out of the core in the outlet region.

- Inlet Region (**solid red**) includes turbulent separation and mixing phenomena.
- Active Height Region (**dashed orange**) includes wall-heated curved flow channels.
- Outlet Region (**dash-dotted blue**) includes a mixing plenum with buoyancy effects.

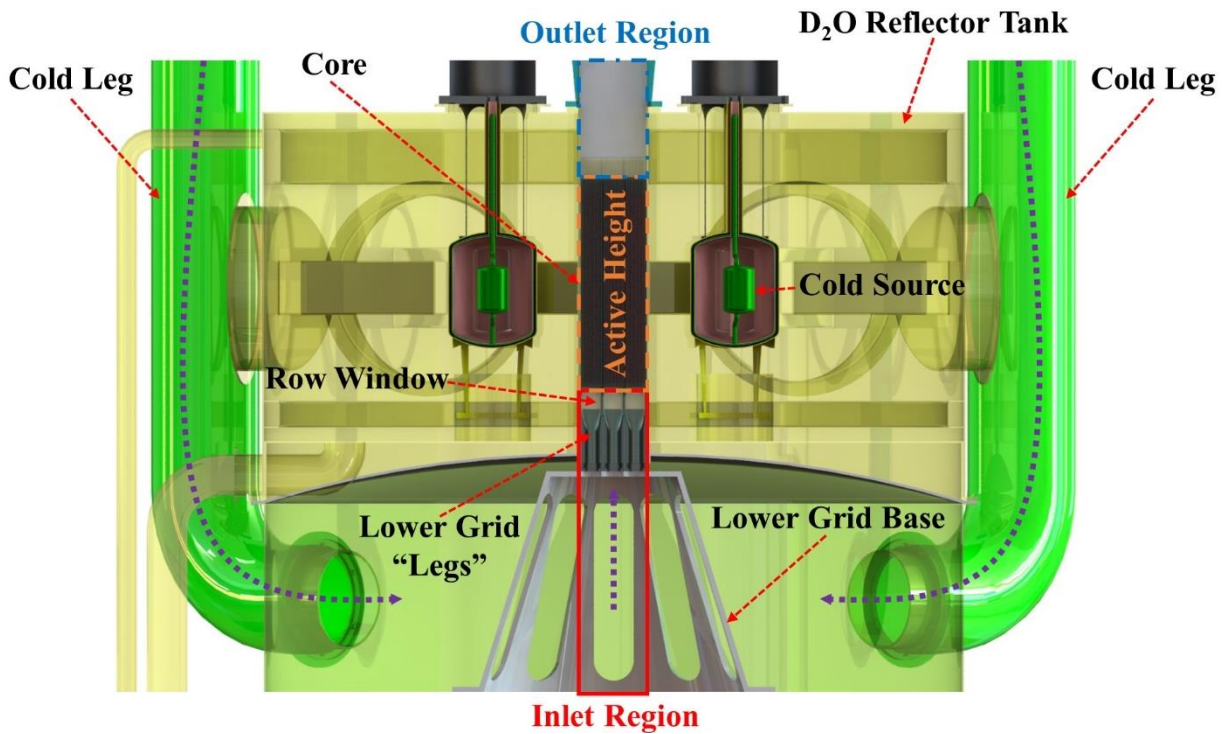


Figure 10. A section view of the NNS highlighting distinct design features and identified regions of interest for CFD work.

The inlet region contains design features that enable both turbulent separation and mixing upstream of the coolant channels providing cooling to the FPs. This prompts questions regarding the hydraulic development of the flow including the mixing length and the uniformity of the coolant velocity entering the coolant channels in each FA. Uncovering any potential bias in the flow distribution (i.e., more flow going towards the outer FAs as opposed to the inner FAs) requires CFD and/or experimental flow investigations of parallel channel mixing and separation. More details on the inlet region are discussed in section 6.1.

The active height region requires an understanding of the validity of existing thermal-hydraulics safety margins correlations (such as Sudo-Kaminaga [12]) for usage in the NNS coolant channels with the NNS inlet flow characteristics and geometry. This includes understanding the validity of the existing correlations for describing the safety margins during natural circulation cooling in some accident scenarios. More details on the active height region are discussed in section 6.2.

The outlet region serves as a mixing plenum for all coolant channels exiting the FAs and entering the chimney. The chimney itself is open to the pool; it is also connected to a hot leg for circulating the flow back towards the primary pumps (Figure 1). This requires understanding mixed convection flows (buoyancy and forced flow effects), which is difficult for any model to capture, including a CFD model. Investigating this will require heavy explorations of different modeling approaches and potential experimental work—all of which could be pursued in future works. Section 6.3 offers some preliminary characterization of the expected flow phenomena at the outlet of the core.

3.6.2. Turbulence Modeling

Modeling turbulence can be performed with various levels of fidelity [19, 20]. A modeler may choose to resolve all scales of motion down to the smallest dissipative length scale (known as the Kolmogorov length scale [21–24]), which is a turbulence modeling approach called Direct Numerical Simulation (DNS). A modeler may choose to resolve scales down to a certain length, and then model the smaller length scales, employing a Large Eddy Simulation (LES). A modeler may choose to model all scales of motion by averaging across them, which is the implementation for Reynolds-Averaged Navier-Stokes (RANS) models. Note that there are hybrids in-between, including Partially-Averaged Navier-Stokes (PANS) models [25, 26], but they are not as developed as the other three turbulence modeling techniques. DNS is most accurate, but it is more computationally expensive. LES is less computationally expensive than DNS, but more expensive than RANS models.

Although RANS is the least accurate of the mentioned modeling approaches, it is the most feasible for complex geometries. Modern computational capabilities can run both RANS and LES models in a reasonable amount of runtime. However, LES presents a greater challenge when setting up the simulations; and it may not be necessary if RANS can provide an acceptable level of fidelity and accuracy for the use-case. We preferred RANS over LES or PANS due to the preliminary nature of the work on NNS. But PANS or LES may be considered for future studies if deemed necessary. We considered several RANS models and we provide a brief overview in parts of this report.

3.6.2.1. General RANS Modeling Approach

The RANS models utilize averaged forms of the Navier-Stokes equations, shown in Eq. (19)-(20). In the RANS equations, $\langle U_i \rangle$ is the averaged form of any i -th component of the velocity and $\langle P \rangle$ is the averaged pressure, where both are dependent on the kinematic viscosity ν and the Reynolds stresses $\langle u_i u_j \rangle$. The Reynolds stresses prevent a real solution from being reached and require a model to solve the RANS equations. The Boussinesq approximation shown in Eq. (21) is a common closure model, which relies on the turbulent kinetic energy (k) and the turbulent viscosity (ν_t) to close the RANS equations. This closure is the primary distinction between each of the RANS models.

$$\frac{\partial \langle U_i \rangle}{\partial t} + \langle U_i \rangle \frac{\partial \langle U_i \rangle}{\partial x_j} = -\frac{\partial \langle P \rangle}{\partial x_i} - \frac{\partial \langle u_i u_j \rangle}{\partial x_j} + \nu \frac{\partial^2 \langle U_i \rangle}{\partial x_j \partial x_j} \quad (19)$$

$$\frac{\partial^2 \langle P \rangle}{\partial x_j \partial x_j} = -2 \frac{\partial \langle U_i \rangle}{\partial x_j} \frac{\partial \langle U_j \rangle}{\partial x_i} - \frac{\partial^2 \langle u_i u_j \rangle}{\partial x_j \partial x_j} \quad (20)$$

$$\langle u_i u_j \rangle = \frac{2}{3} k \delta_{ij} - \nu_t \left(\frac{\partial \langle U_i \rangle}{\partial x_j} + \frac{\partial \langle U_j \rangle}{\partial x_i} \right) \quad (21)$$

3.6.2.2. Standard k - ϵ Model

The 2-equation RANS turbulence models are the most common. One such model is the standard k - ϵ model [27], which relies on modeling the k transport per Eq. (22), and the turbulent dissipation rate (ϵ) per Eq. (23). Both the k and ϵ transport equations rely on ν_t , which is modeled in Eq. (24). Note that standard k - ϵ (like other turbulence models) rely on model coefficients to solve such as C_μ . Each of those coefficients can be derived from different turbulence experiments [28]. For $C_{\epsilon 2}$, decaying isotropic turbulence experimental data can be used with the assumption of homogeneity to derive an acceptable range of values for most flows, with the range of 1.6-1.95 being acceptable for most simulations relevant to the CFD community. With $C_{\epsilon 2}$ known, data from homogenous shear turbulence (or Couette flow) can be used to calculate $C_{\epsilon 1}$, which is often in the range of 1.34 to 1.51. With $C_{\epsilon 1}$ and $C_{\epsilon 2}$ known, the model coefficient C_μ can be calculated, which fits within a range of values between 0.05 and 0.16. The remaining coefficients, σ_k and σ_ϵ , can be calculated via turbulent boundary layer experiments and by utilizing knowledge of the other model coefficients. The values used for the standard k - ϵ model coefficients are tabulated in Table 7, which follow recommendations from Launder and Spalding [29], and applications by El-Tahry [30].

$$\frac{\partial k}{\partial t} + \langle U_j \rangle \frac{\partial k}{\partial x_j} = -\langle u_i u_j \rangle \frac{\partial \langle U_i \rangle}{\partial x_j} - \epsilon + \frac{\partial}{\partial x_j} \left(\left[\nu + \frac{\nu_t}{\sigma_k} \right] \frac{\partial k}{\partial x_j} \right) \quad (22)$$

$$\frac{\partial \epsilon}{\partial t} + \langle U_j \rangle \frac{\partial \epsilon}{\partial x_j} = -C_{\epsilon 1} \frac{\epsilon}{k} \langle u_i u_j \rangle \frac{\partial \langle U_i \rangle}{\partial x_j} - C_{\epsilon 2} \frac{\epsilon^2}{k} + \frac{\partial}{\partial x_j} \left(\left[\nu + \frac{\nu_t}{\sigma_\epsilon} \right] \frac{\partial \epsilon}{\partial x_j} \right) \quad (23)$$

$$\nu_t = C_\mu \frac{k^2}{\epsilon} \quad (24)$$

Table 7. The values used for the standard k - ϵ model in this work.

C_μ	$C_{\epsilon 1}$	$C_{\epsilon 2}$	σ_k	σ_ϵ
0.09	1.44	1.92	1.0	1.3

Although this model is very popular in practical applications (such as industrial applications), its popularity is not attributed to its accuracy, but rather to its low computational costs relative to more sophisticated RANS models. The standard k - ϵ model was developed with high Re flows in-mind, making it less favorable for low Re flows. This is a reason why the standard k - ϵ model struggles in modeling near-wall and turbulent-boundary-layer behavior. Regardless of its flaws, it usually provides a good starting point for most CFD modeling work; so it is valuable to model flows despite its limitations.

3.6.2.3. Standard k - ω Model

Another common and well-known 2-equation RANS model is the standard k - ω model [31], which models the titular k and ω transport equations shown in Eq. (25) and Eq. (26), respectively. In this model, ω is the specific dissipation rate. Note there are altered model coefficients: C_μ from the standard k - ϵ model is replaced by β^* ; and the other coefficients can be obtained from relevant experimental and empirical findings similar to the k - ϵ model. The ν_t is found using Eq. (27).

$$\frac{\partial k}{\partial t} + \langle U_j \rangle \frac{\partial k}{\partial x_j} = -\langle u_i u_j \rangle \frac{\partial \langle U_i \rangle}{\partial x_j} - \beta^* k \omega + \frac{\partial}{\partial x_j} \left([\nu + \nu_t \sigma^*] \frac{\partial k}{\partial x_j} \right) \quad (25)$$

$$\frac{\partial \omega}{\partial t} + \langle U_j \rangle \frac{\partial \omega}{\partial x_j} = -\alpha \frac{\omega}{k} \langle u_i u_j \rangle \frac{\partial \langle U_i \rangle}{\partial x_j} - \beta \omega^2 + \frac{\partial}{\partial x_j} \left([\nu + \nu_t \sigma] \frac{\partial \omega}{\partial x_j} \right) \quad (26)$$

$$\nu_t = \frac{k}{\omega} = \beta^* \frac{k^2}{\epsilon} \quad (27)$$

Table 8. The values used for the standard k - ω model in this work.

β^*	α	β	σ^*	σ
0.09	0.5	0.075	0.5	0.5

Note that this model was first proposed by Kolmogorov in 1942 [32], but later improved by Wilcox [19]. This k - ω model and its implemented coefficients are consistent with Wilcox's recommendations. This model's adoption of ω improves modeling near-wall behavior of flows than the standard k - ϵ model, since k - ω was calibrated for shear-dominated flows. Although it performs better near-wall, the k - ω model coefficients were found at steady state, which makes it limiting for modeling transient behaviors of flows. Further, the model struggles in low Re regions of undeveloped turbulence. Its adoption of a linear constitutive relation can be limiting for certain flows, which includes mixing flows. Like k - ϵ , this model provides a good starting point for the CFD studies.

3.6.2.4. k - ω SST Model

The k - ω Shear Stress Transport (SST) model [33, 34] acts as a hybrid of the standard k - ϵ and k - ω models, where the k - ω model is employed near-wall and the k - ϵ model is employed elsewhere (i.e., in the freestream). The substitution between ϵ and ω away-from and near-to walls of a domain produce a cross-diffusion term between k and ω , which uses a blending function to smoothen the transition between the two models. This requires an adjustment to the ω transport equation, shown in Eq. (26), by adding a term at the end yielding the form shown in Eq. (28). Some of the model coefficients are defined in Eq. (29)-(31) while others are constants as in Table 9.

$$\frac{\partial \omega}{\partial t} + \langle U_j \rangle \frac{\partial \omega}{\partial x_j} = -\alpha S^2 - \beta \omega^2 + \frac{\partial}{\partial x_j} \left([\nu + \nu_t \sigma_{\omega 1}] \frac{\partial \omega}{\partial x_j} \right) + 2(1 - F_1) \frac{\sigma_{\omega 2}}{\omega} \frac{\partial k}{\partial x_i} \frac{\partial \omega}{\partial x_i} \quad (28)$$

$$v_t = \frac{\alpha_1 k}{\max(\alpha_1 \omega, SF_2)}, \quad \left\{ \begin{array}{l} \alpha_1 = 5/9 \\ F_2 = \tanh \left(\left[\max \left(\frac{2\sqrt{k}}{\beta^* \omega y}, \frac{500\nu}{y^2 \omega} \right) \right]^2 \right) \\ S = \frac{\omega}{k} \langle u_i u_j \rangle \frac{\partial \langle U_i \rangle}{\partial x_j} \end{array} \right. \quad (29)$$

$$F_1 = \tanh \left(\left[\min \left(\max \left[\frac{\sqrt{k}}{\beta^* \omega y}, \frac{500\nu}{y^2 \omega} \right], \frac{4\sigma_{\omega 2} k}{CD_{k\omega} y^2} \right) \right]^4 \right) \quad (30)$$

$$CD_{k\omega} = \max \left(\frac{2\sigma_{\omega 2}}{\omega} \frac{\partial k}{\partial x_i} \frac{\partial \omega}{\partial x_i}, 10^{-10} \right) \quad (31)$$

Table 9. The values used for the k - ω SST model constants in this work.

α_1	α_2	β_1	β_2	β^*	σ_{k1}	σ_{k2}	$\sigma_{\omega 1}$	$\sigma_{\omega 2}$
5/9	0.44	3/40	0.0828	0.09	0.85	1.0	0.5	0.856

Note how v_t is defined different for the SST model when compared to the previous 2-equation models. This allows it to consider the influence of the shear stress component as in the half-equation model of Johnson and King [35]. This allows the SST model to offer significant improvements over the k - ϵ and k - ω models when simulating flows with strong adverse pressure gradients (like mixing flows). This transition and usage of k - ω in the inner parts of the boundary layer improves the usability of the SST model for low Re turbulent flows without reliance on damping functions. However, note that the SST model tends to dramatize turbulent effects in regions with stagnating pressure or strong acceleration (i.e., large normal strain regions).

3.6.2.5. Realizable k - ϵ Model

The Realizable k - ϵ model is a variant of the standard k - ϵ model, which reformulates Eq. (23) to the form shown in Eq. (32). Note the addition of a new term to the ϵ transport equation, which relies on coefficients and variables defined in Eq.(33). The model adjusts C_μ to satisfy the realizability of the Reynolds stresses $\langle u_i u_j \rangle$, where C_μ can be computed via Eq. (34) as a function of the shear velocity (U^*) and the model constants A_0 and A_5 . Note that A_5 is a function of the shear stress ratio (W), which is discussed further in literature [36, 37]. In this work, the remaining model constants for realizable k - ϵ are identical to the ones adopted for the standard k - ϵ model shown in Table 7.

$$\frac{\partial \epsilon}{\partial t} + \langle U_j \rangle \frac{\partial \epsilon}{\partial x_j} = -C_{\epsilon 1} \frac{\epsilon}{k} \langle u_i u_j \rangle \frac{\partial \langle U_i \rangle}{\partial x_j} - C_{\epsilon 2} \frac{\epsilon^2}{k + \sqrt{\nu \epsilon}} + \frac{\partial}{\partial x_j} \left(\left[\nu + \frac{\nu_t}{\sigma_\epsilon} \right] \frac{\partial \epsilon}{\partial x_j} \right) + C_1 \epsilon \sqrt{2S_{ij} S_{ij}} \quad (32)$$

$$S_{ij} = \frac{1}{2} \left(\frac{\partial \langle U_j \rangle}{\partial x_i} + \frac{\partial \langle U_i \rangle}{\partial x_j} \right), \quad C_1 = \max \left(0.43, \frac{\eta}{\eta + 5} \right), \quad \eta = \sqrt{2S_{ij} S_{ij}} \frac{k}{\epsilon} \quad (33)$$

$$C_\mu = \frac{1}{A_0 + A_s \frac{k U^*}{\epsilon}}, \quad \begin{cases} A_0 = 4.04 \\ A_s = \sqrt{6} \cos\left(\frac{1}{3} \cos^{-1}[\sqrt{6} W]\right) \end{cases} \quad (34)$$

The alterations offered by the realizable variant of k - ϵ enable greater generalizability and makes it more applicable to flow topologies that are more complex than a single channel or a pipe. The adjusting dynamic of C_μ offers greater sensitivity of the model to flow topology and improves the prediction of mean flow quantities [38]. This makes the model more applicable than the standard k - ϵ for simulating non-equilibrium turbulence like rapid distortion. Like all other RANS models, Realizable k - ϵ is not without limitations, as it faces challenges from its adoption of the Boussinesq approximation. In particular, the model is limiting when simulating swirling flows and secondary flows in rectangular ducts, both representing relevant flow topologies in the regions of interest identified in subsection 3.6.1.

3.6.2.6. Spalart-Allmaras Model

Spalart-Allmaras model [39] is a 1-equation model that is useful and computationally efficient for low Re flows. This model relies on v_t transport equations shown in Eq. (35). This model depends on a variety of model coefficients, some of which are described in Eq. (36)-(38), while others are constants shown in Table 10. This report will be limited to the description of the model shown below, but additional information on the model can be found in Spalart and Allmaras's original work [39]. Note we use the original model coefficients used by Spalart and Allmaras, but not the Dacles-Mariani modification [40].

$$\frac{\partial \tilde{v}}{\partial t} + \langle U_j \rangle \frac{\partial \tilde{v}}{\partial x_j} = -c_{b1} \tilde{S} \tilde{v} - c_{w1} f_w \left(\frac{\tilde{v}}{d}\right)^2 + \frac{1}{\sigma} \frac{\partial}{\partial x_k} \left[(v + \tilde{v}) \frac{\partial \tilde{v}}{\partial x_k} \right] + \frac{c_{b2}}{\sigma} \frac{\partial \tilde{v}}{\partial x_k} \frac{\partial \tilde{v}}{\partial x_k} \quad (35)$$

$$v_t = \tilde{v} f_{v1}, \quad f_{v1} = \frac{\chi^3}{\chi^3 + c_{v1}^3}, \quad f_{v2} = 1 - \frac{\chi}{1 + \chi f_{v1}}, \quad \chi = \frac{\tilde{v}}{v} \quad (36)$$

$$f_w = g \left[\frac{1 + c_{w3}^6}{g^6 + c_{w3}^6} \right]^{1/6}, \quad g = r + c_{w2}(r^6 - r), \quad r = \frac{\tilde{v}}{\tilde{S} \kappa^2 d^2} \quad (37)$$

$$\tilde{S} = S + \frac{\tilde{v}}{\kappa^2 d^2} f_{v2}, \quad S = \sqrt{2\Omega_{ij}\Omega_{ij}}, \quad \Omega_{ij} \equiv \frac{1}{2} \left(\frac{\partial u_i}{\partial x_j} - \frac{\partial u_j}{\partial x_i} \right) \quad (38)$$

Table 10. The values used for the Spalart-Allmaras model constants in this work.

c_{b1}	c_{b2}	c_{v1}	σ	c_{w1}	c_{w2}	c_{w3}	κ
0.1355	0.622	7.1	2/3	$\frac{c_{b1}}{\kappa^2} + \frac{1 + c_{b2}}{\sigma}$	0.3	2.0	0.41

3.6.2.7. Near-wall Modeling

Regardless of the adopted RANS model, it is challenging to model the behavior of flow near the wall due to the multi-scale nature of turbulence in the boundary layer. So, several wall models can be adopted, all of which make different assumptions regarding the evolution of the boundary layer. A wall model can be neglected if the mesh is fine near the wall (i.e., smaller finite volumes near the wall). Such mesh resolution near the wall would yield wall-resolved RANS models, which offer the most accurate simulation of near-wall behavior that RANS can offer. The level of fidelity required can be dictated by the modeler using a non-dimensional parameter known as y^+ , which represents the ratio of inertial to viscous forces for a fluid near any given wall boundary. A $y^+ \leq 1$ is considered small enough to reach a wall-resolved RANS model. Per Eq. (39), y^+ is a function of the mesh resolution near the wall (Δy), the dynamic viscosity of the fluid (ν), and the friction velocity (u_τ). The u_τ is a function of the wall shear stress (τ_w), which relies on the skin friction coefficient (C_f), fluid mass density (ρ), and the bulk velocity (U_∞) shown in Eq. (40). The C_f can be obtained via numerical or experimental correlations, and it varies depending on geometry and flow conditions. Assuming a turbulent boundary layer over a flat plate (with the 1/7 power law), the C_f can be estimated by Eq. (41), with limitations further discussed in literature [41].

$$y^+ = \frac{u_\tau \Delta y}{\nu}, \quad u_\tau = \sqrt{\frac{\tau_w}{\rho}} \quad (39)$$

$$\tau_w = \frac{1}{2} C_f \rho U_\infty^2 \quad (40)$$

$$C_f \approx 0.0576 Re^{-1/5} \quad (41)$$

4. Steady-State NNS Characteristics

Results from both steady-state TRACE models (the system model and the core model from section 3.2) are reported in this chapter. Steady-state thermal-hydraulics characteristics for the NNS from both steady-state models are reported in section 4.1. Safety margins from both steady-state models are also reported in section 4.2.

4.1. Thermal-hydraulic Behavior

The axial temperature distributions in the hot channel for each of the steady-state models are shown in Figure 11, where the coolant temperature (T_∞), the right-facing or outer clad temperature ($T_{c,o}$), and the left-facing or inner clad temperature ($T_{c,i}$) are shown. The left and right facing clad and the hot channel number are respective to Figure 2(b), where channel 1 in any given row is the left-most channel in that row, shown in Figure 2(b). The startup power profiles were used for the core model since we found them to be the most-limiting cycle state for the NNS (from a thermal-hydraulics perspective).

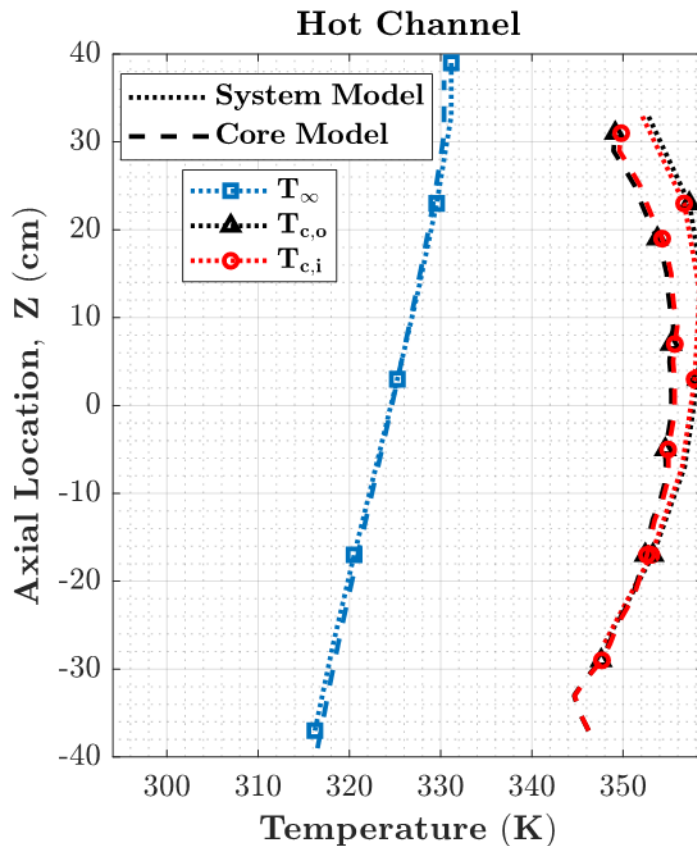


Figure 11. Axial temperature distributions in the hot channel according to both the system model and the subchannel model (at startup). Note that axial centerline is at $Z = 0$ cm. The hot channel in the system model was channel 63 in row B. The hot channel in the core model was channel 2 in row A.

As the caption of Figure 11 indicates, each of the steady-state models predicted a different hot channel. The system model predicted channel 63 in row B is the hot channel, while the core model predicted the hot channel is the 2nd one in row A. This deviation is likely due to the flow distribution between the channels being modeled with greater fidelity in the core model, yielding differing pressure and flow profiles. Note that for the preconceptual neutronics analysis which has been completed and used as the basis for this work, the system model predicts hotter peak temperatures than the core model (at any cycle state), making it the more conservative model Table 11 provides a summarized comparison between the models' temperature predictions.

Table 11. An overview of the hottest temperature values according to both steady-state models.

		System Model		Core Model	
Hot Channel Location	Row	B	A		
	Channel #	63	2	System Model <i>at the core model's hot channel</i>	
Maximum Temperatures		T_{∞} (K)	331.16	330.38	331.10
		$T_{c,o}$ (K)	364.28	361.17	357.58
		$T_{c,i}$ (K)	364.38	360.38	358.07

The pressure results from both models are shown in Figure 12 and Table 12. On average, both models predict a pressure drop (ΔP) of approximately 2.7-2.8 bar, but variations can be observed depending on the channel location and the model used to compute the pressure. For both models, the pressure varied depending on whether the channel is an outer channel (channel 1 or channel 64) or whether it is an inner channel (remaining channels). That is, referencing Table 2 and Figure 2(b), the pressure profiles for the FA-FA and FP-FP channels matched those of the inner channels, whereas the chimney-FP and FP-chimney channels matched those of the outer channels. The models vary in their pressure prediction but lie within each other's bounds. The system model does not show variations between the columns, whereas the core model predicts that column #2 has unique profiles relative to columns #1 and #3. In particular, the core model predicts lower ΔP for the channels in column #2. The lower ΔP in column #2 is attributed to the reduced flow rates in the middle column relative to the other two columns as shown in Figure 13.

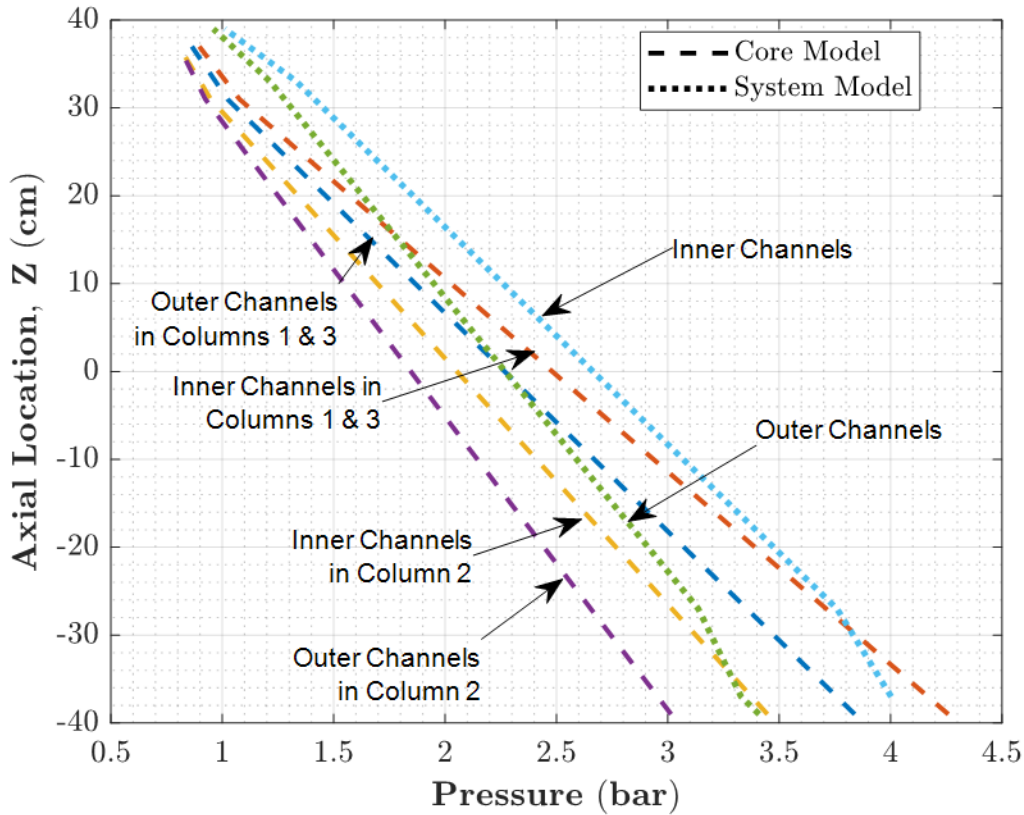


Figure 12. Axial pressure distributions in any channel in the core according to both the system model (dotted lines) and the subchannel model (dashed lines). Note that axial centerline is at $Z = 0$ cm.

Table 12. An overview of the computed pressure-drop values (ΔP) across the core according to both steady-state models.

	Location	ΔP (bar)	Average ΔP (bar)
System Model	Inner Channels	2.99	2.72
	Outer Channels	2.45	
Core Model	Inner Channels in Columns 1 & 3	2.98	2.80
	Outer Channels in Columns 1 & 3	3.36	
	Inner Channels in Column 2	2.64	
	Outer Channels in Column 2	2.21	

Figure 13 shows the mass flow rate (\dot{m}) in each of the channels in the core as modeled by both the core and system models. Note that the system model only models the outer 3 channels on each side of any row and lumps the rest of the channels in one equivalent channel (refer to Figure 6), which is why the system model only provides relevant data points in the outer 3 channels of any given row in the core. In contrast, the core model captures the \dot{m} in each of the channels, providing an understanding of the variation in the flow in each row and in each column. Note that the error

bars in Figure 13 are representative of the standard deviation in the \dot{m} along the height of the channel, and they are dramatized (scaled by a factor of 4×10^5 kg/s) to demonstrate which channels yield the most axially varied \dot{m} . This demonstrates the validity of utilizing a constant \dot{m} to describe the flow rate in any given channel. Note that this axial variation is not physical due to continuity, but it is the inadvertent consequence of numerical convergence errors (which are insignificant in magnitude).

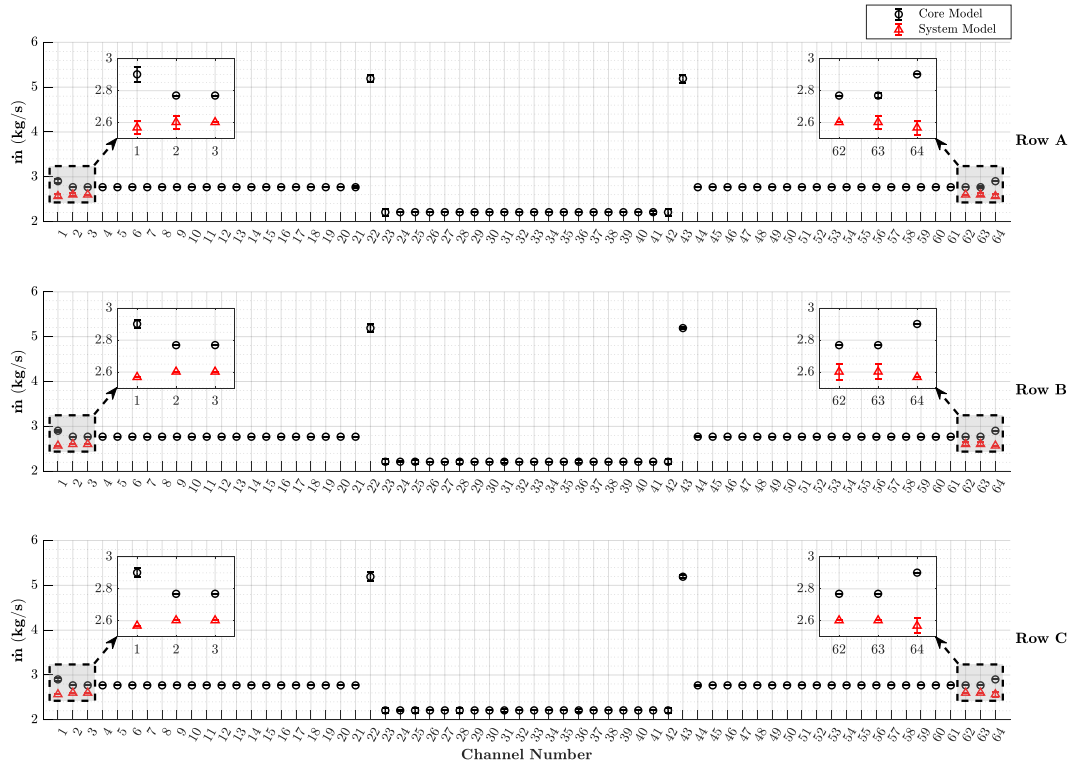


Figure 13. The mass flow rate distribution across the core according to the system model (red triangles) and the core model (black circles). Note that the error bars are scaled by a factor of 4×10^5 kg/s to improve graphical visibility.

In Figure 13, channels in the middle column (column 2) have lower \dot{m} than the rest, approximately 20% lower than channels in the outer columns. This reduction in flow is expected due to the triple-channel mixing behavior encountered at the inlet of each FA in any given row in the core, where the middle channel (middle column in this scenario) experiences notable decrement in velocity compared to the outer channels. This flow reduction is due to the middle column's inlet being bounded by two mixing layers, causing shearing in the flow on either side of the column, whereas the outer columns are bounded by only one mixing layer (and a boundary layer). A more detailed assessment of this behavior can be found in subsection 6.1 and in literature [42, 43]. This mixing is not modeled by default in TRACE, but it was incorporated in both models via the adopted nodalizations (Figure 6 and Figure 7).

4.2. Safety Margins

The safety margins for each of the NNS steady-state models are summarized and compared to NBSR’s safety margins in Table 13. Margins from both the high-enriched uranium (HEU) and proposed low-enriched uranium (LEU) cores for the NBSR are presented in Table 13 for comparison to the NNS steady-state models, where the NBSR data was obtained from the NBSR SAR [2] and the LEU conversion Preliminary SAR (PSAR) [44]. Results from all NBSR data sources are based on equilibrium core steady-state analyses. Note that the NBSR core does not have reportable ONBR data. ONB results from an assessment on the NBSR LEU design demonstration element in the experimental irradiation conditions are available in literature [45], which are not appropriate for this comparison to NNS. The NNS core model results in Table 13 reflect the most limiting cycle state of SU, whereas the margins for the remaining cycle states are in Table 14.

Table 13. A summary of the safety margins according to both steady-state models in comparison to NBSR safety margins with both HEU- and LEU-fueled NBSR cores. These are all at the hot channels (denoted in Table 11). Z_{hot} is the axial location relative to the center of the fueled zone in the core (negative being below the centerline, and positive being above the centerline).

Safety Margin	Correlation	NNS		NNS		NBSR	NBSR
		System		Core (SU)		HEU	LEU
		Value	Z_{hot} (cm)	Value	Z_{hot} (cm)	Value	Value
CHFR	Mirshak	3.03	-1	3.09	-13	3.04	-
	Sudo-Kaminaga	3.22	-1	3.28	-13	3.99	3.96
OFIR	Saha-Zuber	7.17	-11	7.22	-13	5.50	5.61
	Costa	5.62	-11	5.48	-13	-	-
ONBR	Bergles-Rohsenow	1.96	9	2.15	13	-	-

For CHFR, the NNS provides comparable results to the minimum computed for NBSR with Mirshak correlation; but it is lower for NNS than NBSR when using the Sudo-Kaminaga correlation. Based on the current assessment, the NNS’s CHFR margins are comparable to NBSR. For OFIR, the NNS yields larger margins than NBSR using either correlation, with the Costa correlation providing more conservative values under the evaluated steady-state conditions. The system model yields lower margins, making it the more conservative model to use for the accident analyses (identified in section 4.1). Both the NNS models yield ONBR values that are higher than unity, indicating that the NNS would maintain single-phase convection in steady-state operating conditions. Any remaining differences in comparison to NBSR are suitably analyzed and later work incorporating uncertainties since NBSR has substantial margins.

The evolution of the safety margins throughout a cycle in the NNS is shown in Table 14, where the most limiting conditions are observed during the SU cycle state, with the margins growing as the cycle progresses to EOC. Note that the position of the minimum safety margin changes throughout the cycle, which is reflected in Table 15. This demonstrates that evaluating transients with SU power distributions would yield the most limiting conditions. With SU being most limiting and the system model being more conservative than the core model, utilizing the system

model with the SU power distributions would provide the most limiting reactor transient results—this is the approach adopted for the results in chapter 5.

Table 14. An overview of the NNS results for the system model and the core model at various cycle states.

Safety Margin	Correlation	NNS		NNS Core				
		System	SU	BOC	Q2	MOC	Q4	EOC
<i>Minimum Values</i>								
CHFR	Mirshak	3.03	3.09	3.08	3.24	3.42	3.72	3.74
	Sudo-Kaminaga	3.22	3.28	3.26	3.41	3.59	3.90	3.92
OFIR	Saha-Zuber	7.17	7.22	7.25	7.71	8.20	9.17	9.31
	Costa	5.62	5.48	5.51	5.86	6.23	6.96	7.07
ONBR	Bergles-Rohsenow	1.96	2.15	2.23	2.31	2.42	2.39	2.38

Table 15. A companion to Table 14 that shows the axial locations of the hot of the minimum safety margins. Note that the location is Z_{hot} , which is relative to the axial centerline of the fueled zone in the core (negative being below the centerline, and positive above the centerline). All locations are in cm.

	Correlation	NNS		NNS Core				
		System	SU	BOC	Q2	MOC	Q4	EOC
<i>Z_{hot} (cm)</i>								
CHFR	Mirshak	-1	-13	-11	-7	-9	7	7
	Sudo-Kaminaga	-1	-13	-11	-7	-15	7	7
OFIR	Saha-Zuber	-11	-13	-11	-7	-15	-9	7
	Costa	-11	-13	-11	-7	-15	-9	7
ONBR	Bergles-Rohsenow	9	13	7	9	7	15	15

5. Accident Analyses

The transients are run using the nodalization adopted in the system model, with the trips, shutdowns, and accident scenarios discussed in subsection 3.2.6 and section 3.4. For each accident scenario, the transient evolution of the temperatures (T_{∞} , and for evaluating the safety criterion of not exceeding the blistering $T_{c,o}$, and $T_{c,i}$) are shown alongside the temporal evolution of the minimum CHFR, OFIR, and ONBR (i.e., mCHFR, mOFIR, and mONBR) to provide additional understanding of system responses. The minimum safety margins encountered throughout each accident are tabulated in the following sections.

5.1. Loss of Power Accident

The loss of power accident (LOPA) is modeled as explained in section 3.4. A summary of the minimum ONBR, OFIR, and CHF throughout the LOPA are shown in Table 16, and are compared to relevant NBSR values for a LOPA. According to the values in Table 16, NBSR maintains higher mCHF than NBSR when utilizing the Mirshak correlation and similar mCHF values when utilizing Sudo-Kaminaga. Using Saha-Zuber, the NNS yields higher mOFIR than NBSR, whereas the Costa correlation yields more limiting mOFIR values. Throughout the LOPA, the mONBR is maintained above unity, indicating that no transition to two-phase flow would be observed in this accident. Both the PSS and SSS yield similar safety margins, demonstrating that both shutdown systems are adequate for this accident and yield almost identical behaviors. The following subsections show a more detailed assessment of the results for each of the shutdown systems (PSS and SSS, as explained in subsection 3.2.6). Note that the minimum ONBR, OFIR, and CHF for the NNS are found in the hot channel, with the axial location indicated in Table 16.

Table 16. A summary of the minimum ONBR, OFIR, and CHF throughout the loss of power accident.

	Correlation	NNS (PSS)		NNS (SSS)		NBSR	NBSR LEU
		Value	Z_{hot} (cm)	Value	Z_{hot} (cm)	Value	Value
CHF	Mirshak	3.03	-1	3.03	-1	2.19	-
	Sudo-Kaminaga	2.70	-1	2.66	-1	2.67	2.75
OFIR	Saha-Zuber	7.17	9	7.17	9	2.97	3.03
	Costa	2.72	-11	2.28	-11	-	-
ONBR	Bergles-Rohsenow	1.34	19	1.32	19	-	-

5.1.1. PSS

Figure 14 shows the temporal evolution of the temperatures throughout a LOPA with the PSS applied for the hot channel and the hottest elevation represented by Z_{hot} cm from the axial centerline of the fuel. The hottest channel in this transient (with the PSS applied) is channel 63 in row 2, where the hottest temperature is reached at an elevation of 23 cm above the fuel core centerline. Note how the temperatures of both the coolant and the cladding all remain below the saturation temperature of the coolant, affirming that the flow does not experience phase transitions (i.e., single-phase flow is maintained). The temperatures peak at ~110 seconds after the initiation of the transient, which is the point when the flywheels stop. After this point, temperatures drop because the natural circulation starts up throughout the core, demonstrating the effectiveness of natural circulation for maintaining sufficient cooling in the core post shutdown.

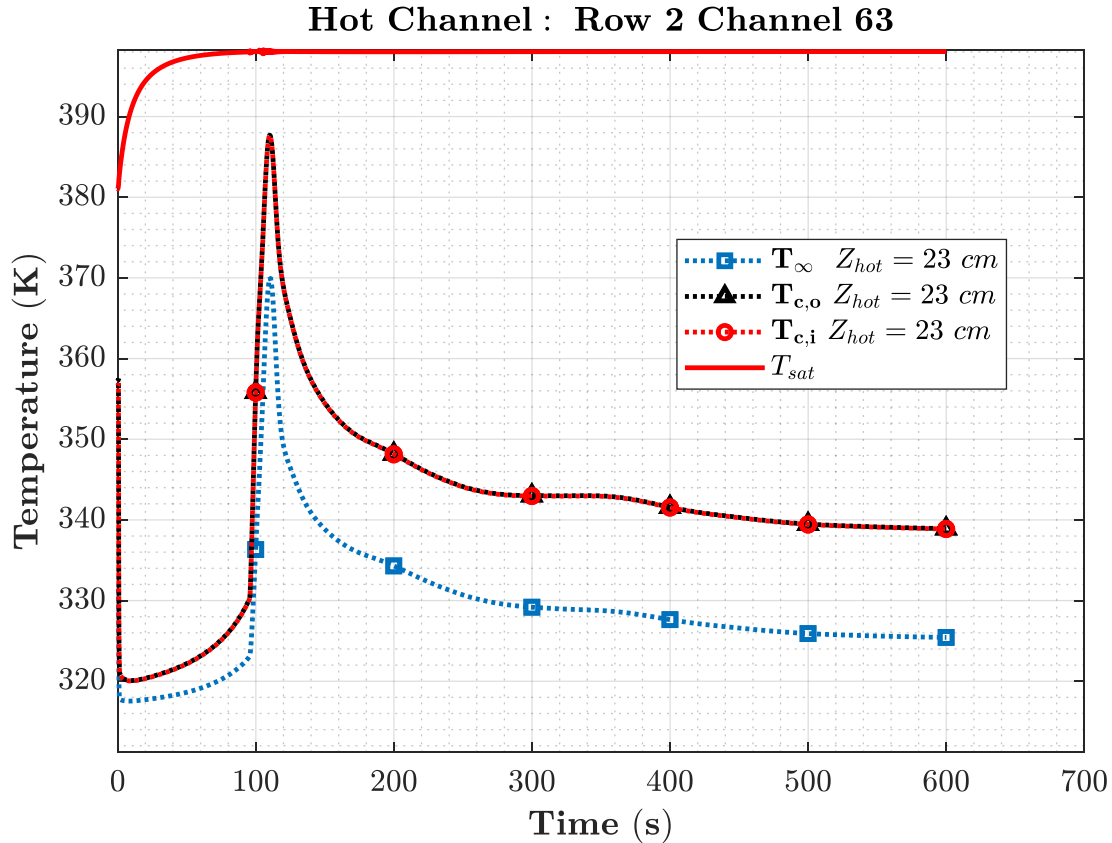


Figure 14. The temporal evolution of temperatures throughout a loss of power transient with the PSS applied.

At ~110 second point is when the lowest safety margins can be observed. For mCHFR, Figure 15 shows that at any point throughout the LOPA, the mCHFR (with either correlation) remains higher than two, which is the accepted mCHFR limit for research and test reactors in US for typical operating conditions [46]. Per Figure 15, the mCHFR increases at the start of the transient due to the core shutting down and going from 20 MW to decay heat while the forced convection flow continues due to the flywheels on the pumps. Approximately 40 seconds into the transient, the mCHFR reaches a maximum and then starts dropping due to the flywheels losing momentum. This drop in mCHFR appears to occur at a uniform rate, linearly for Sudo-Kaminaga and parabolically for Mirshak, until the ~100 second point, when the flywheels stop, and natural circulation becomes the primary cooling mechanism. Past that 100 second point, the rate at which the mCHFR drops becomes more dramatic for both correlations until they reach a minimum at the ~110 second point. At that point, natural circulation begins and the mCHFR starts rising. Per Figure 15, Sudo-Kaminaga is more limiting than Mirshak for a LOPA in the NNS. Further, Sudo-Kaminaga captures a more realistic evolution of the transient at the ~100 second point, whereas Mirshak predicts a sudden increase in the mCHFR once forced convection ends.

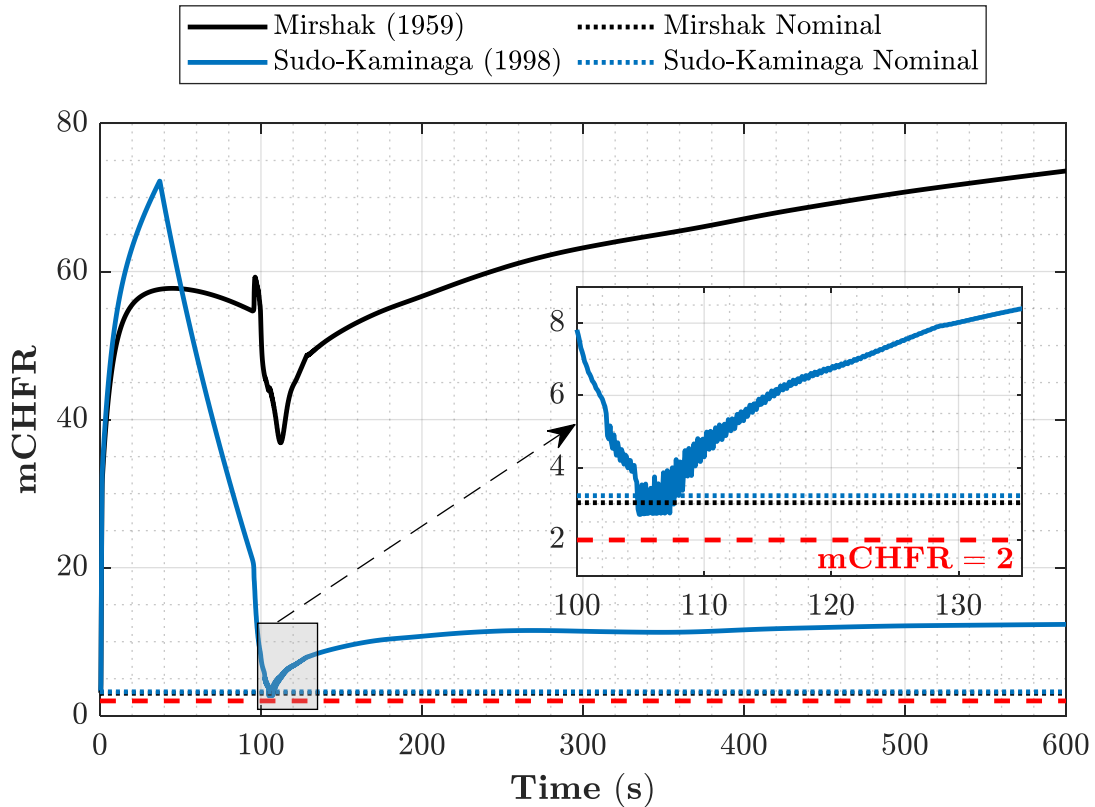


Figure 15. The temporal evolution of mCHFR throughout a loss of power transient with the PSS applied.

The mOFIR offers similar behavior to mCHFR as shown in Figure 16, where the Costa correlations appear to be more limiting than Saha-Zuber. Per the Costa correlation, the mOFIR drops to as low as 2.28, which still remains above two for mOFIR—we conclude this is a large enough margin. A fluctuating behavior is observable for both the mCHFR (with Sudo-Kaminaga) and for mOFIR (with Costa) in the period between the flywheel ramping-down and the start of natural circulation (between ~100-110 seconds). The fluctuations are likely caused by flow instability from the transition from forced to natural convection, which is observed in other relevant cases in literature [47].

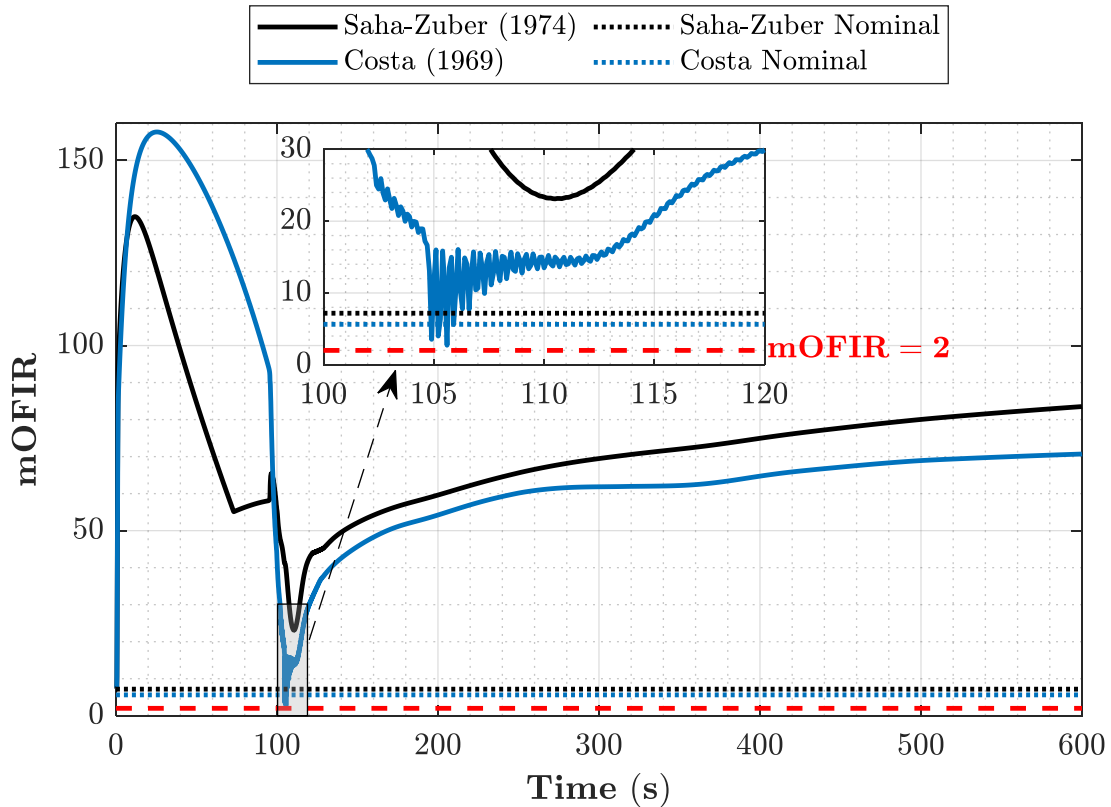


Figure 16. The temporal evolution of mOFIR throughout a loss of power transient with the PSS applied.

The mONBR's evolution throughout a LOPA is shown in Figure 17, where the minimum occurs at ~110 seconds. The same qualitative characteristics of mCHFR and mOFIR are retained for mONBR, demonstrating consistency in behavior across all the thermal-hydraulics safety margins. We expect this consistency for most accidents. Throughout a LOPA, the mONBR does not reach unity, indicating no expected transition to two-phase flow at any time throughout the accident. Note that for all computed safety margins, they do not dip below their nominal value until the forced-to-natural convection flow transition is observed within the ~100-110 seconds range. So, this period is likely the most limiting period of time for the LOPA. Note the lack of fluctuations in the safety margin (within this limiting period) is omitted from the mONBR plot. Another correlation to compute q''_{ONB} may yield this fluctuating behavior, but the Bergles-Rohsenow correlation used in this work did not detect any potential fluctuations in the mONBR in that limiting period during the LOPA. These demonstrate the NNS's capability to withstand a LOPA safely when using the PSS.

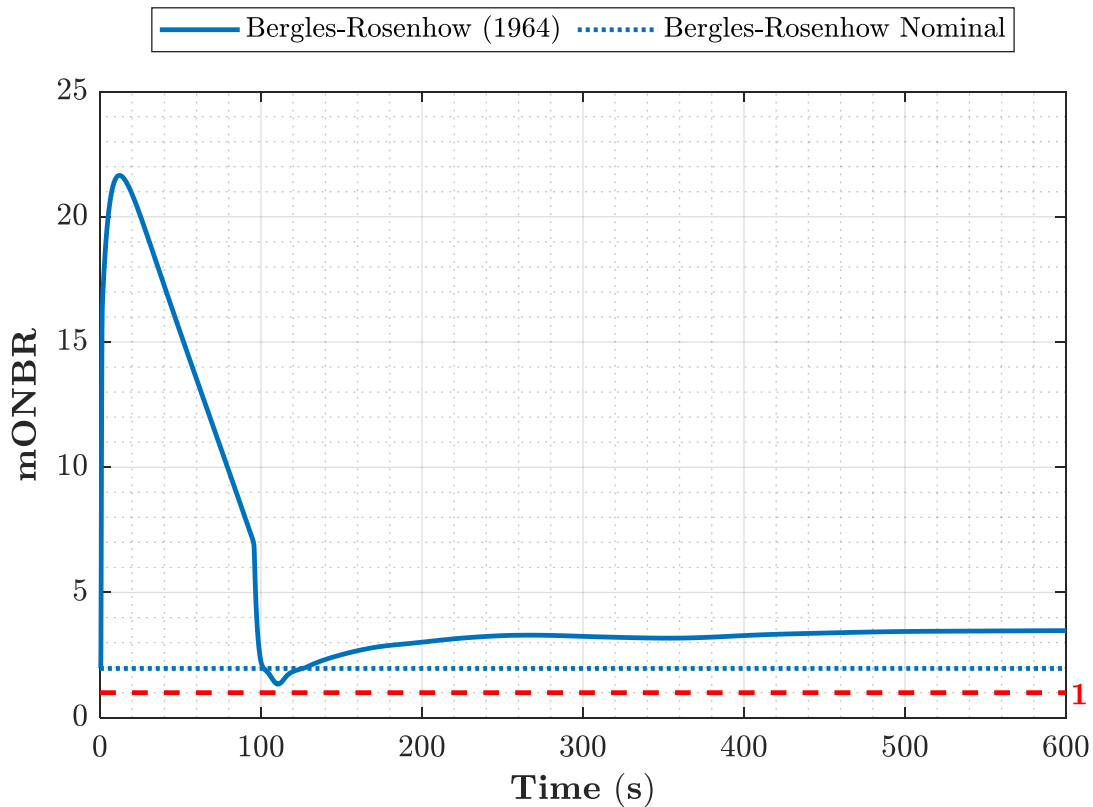


Figure 17. The temporal evolution of mONBR throughout a loss of power transient with the PSS applied.

5.1.2. SSS

Figure 18 shows the temporal evolution of the temperatures throughout a LOPA with the SSS applied for the hot channel and the hottest elevation represented by Z_{hot} cm from the axial centerline of the fuel. Similar to the PSS assessment in subsection 5.1.1, the hottest channel in this transient (with the SSS applied) is channel 63 in row 2, and the hottest temperature is reached at an elevation of 23 cm above the fuel core centerline. Note how the temperatures of both the coolant and the cladding remain below the saturation temperature of the coolant, affirming that the flow does not experience phase transitions (i.e., single-phase flow is maintained). The temperatures peak at ~110 seconds after the initiation of the transient, which is identical to the PSS behavior in Figure 14. After this point, the temperature drops due to natural circulation starting up throughout the core. This demonstrates the effectiveness of natural circulation for maintaining sufficient cooling in the core post shutdown.

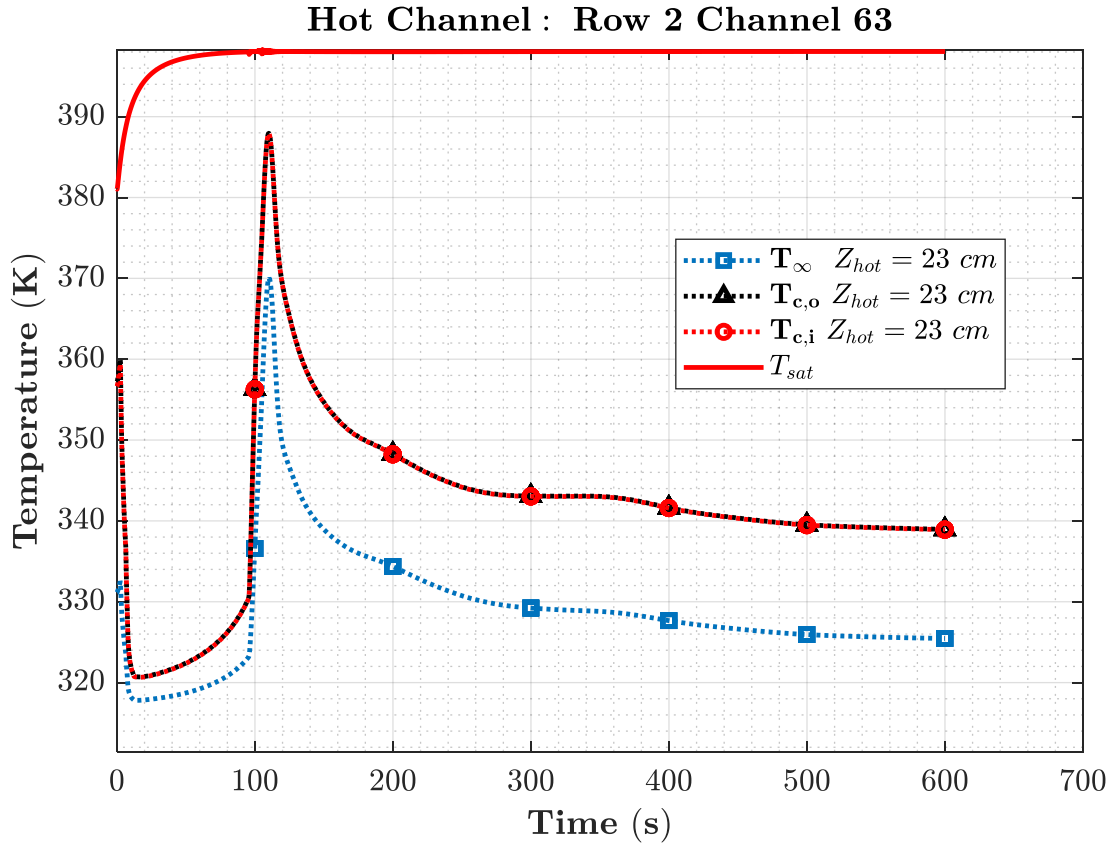


Figure 18. The temporal evolution of temperatures throughout a loss of power transient with the SSS applied.

The behavior of mCHFR with the SSS is similar to that of the LOPA with the PSS; Figure 19 shows the evolution of mCHFR throughout the LOPA with SSS, which is similar to the one shown in Figure 15 for the PSS. The most notable difference between PSS and SSS behaviors is the slight delay in the rise of mCHFR at the beginning of the LOPA. The PSS behavior in Figure 15 signaled a near instantaneous rise in the mCHFR, while the SSS behavior in Figure 19 has a visible offset when initiating the increasing slope; this is due to the delayed start of SSS compared to PSS. Even with the delay, the mCHFR does not reach two throughout the LOPA, indicating the SSS is effective in maintaining safety throughout the LOPA.

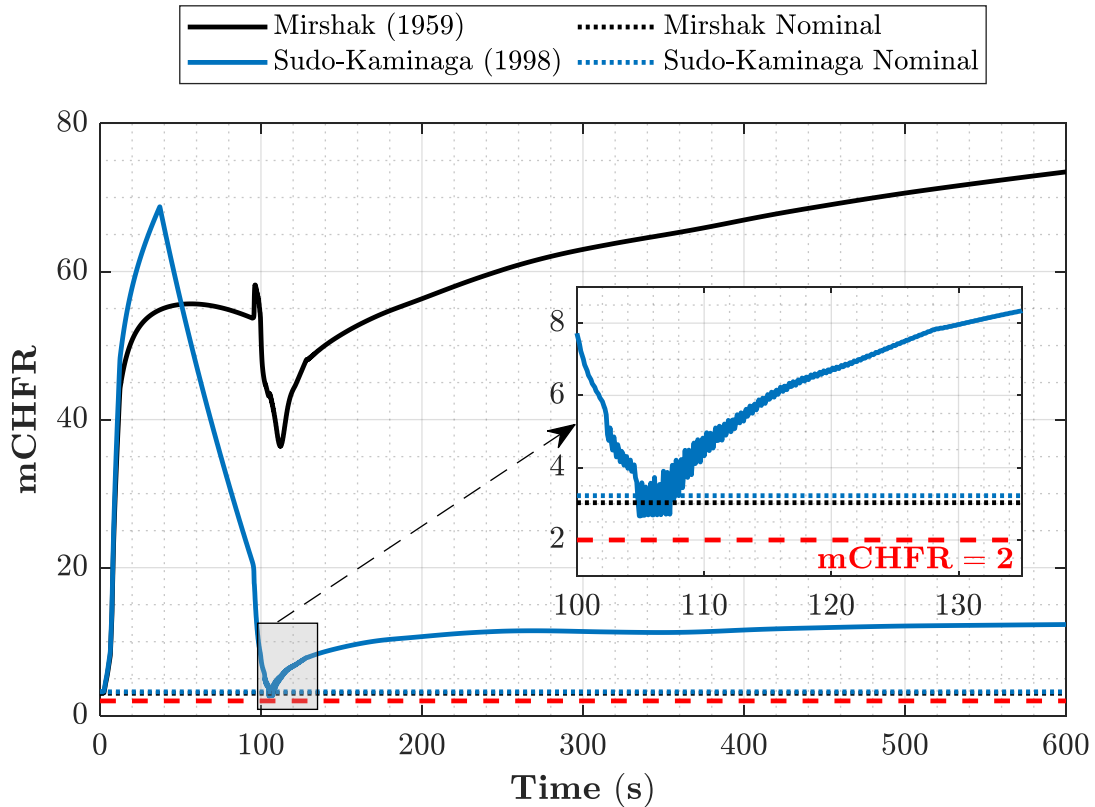


Figure 19. The temporal evolution of mCHFR throughout a loss of power transient with the SSS applied.

The mOFIR behavior in Figure 20 demonstrates a similar behavior to the one exhibited by the PSS in Figure 16. Maintaining cooling effectiveness appears to be less sensitive to the time it takes to shut down the core and more sensitive to the extended availability of forced convection offered by the flywheels and the natural convection offered by the water in the pool. Therefore, delays on the order of seconds will not cause significant changes to the NNS's response to a LOP. But reductions in the flywheels' momentum or pool level would yield significant changes to the NNS's response to a LOPA.

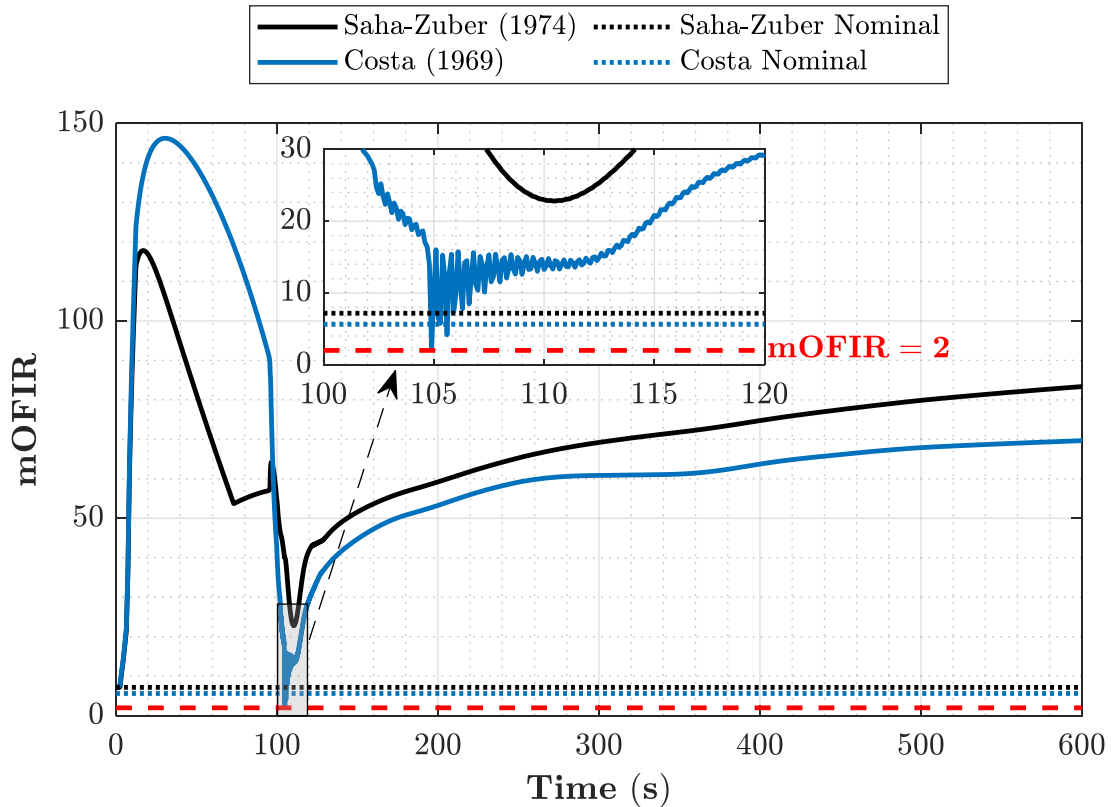


Figure 20. The temporal evolution of mOFIR throughout a loss of power transient with the SSS applied.

The analysis in Figure 20 are also reflected in the mONBR behavior shown in Figure 21. Whether PSS or SSS are applied, the behavior is sensitive to the extended availability of forced convection from the flywheels and the natural circulation from the pool. The delay caused by the SSS is not enough to cause any difference in the NNS's response to the LOPA. This sentiment is echoed by all the other accident scenarios we analyzed.

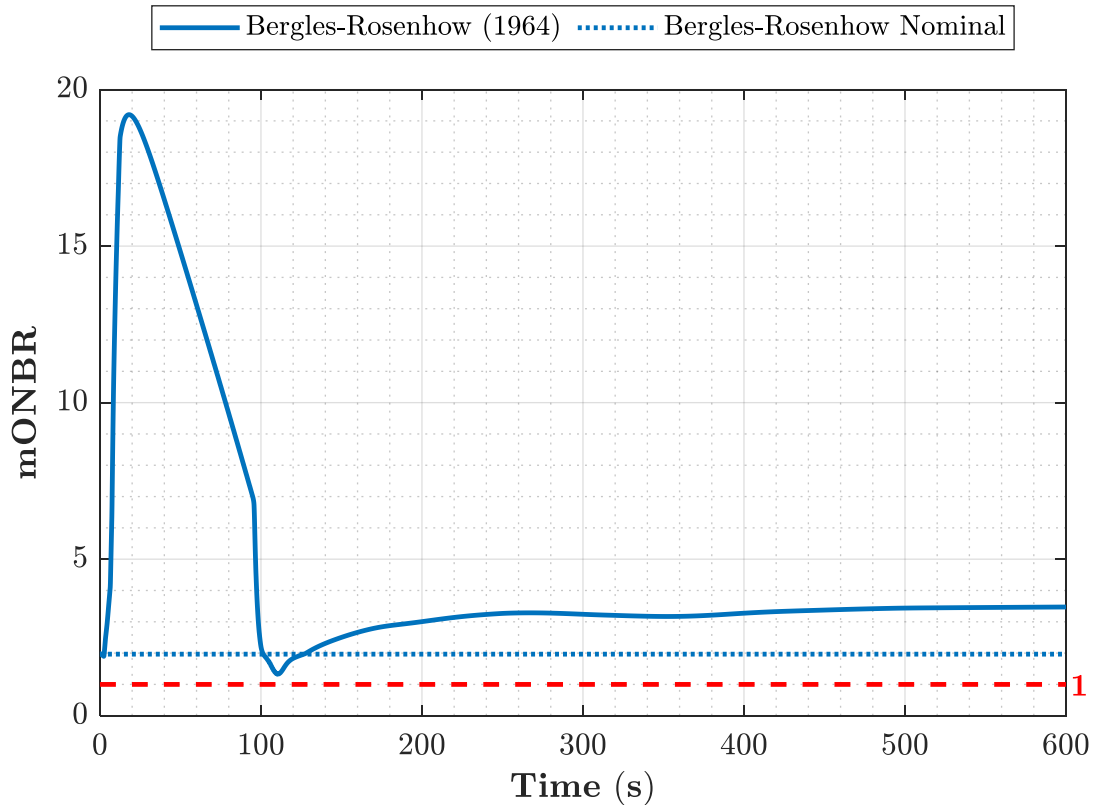


Figure 21. The temporal evolution of mONBR throughout a loss of power transient with the SSS applied.

5.2. Loss of Heat Sink Accident

The loss of heat sink accident (LOHSA) is modeled as explained in section 3.4. Table 17 shows a summary of the minimum-obtained safety margins throughout the LOHSA for both NNS shutdown systems. Note there were no comparable accidents for NBSR in either the SAR or the LEU conversion PSAR. Table 17 demonstrates that the Mirshak correlation is more limiting for mCHFR and the Costa correlation is more limiting for mOFIR. Both the CHFR and OFIR remain above two throughout the incident, demonstrating the effectiveness of both the PSS and SSS at shutting down the core during the LOHSA. Both shutdown systems are adequate for this accident and yield near identical behaviors. Therefore, this section provides a more detailed assessment of the LOHSA results for PSS, with the SSS results reported in Appendix B.1. For this accident, the shutdown systems are applied via an outlet temperature trip.

Table 17. A summary of the minimum safety margins throughout the loss of heat sink accident. The minimum margins are all found in the hot channel at the axial location Z_{hot} .

Safety Margin	Correlation	NNS (PSS)		NNS (SSS)	
		Value	Z_{hot} (cm)	Value	Z_{hot} (cm)
CHFR	Mirshak	2.81	-1	2.81	-1
	Sudo-Kaminaga	3.12	-1	3.12	-1
OFIR	Saha-Zuber	5.14	-11	5.13	-11
	Costa	4.04	-11	4.03	-11
ONBR	Bergles-Rohsenow	1.81	19	1.81	19

Figure 22 shows the temporal evolution of the temperatures throughout a LOHSA with the PSS applied for the hot channel and the hottest elevation represented by Z_{hot} cm from the axial centerline of the fuel. The hottest channel in this transient (with the PSS applied) is channel 63 in row 2 (like the LOPA), where the hottest coolant temperature is reached at an elevation of 23 cm above the fuel core centerline. The hottest cladding temperatures are reached at an elevation of 13 cm above the centerline. Considering both the coolant and cladding temperatures remain below the saturation temperature of the coolant, the flow does not experience phase transitions throughout the LOHSA (i.e., single-phase flow is maintained). Observe a drop in the temperatures at ~236 seconds after the start of the accident, which is when the RPS trip is activated, shutting down the reactor and reducing the heat generation in the core. Once the reactor is shut down with either PSS or SSS, the temperature drops and fluctuates at $332 \text{ K} \pm 3 \text{ K}$ until the end of the simulation.

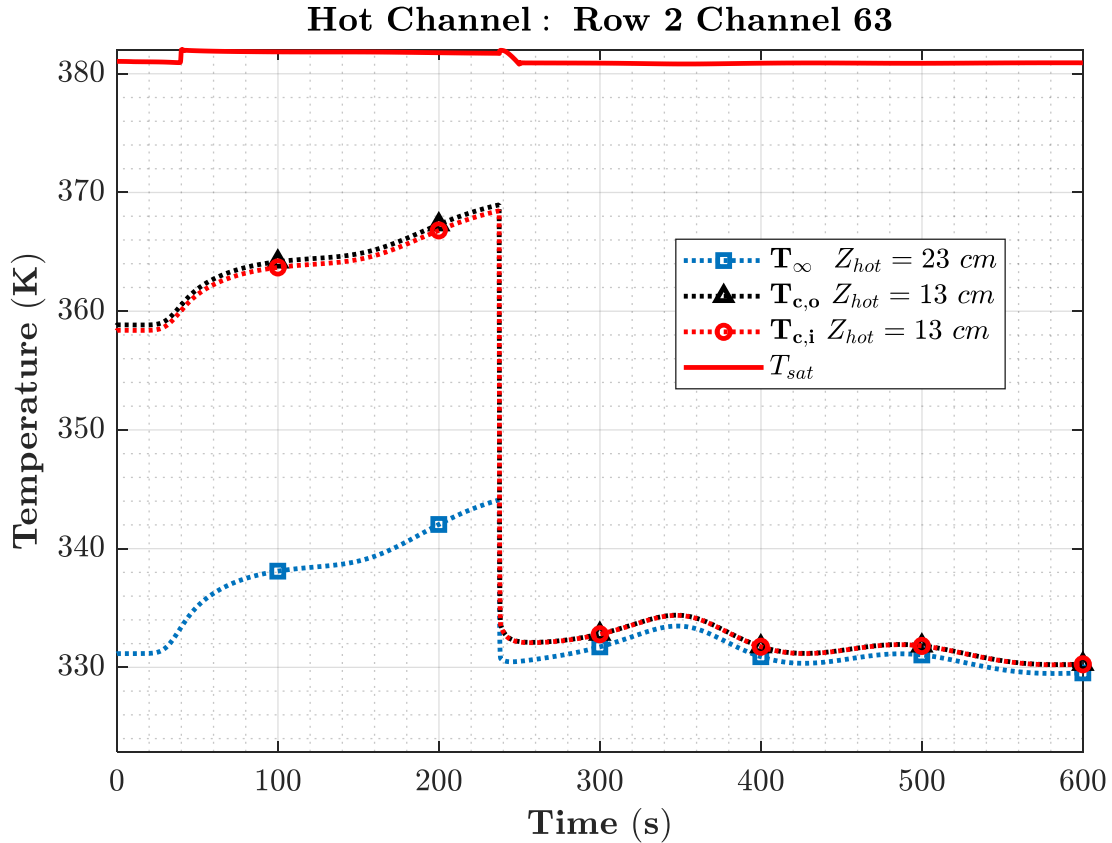


Figure 22. The temporal evolution of temperatures throughout a loss of heat sink transient with the PSS applied.

The mCHFR evolution throughout the LOHSA is shown in Figure 23. Note how both correlations are qualitatively consistent, with Mirshak providing more limiting mCHFR predictions. At the start of the LOHSA and prior to the RPS trips being initiated, the mCHFR drops slowly due to the increasing temperature shown in Figure 22. Once the RPS trip initiates, the mCHFR shoots back up due to the effective shutdown of the core, reducing the heat generation in the fuel. At all times throughout the LOHSA, the mCHFR is higher than two, ensuring the effectiveness of the NNS at withstanding the LOHSA.

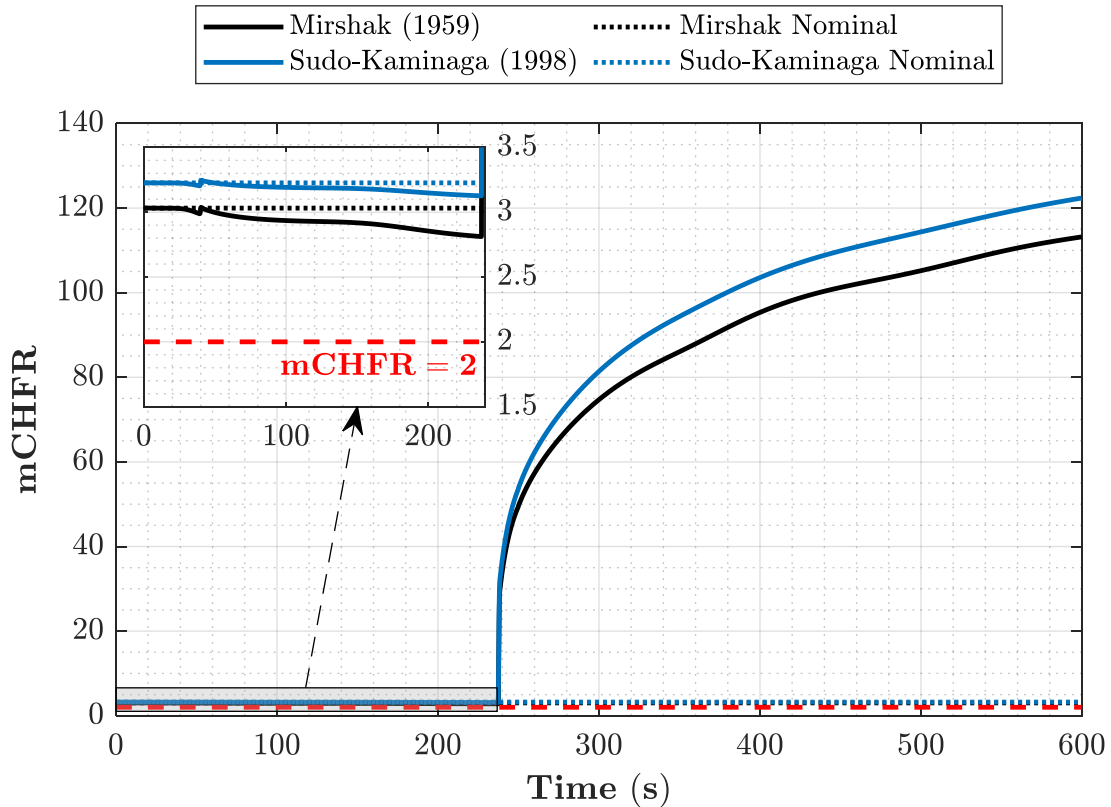


Figure 23. The temporal evolution of mCHFR throughout a loss of heat sink transient with the PSS applied.

Figure 24 shows the mOFIR temporal evolution is similar to the mCHFR, where the mOFIR drops until the ~236 seconds point when the reactor is shut down via the RPS trip, after which the mOFIR shoots up. The Costa correlation provides the more limiting estimate of mOFIR. But both correlations show near identical qualitative behavior and demonstrate that the mOFIR does not reach two throughout the LOHSA. For both the mCHFR and mOFIR, the PSS and SSS provide similar behaviors; the only exception is that the jump in the safety margins does not occur as fast as the PSS due to the delay in initiating the shutdown system. This does not yield any notable variations other than that slight delay. For the SSS results, refer to Appendix B.1.

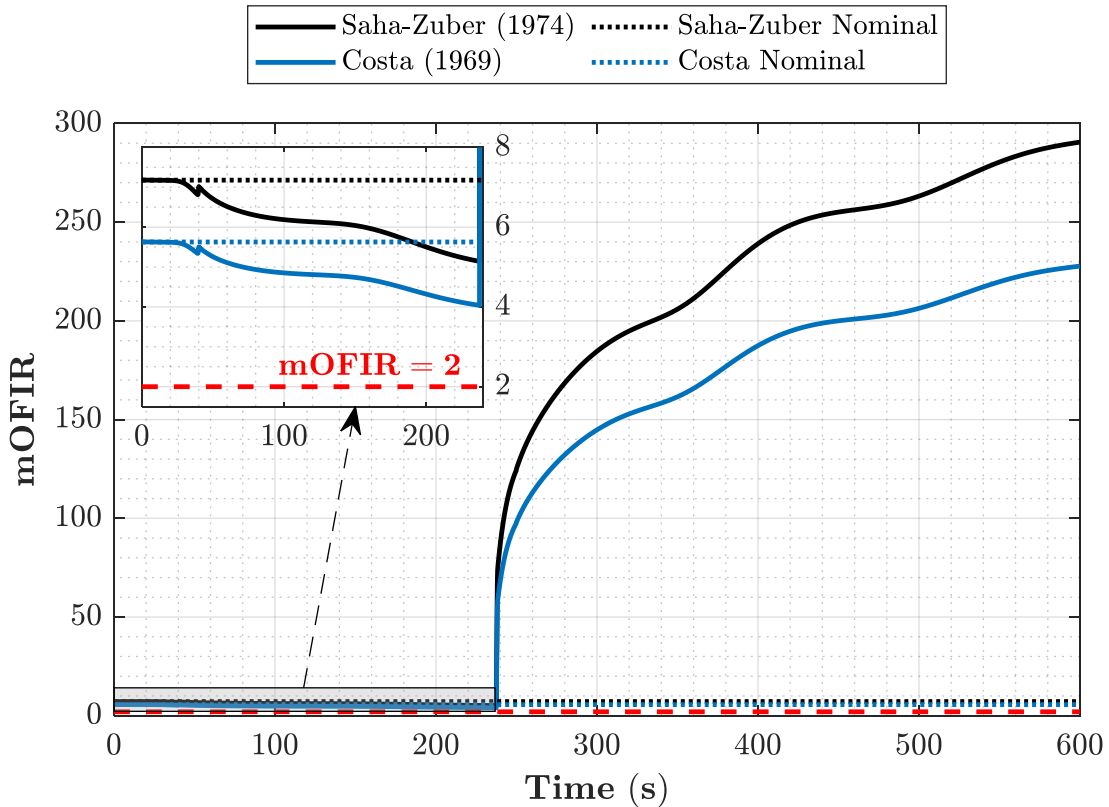


Figure 24. The temporal evolution of mOFIR throughout a loss of heat sink transient with the PSS applied.

The mONBR yields a similar qualitative behavior to the other two safety margins, where a drop occurs in the first portion of the LOHSA, and then it jumps as the PSS initiates at ~236 seconds once the RPS trips (Figure 25). At no time throughout the LOHSA does the mONBR drop to unity, ensuring that single-phase convection remains throughout the accident. Like the other accidents, both shutdown systems yield near identical results (SSS results are in Appendix B.1). This shows the effectiveness of both systems to shut down the core without any operator intervention in the LOHSA, demonstrating the selected RPS trips are sufficient to withstand the LOHSA. Further, even in the event of a LOHSA involving the loss of the secondary system, the NNS can shut down with either shutdown system if the RPS trips work, thereby reducing the safety significance of the secondary system and loosening quality assurance requirements. Note that any change in the NNS design, RPS setpoints and logic, or the shutdown systems would require a reevaluation of the LOHSA (and other accidents), which may change the safety significance of the secondary system.

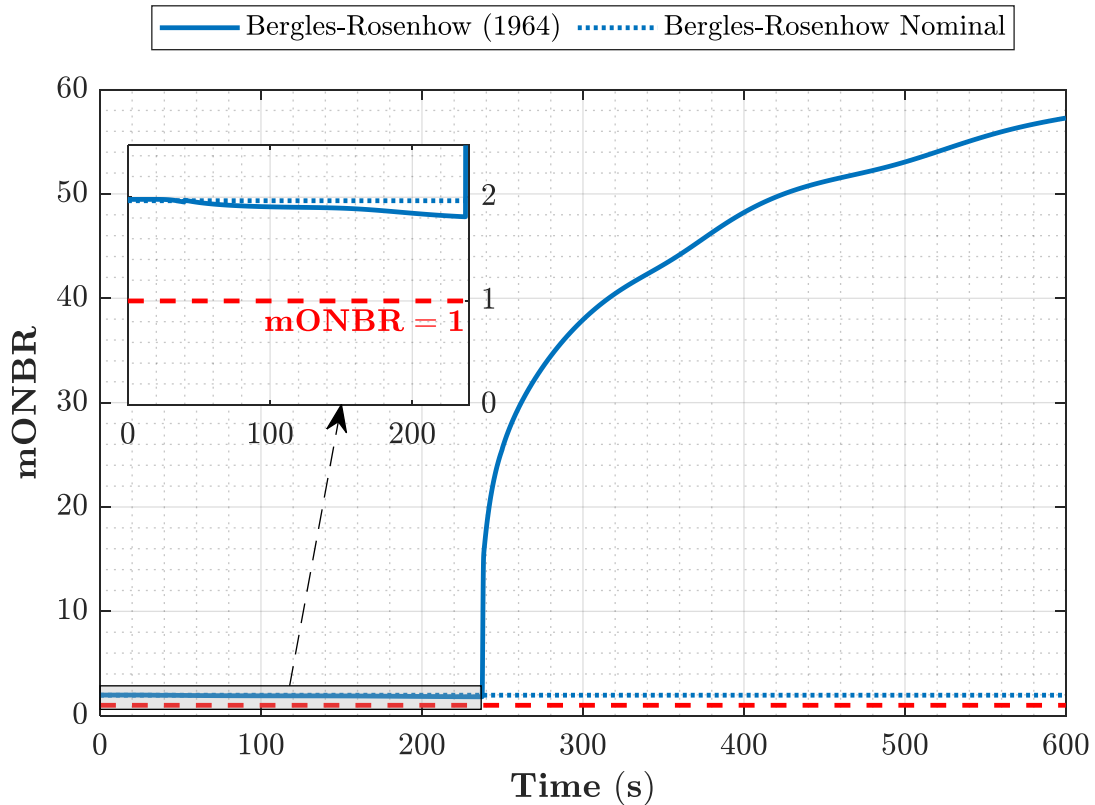


Figure 25. The temporal evolution of mONBR throughout a loss of heat sink transient with the PSS applied.

5.3. Reactivity Insertion Accidents

The reactivity insertion accident (RIA) is modeled as explained in section 3.4. Table 18 shows a summary of the minimum-obtained safety margins throughout the LOHSA for both NNS shutdown systems with comparisons to the NBSR and the LEU-fueled NBSR core. Table 18 demonstrates that the Mirshak correlation is more limiting for mCHFR, and the Costa correlation is more limiting for mOFIR, which is consistent with the LOHSA findings in Table 17. Both the CHFR and OFIR remain above two throughout the incident, demonstrating the effectiveness of both the PSS and SSS at shutting down the core during the RIA. Both shutdown systems are adequate for this accident and yield near identical behaviors. So, this section provides a more detailed assessment of the RIA results for PSS, with the SSS results reported in Appendix B.2. For this accident, the shutdown systems are applied via a reactor power trip.

Table 18. A summary of the minimum safety margins throughout the reactivity insertion accident. The minimum margins are all found in the hot channel at the axial location Z_{hot} .

Safety Margin	Correlation	NNS (PSS)		NNS (SSS)		NBSR	NBSR LEU
		Value	Z_{hot} (cm)	Value	Z_{hot} (cm)	Value	Value
CHFR	Mirshak	2.17	-1	2.17	-1	1.19	-
	Sudo-Kaminaga	2.36	-11	2.36	-11	2.26	2.21
OFIR	Saha-Zuber	4.61	-11	4.61	-11	3.19	3.26
	Costa	3.62	-11	3.62	-11	-	-
ONBR	Bergles-Rohsenow	1.49	9	1.49	9	-	-

Figure 26 shows the temporal evolution of the temperatures throughout an RIA with the PSS applied for the hot channel and the hottest elevation represented by Z_{hot} cm from the axial centerline of the fuel. The hottest channel in this transient (with the PSS applied) is channel 63 in row 2 (like the LOPA and LOHSA), where the hottest coolant temperature is reached at an elevation of 23 cm above the fuel core centerline. The hottest cladding temperatures are reached at an elevation of 13 cm above the centerline. Considering both the coolant and cladding temperatures remain below the saturation temperature of the coolant, the flow does not experience phase transitions throughout the RIA (i.e., single-phase flow is maintained). The sharp rise in temperatures at the beginning of the RIA is due to the inadvertent withdrawal of all the control blades. The temperatures drop ~3.1 seconds after the start of the RIA, due to the RPS trips being reached, shutting down the reactor. Note that flow from all pumps is maintained throughout this accident, allowing for the cooling to be maintained even after the PSS or SSS are applied.

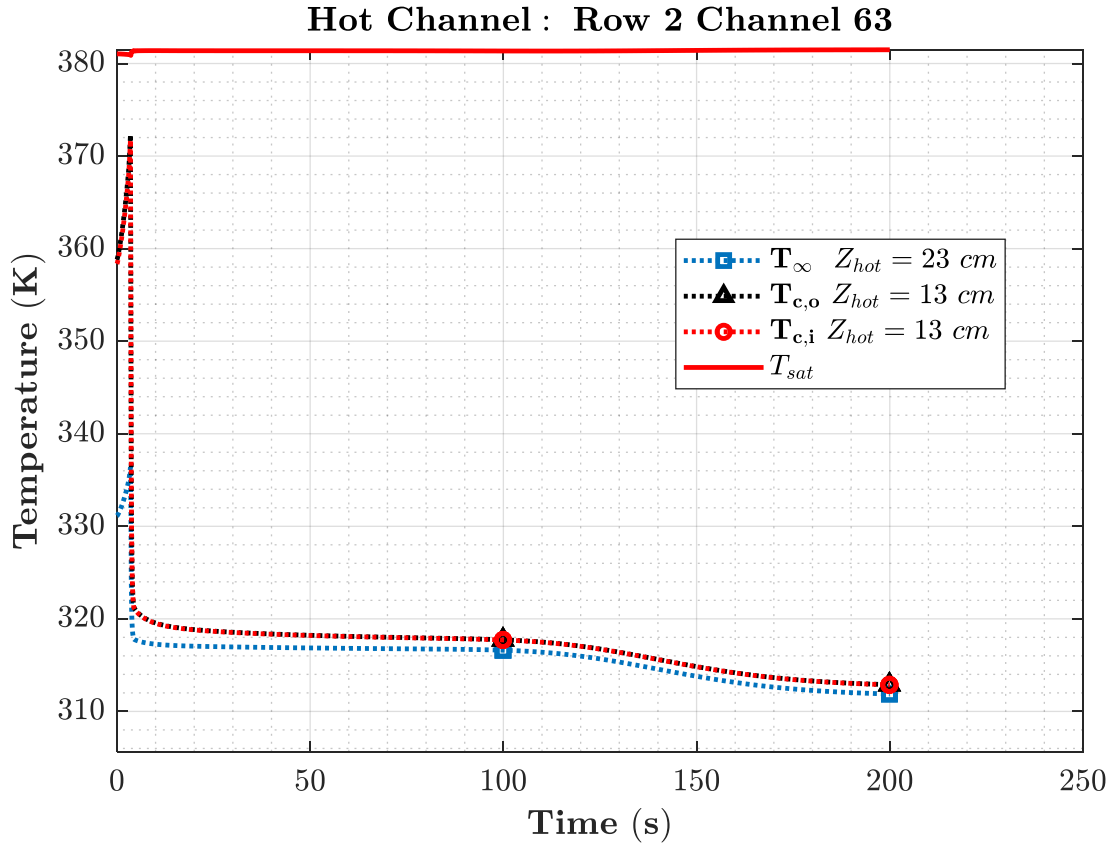


Figure 26. The temporal evolution of temperatures throughout a reactivity insertion transient with the PSS applied.

The mCHFR behavior throughout the RIA is illustrated in Figure 27, where the mCHFR drops at the start of the accident, then increases after ~ 3.1 seconds due to the reactor shutting down. The primary difference between the PSS and SSS for the RIA is the sharp increase in mCHFR (and decrease in temperatures) is delayed by two seconds due to the time it takes for the SSS to initiate. The zoomed-in sub-axis in Figure 58 (Appendix B.2) shows the difference between the two shutdown systems in the RIA, where the mCHFR requires two seconds before the increase in the safety margin is observed. Though both SSS and PSS demonstrate that the mCHFR does not drop below two throughout the RIA (with any of the two correlations used for computing the safety margin). Both Sudo-Kaminaga and Mirshak yield identical qualitative results for mCHFR in an RIA; Mirshak is more limiting at the start of the accident.

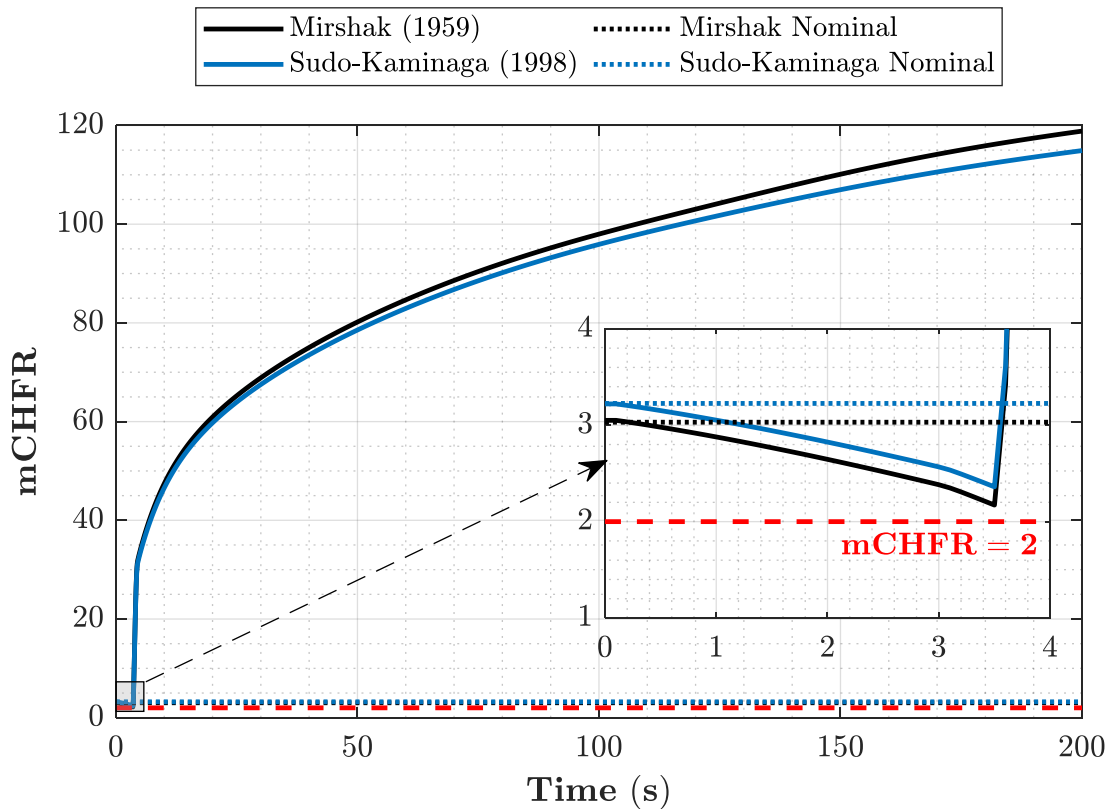


Figure 27. The temporal evolution of mCHFR throughout a reactivity insertion transient with the PSS getting used.

The mOFIR and mCHFR behaviors are identical qualitatively, as demonstrated in Figure 28. The Costa correlation offers the more limiting estimate of mOFIR throughout the RIA with either of the shutdown systems (see Appendix B.2 for SSS results). For both mCHFR and mOFIR, the sharp increase lasts a second after the PSS starts up. Afterward, the increase is more gradual, following a logarithmic growth profile. When the SSS is applied, the sharp increase in the safety margins are more gradual (Appendix B.2), where the SSS allows for an exponential growth in the margins, then follows a logarithmic growth like the PSS offers. Regardless, the mOFIR remains larger than two throughout the RIA in the NNS.

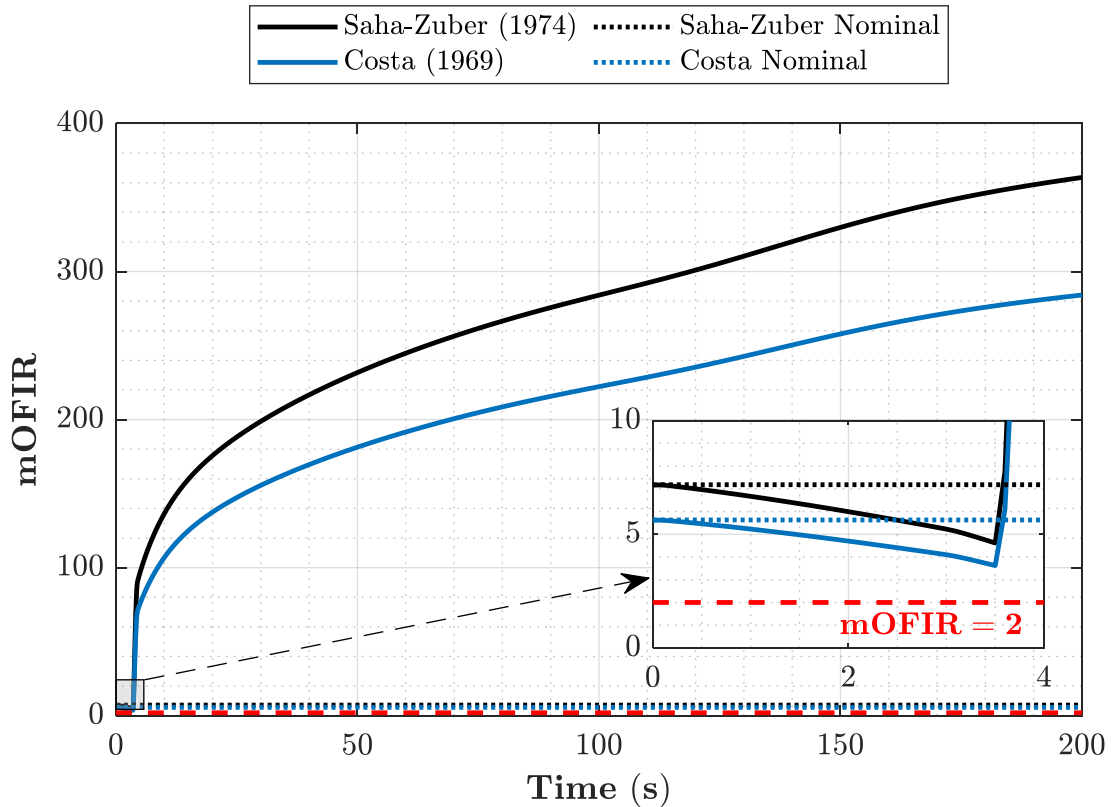


Figure 28. The temporal evolution of mOFIR throughout a reactivity insertion transient with the PSS applied.

The mONBR behavior (Figure 29) follows a similar trend to mCHFR and mOFIR. For both the PSS and SSS, the mONBR remains above unity, indicating that single-phase convection is maintained throughout the RIA. The delay offered by the SSS activation does not yield any detrimental effects to the NNS's ability to recover from the RIA. As the blades are withdrawn (prior to the core shutdown), the temperature rises as shown in Figure 26, which would remove some reactivity. Additional analyses would be needed to further assess the effects of the moderator temperature reactivity feedback on the RIA.

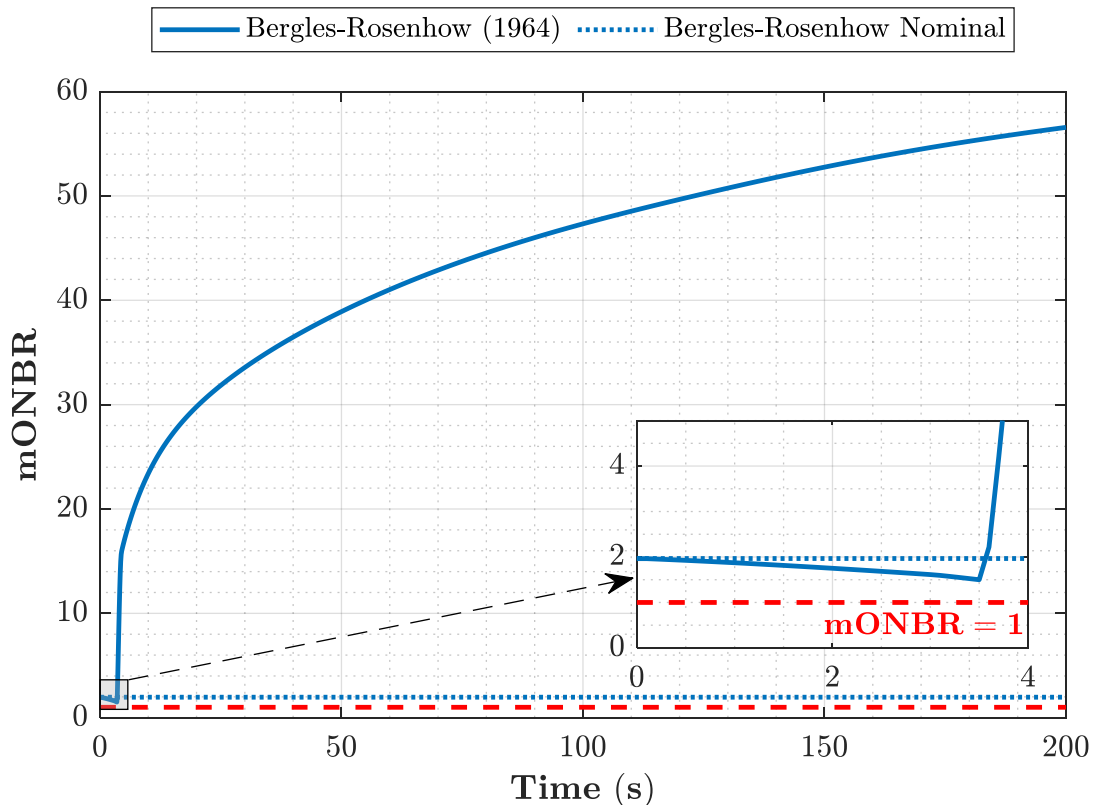


Figure 29. The temporal evolution of mONBR throughout a reactivity insertion transient with the PSS applied.

5.4. Loss of Flow Accidents

Two loss of flow accidents (LOFAs) are analyzed as explained in section 3.4: the NNS’s response to a seizure of one primary pump (LOFA₁) or a complete loss of two primary pumps (LOFA₂). This section provides results of both LOFAs utilizing the PSS (SSS results for the LOFAs are in Appendix B.3). For both LOFAs, the shutdown systems are applied via the pressure drop trip. Both LOFAs start at a time of 1 second, with the LOFA₁ tripping at 1.3 seconds (0.3 seconds after the LOFA starts) while the LOFA₂ trips at 3.3 seconds (2.3 seconds after the LOFA starts).

5.4.1. Seizure of One Pump

The seizure of one pump LOFA (LOFA₁) is simulated with the TRACE model—assuming an abrupt shaft seizure in one of the primary pumps, causing a flow through this pump to stop. Table 19 shows a summary of the minimum obtained safety margins throughout the LOFA₁ for both NNS shutdown systems with comparisons to the NBSR and the LEU-fueled NBSR core. Similar to the accidents discussed, Table 19 demonstrates that the Mirshak correlation is more limiting for mCHFR, and the Costa correlation is more limiting for mOFIR. Both the CHFR and OFIR remain above two throughout the incident, demonstrating the effectiveness of both the PSS and SSS at shutting down the core during the LOFA₁. Both shutdown systems are adequate for this accident; provide safety margins above the desired limit; and yield near identical behaviors (apart from the

anticipated delay offered by the SSS). The two-second delay by the SSS causes no detrimental effects. So, this subsection provides a detailed assessment of the LOFA₁ results for PSS (SSS results are in Appendix B.3.1).

Table 19. A summary of the minimum safety margins throughout a seizure of one pump LOFA. The minimum margins are all found in the hot channel at the axial location Z_{hot} .

Safety Margin	Correlation	NNS (PSS)		NNS (SSS)		NBSR	NBSR LEU
		Value	Z_{hot} (cm)	Value	Z_{hot} (cm)	Value	Value
CHF _R	Mirshak	2.98	-1	2.75	-11	2.23	-
	Sudo-Kaminaga	3.21	-11	3.04	-11	3.02	3.11
OFIR	Saha-Zuber	6.48	-11	5.72	-11	3.39	3.46
	Costa	5.58	-11	5.18	-11	-	-
ONBR	Bergles-Rohsenow	1.68	9	1.48	9	-	-

Figure 30 shows the temporal evolution of the temperatures throughout a LOFA₁ with the PSS applied for the hot channel and the hottest elevation represented by Z_{hot} cm from the axial centerline of the fuel. The hottest channel in this transient (with the PSS applied) is channel 63 in row 2 (like the accidents discussed), where the hottest coolant temperature is reached at an elevation of 23 cm above the fuel core centerline. The hottest cladding temperatures are reached at an elevation of 13 cm above the centerline. Considering both the coolant and cladding temperatures remain below the saturation temperature of the coolant, the flow does not experience any phase transitions throughout the LOFA₁ (i.e., single-phase flow is maintained).

Although the gap between the saturation temperature and cladding temperature in Figure 30 is narrower than the one observed for the LOPA, the LOHSA, and the RIA, it still provides a margin of 13.6 K between them; this is 6.6 K higher than the difference between the maximum anticipated T_{∞} at steady-state conditions (Table 11) and the setpoint for the outlet coolant temperature (Table 4). Note the cladding temperature is higher than the coolant temperature, which peaks at 335.5 K ~1.7 seconds into the LOFA₁, which is ~0.4 seconds after the PSS is activated. The SSS activates two seconds after the PSS (i.e., at ~2.4 seconds into the LOFA₁), and the coolant temperature peaks at 338.5 K.

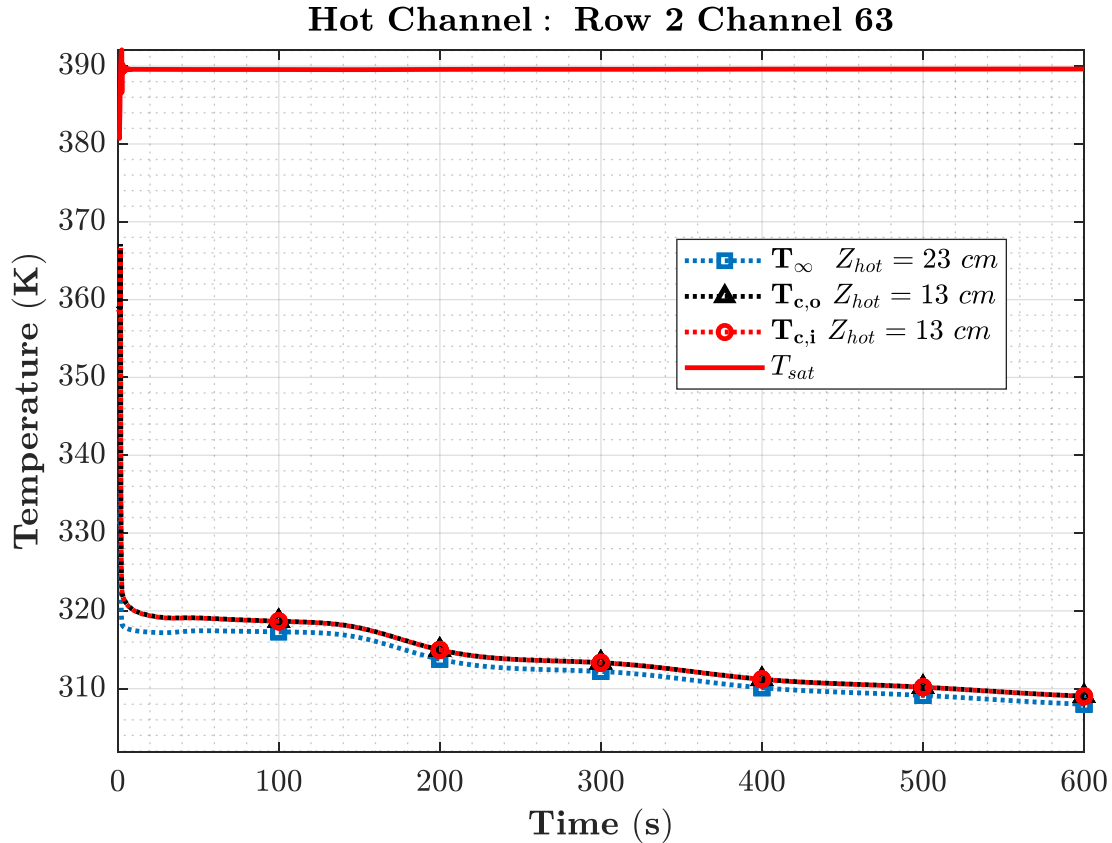


Figure 30. The temporal evolution of temperatures throughout a seizure of one pump LOFA transient with the PSS applied.

The mCHFR behavior throughout the LOFA₁ is shown in Figure 31, where the mCHFR remains relatively constant at its nominal value, and then increases once the PSS is applied. The primary difference between PSS and SSS for the LOFA₁ is that the sharp increase in mCHFR is delayed by two seconds due to the time it takes for the SSS to initiate. The zoomed-in sub-axis in Figure 62 (Appendix B.3.1) shows the difference between the two shutdown systems in the LOFA₁, where the mCHFR requires two seconds before the increase in the safety margin is observed. Within these two seconds, the mCHFR tends to oscillate around its nominal value, due to the preservation of some forced convection in the core. Regardless, both the SSS and PSS demonstrate that the mCHFR does not drop below two throughout the LOFA₁ (with any of the two correlations computing the safety margin). Both Sudo-Kaminaga and Mirshak yield qualitatively identical results for mCHFR in the LOFA₁; Mirshak is more limiting at the start of the accident.

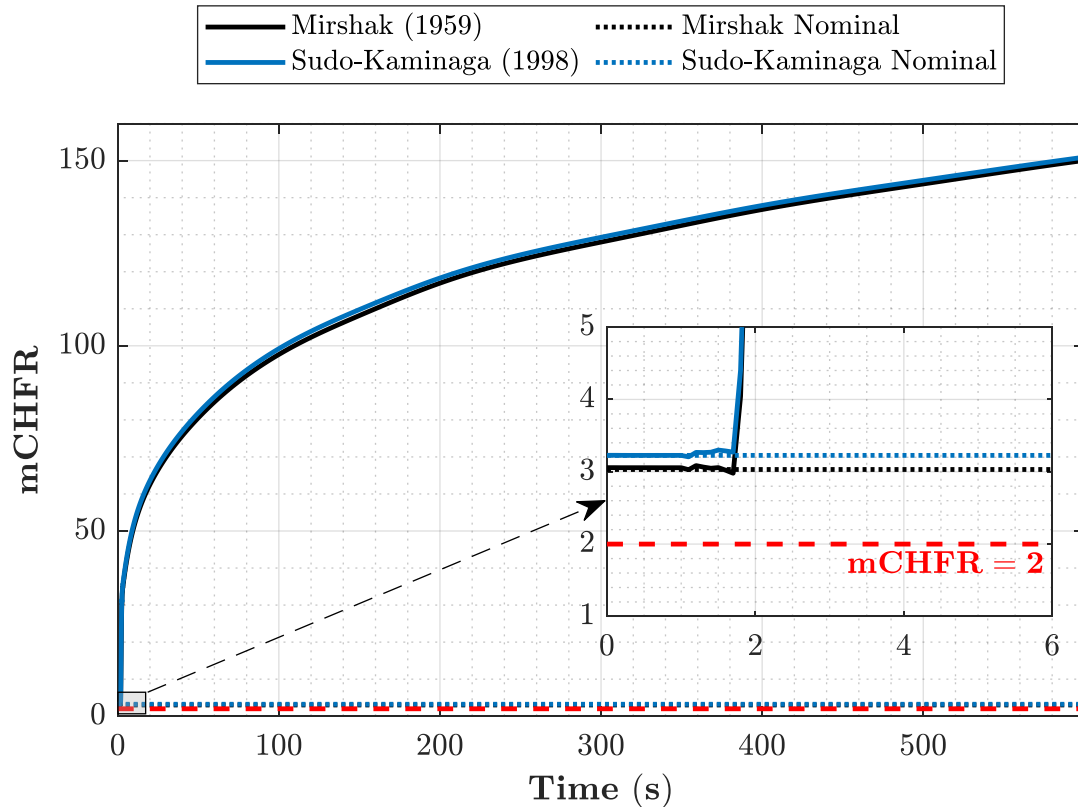


Figure 31. The temporal evolution of mCHFR throughout a seizure of one pump LOFA transient with the PSS applied.

The mOFIR behavior is qualitatively identical to that of mCHFR, as shown in Figure 32, where the Saha-Zuber correlation yields a more notable drop at the start in mOFIR at the start of the accident and before the scram is initiated. The Costa correlation offers the more limiting estimate of mOFIR throughout the LOFA₁ with either of the shutdown systems (see Appendix B.3.1 for SSS results). Note for both mCHFR and mOFIR, the sharp increase lasts a second after the PSS starts up. Afterward, the increase becomes more gradual, following a logarithmic growth profile. When the SSS is applied, the increase in the safety margins are more gradual (Appendix B.3.1) and similar to the growth seen for the RIA. Regardless, the mOFIR remains larger than two throughout the LOFA₁ in the NNS.

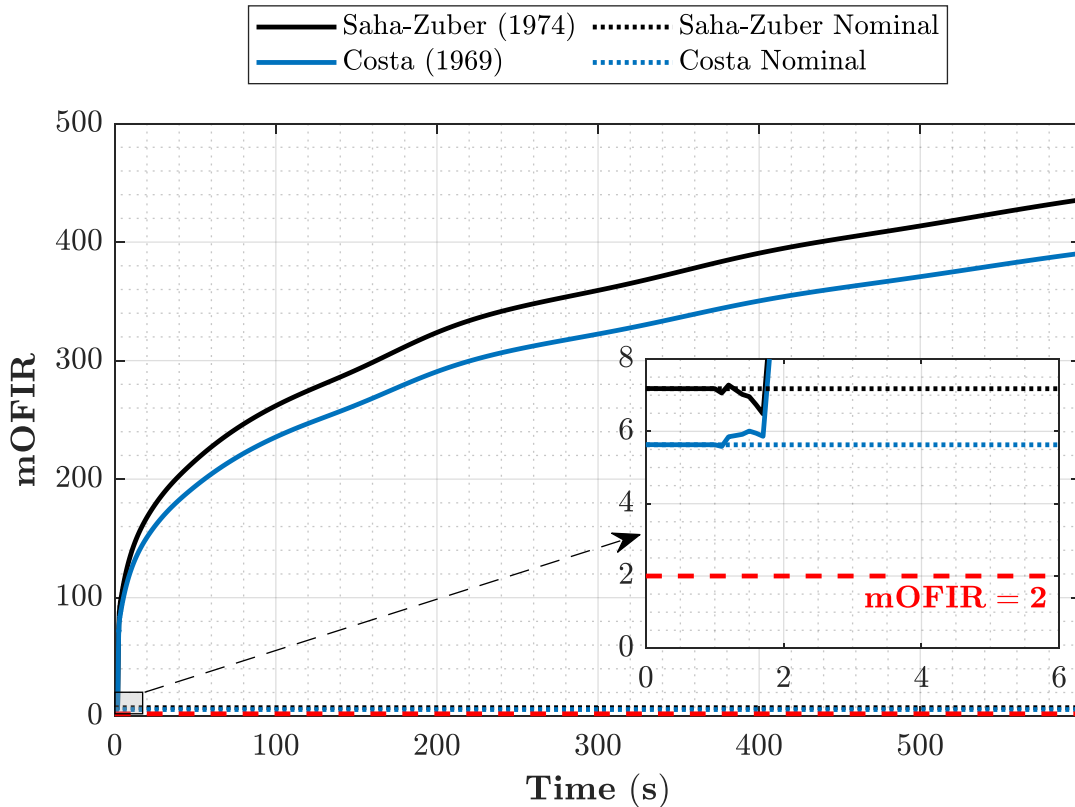


Figure 32. The temporal evolution of mOFIR throughout a seizure of one pump LOFA transient with the PSS applied.

The mONBR behavior (Figure 33) follows a similar trend to the ones observed for mCHFR and mOFIR. For both the PSS and SSS, the mONBR remains above unity, indicating that single-phase convection is maintained throughout the LOFA₁. The delay from the SSS activation does not yield any detrimental effects to the NNS’s ability to recover from the LOFA₁. Although both PSS and SSS can recover and secure the core during the LOFA₁, there are differences in the early stages due to the two-second delay in the SSS’s activation. The SSS clad temperature profiles in Appendix B.3.1 reflect a 5 K drop in their values at ~2.3 seconds. After that point, the temperature remains almost unchanged until the SSS activates at ~3.3 seconds, shutting down and reducing heat generation in the core. This initial 5 K drop is due to flow rate in the channel ramping up from the pressure-induced flow rate compensation offered by the remaining two active pumps.

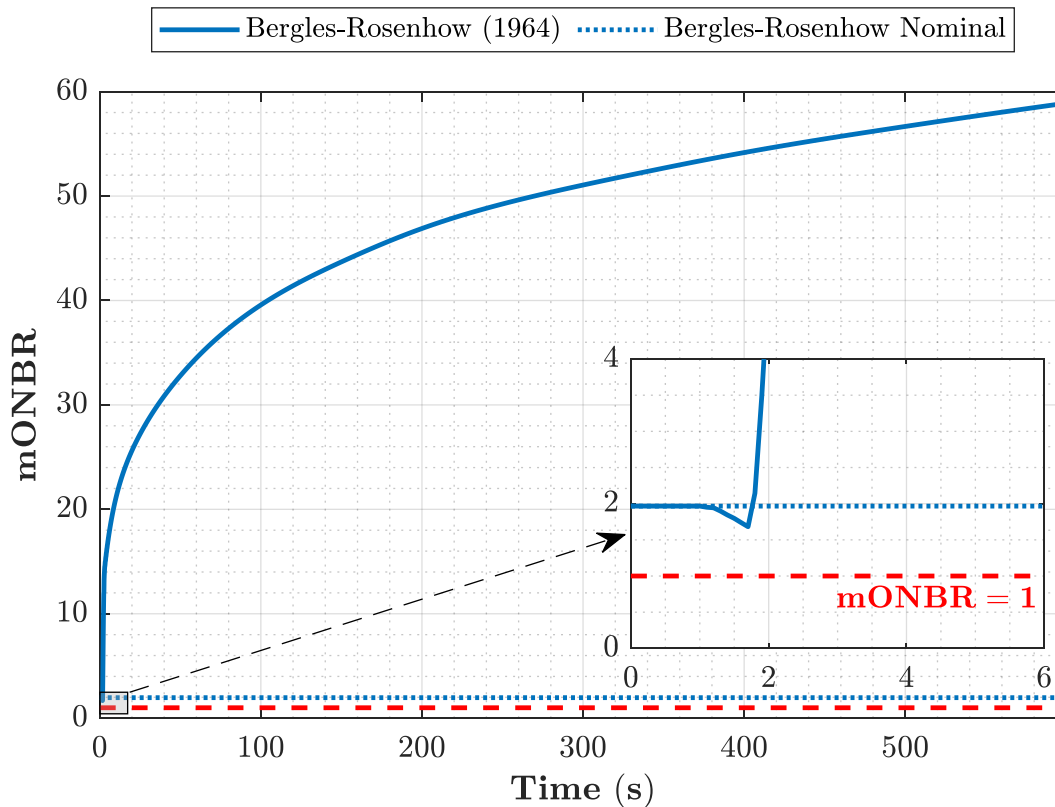


Figure 33. The temporal evolution of mONBR throughout a seizure of one pump LOFA transient with the PSS applied.

5.4.2. Loss of Two Pumps

The loss of two pumps LOFA (LOFA₂) is simulated with the TRACE model assuming the motors for two separate primary pumps failed at the same time, and the pumps coast down with assistance from the flywheels. Table 19 shows a summary of the minimum obtained safety margins throughout the LOFA₂ for both NNS shutdown systems. The NBSR does not offer any relevant comparisons to this accident. This is because the NRC’s design acceptance criteria for non-power reactors (according to the NUREG-1537) requires “*design redundancy to protect against unsafe conditions in case of single failures of reactor protective and safety systems.*” Such “*single failure*” condition is exceeded in the LOFA₂ as it assumes multiple and simultaneous failures to reactor safety systems. This “*single failure*” condition is exceeded by the SSS since applying the SSS requires both an accident scenario (applied by a failure of a safety or protective system) and the failure of the PSS. So, the NNS’s incorporation of the SSS exceeds current NRC guidance and requirements for the design of non-power reactors. Accounting for this LOFA₂ accident goes beyond NRC guidance and offers improved safety than what the current guidelines require.

Like the accidents discussed, Table 20 demonstrates the Mirshak correlation is more limiting for mCHFR, and the Costa correlation is more limiting for mOFIR. Both the CHFR and OFIR remain above two throughout the incident, and the mONBR remains above unity. This demonstrates the effectiveness of both the PSS and SSS at shutting down the core during the LOFA₂. Both shutdown

systems are adequate for this accident (provide safety margins above the desired limit) and yield near identical behaviors (apart from the anticipated delay from the SSS). The two-second delay from the SSS causes no detrimental effects. So, this subsection provide detailed assessments of the LOFA₂ results for PSS (SSS results are in Appendix B.3.2).

Table 20. A summary of the minimum safety margins throughout a loss of two pumps LOFA. The minimum margins are all found in the hot channel at the axial location Z_{hot} .

Safety Criterion	Correlation	NNS (PSS)		NNS (SSS)	
		Value	Z_{hot} (cm)	Value	Z_{hot} (cm)
CHFR	Mirshak	3.03	-1	3.03	-1
	Sudo-Kaminaga	3.23	-1	3.23	-1
OFIR	Saha-Zuber	7.18	-11	7.13	-11
	Costa	5.63	-11	5.63	-11
ONBR	Bergles-Rohsenow	1.89	9	1.82	9

Figure 34 shows the temporal evolution of the temperatures throughout a LOFA₂ with the PSS applied for the hot channel and the hottest elevation represented by Z_{hot} cm from the axial centerline of the fuel. The hottest channel in this transient (with the PSS applied) is channel 63 in row 2 (like the accidents discussed), where the hottest coolant temperature is reached at an elevation of 23 cm above the fuel core centerline. The hottest cladding temperatures are reached at an elevation of 13 cm above the centerline. Considering both the coolant and cladding temperatures remain below the saturation temperature of the coolant, the flow does not experience any phase transitions throughout the LOFA₂ (i.e., single-phase flow is maintained).

As opposed to the LOFA₁, the RPS for the LOFA₂ takes longer, requiring ~3.7 seconds for the PSS to commence the shutdown (~5.7 seconds for SSS). This allows the coolant temperature to rise higher than the LOFA₁, but remains below the saturation temperature. The cladding temperatures in the LOFA₂ peak at ~361 K with the PSS applied (~363 K with SSS), while the coolant temperature peaks at 332.2 K with the PSS (~333.1 K with the SSS). This slower rise in the coolant temperature is due to the flywheels slowing-down the coastdown of the pumps. The temperature increase in the LOFA₁ was more rapid due to the loss of the flywheel with the pump, which is not the case for this LOFA₂ accident where the two lost pumps retain their flywheels. This affirms the importance of the flywheels for the NNS's safety in accident conditions such as LOPAs and LOFAs. There were no other notable deviations between the PSS and SSS temperature behaviors for the LOFA₂.

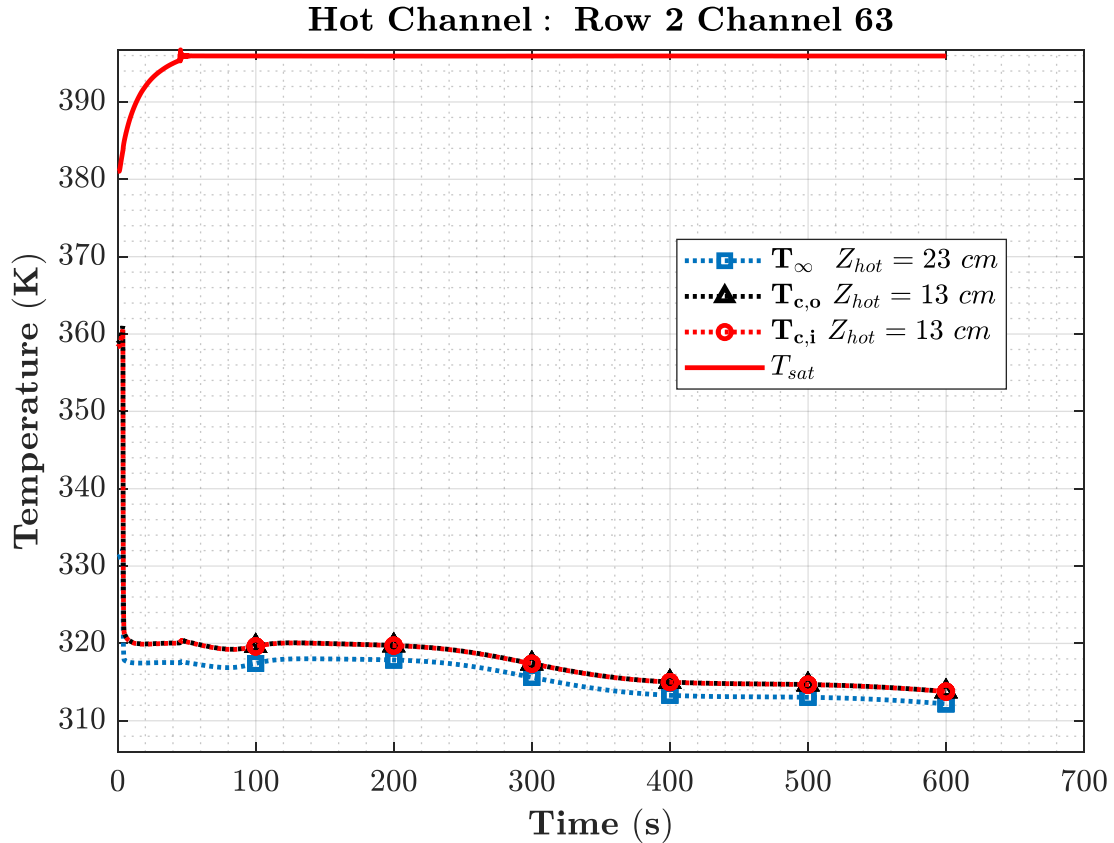


Figure 34. The temporal evolution of temperatures throughout a loss of two pumps LOFA transient with the PSS applied.

The mCHFR temporal evolution for the LOFA₂ with the PSS is shown in Figure 35, where Mirshak offers more limiting margins. The mCHFR behavior is qualitatively identical for both correlations. Both Sudo-Kaminaga and Mirshak exhibit a margin from the limit of mCHFR= 2 (for both PSS and SSS), demonstrating the NNS’s capability of safely managing the LOFA₂. A feature of the mCHFR profile is a dip in mCHFR observed at the ~45 seconds point, due to flywheels stopping. The rise in mCHFR that follows that dip is attributed to the exponential drop in the reactor power post shutdown.

A reoccurring observation is Mirshak offers the more limiting estimate of the safety margin for mCHFR profiles on multiple accidents. However, as shown in Figure 35, Sudo-Kaminaga becomes more limiting than Mirshak as the accident progresses and, in particular, when considerable amounts of flow are lost (i.e., LOPA and LOFA₂). This indicates that under low-flow conditions, Sudo-Kaminaga yields more limiting mCHFR values for the NNS. Note that the Mirshak correlation is valid to a minimum Re of 9×10^3 (refer to part 3.5.1.1 of this document), which makes the correlation prone to large errors in low-flow conditions including natural circulation.

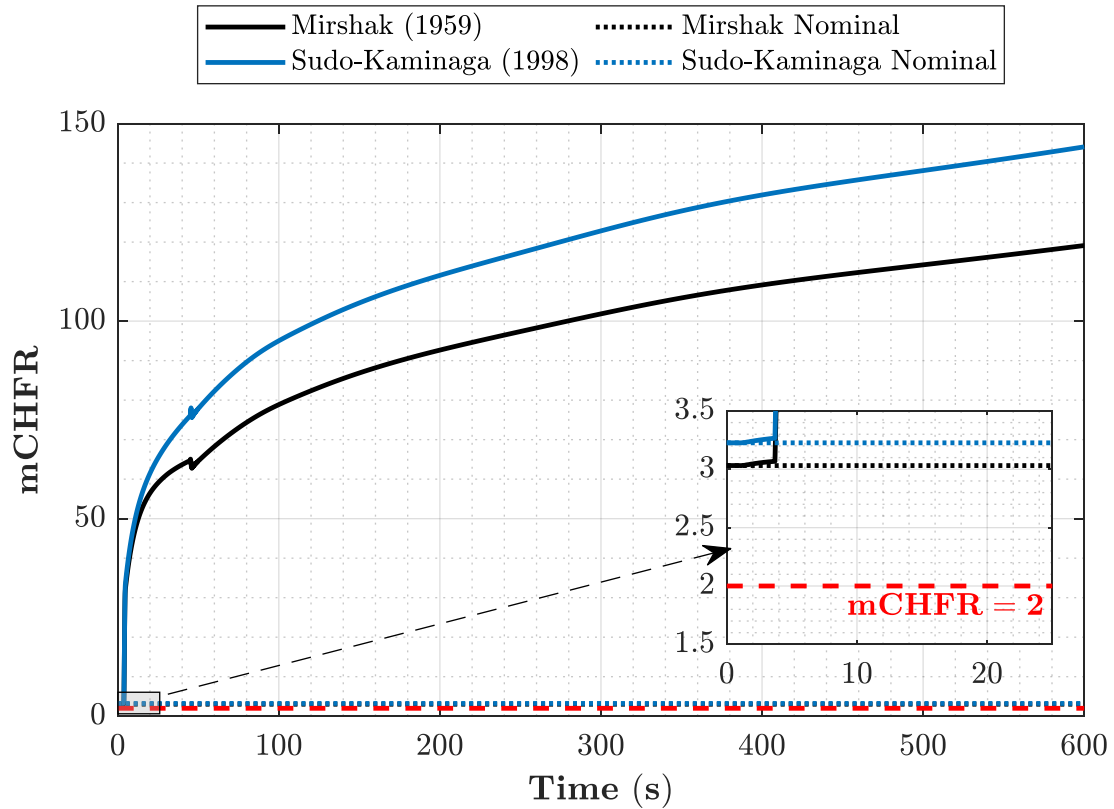


Figure 35. The temporal evolution of mCHFR throughout a loss of two pumps LOFA transient with the PSS applied.

The mOFIR behavior is illustrated in Figure 36, where a similar qualitative behavior to mCHFR is observed. The Costa correlation yields the more limiting mOFIR margin in the early stages of the accident, but as the accident progresses, Saha-Zuber becomes more limiting. The dip caused by the flywheels' loss of momentum is visible in Figure 36 at ~45 seconds. Both the Saha-Zuber and Costa correlations demonstrate near identical qualitative evolution in the mOFIR; and both show mOFIR is maintained above two throughout the LOFA₂. The SSS behavior (Figure 67) is qualitatively identical to that of the PSS shown in Figure 36 (except for the two-second delay from the SSS activation [Table 6]).

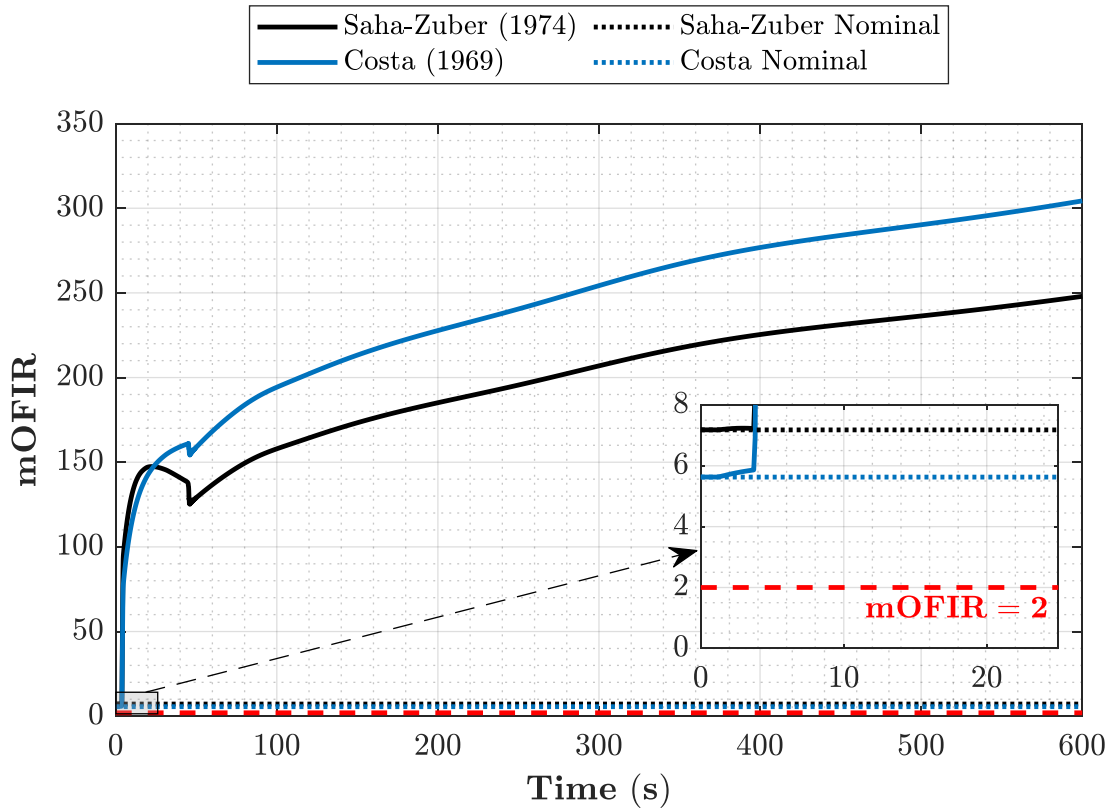


Figure 36. The temporal evolution of mOFIR throughout a loss of two pumps LOFA transient with the PSS applied.

The mONBR (shown in Figure 37) shows a similar behavior to the other safety margins, which includes the dip caused by the flywheels stopping. For both the PSS and SSS, the mONBR remains above unity, indicating that single-phase convection is maintained throughout the LOFA₂. The delay from the SSS activation does not yield any detrimental effects to the NNS's ability to recover from the LOFA₂. The difference between the PSS and SSS regarding mONBR's evolution in the LOFA₂ is the lighter rise in mONBR after the commencement of the shutdown system. In the PSS (Figure 37), the rise is linear and with a sharp slope. In the SSS (Figure 68), the rise is more gradual with a softer slope. Both the PSS and SSS demonstrate similar safety margins and temperatures, yielding minimal quantitative difference and reaffirming that the NNS can cope with the LOFA₂.

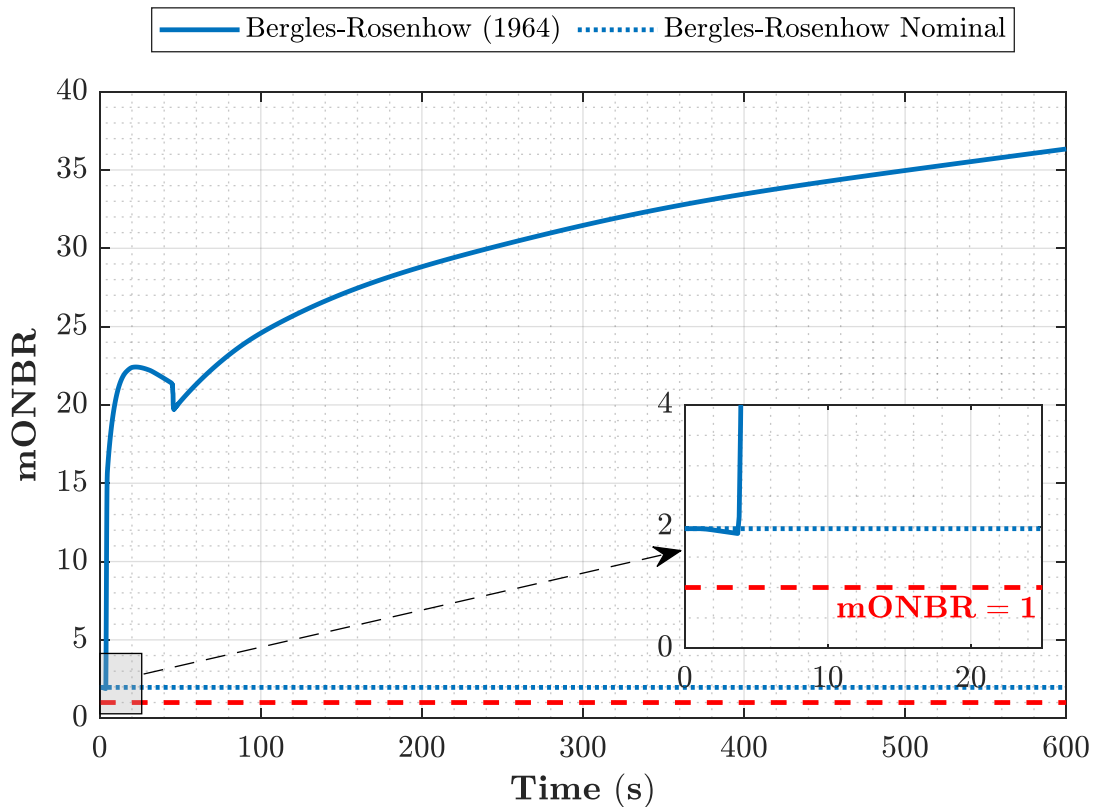


Figure 37. The temporal evolution of mONBR throughout a loss of two pumps LOFA transient with the PSS getting used.

5.5. Loss of Coolant Accidents

Two loss of coolant accidents (LOCAs) are analyzed as explained in section 3.4. The first LOCA assumes a 0.1 m diameter break (LOCA₁) and the second LOCA assumes a 0.2 m diameter break (LOCA₂). This section provides results of both LOCAs utilizing the PSS. For both of the LOCAs, the shutdown systems are applied via an instantaneous pressure drop trip.

5.5.1. The 0.1 m break

Figure 38 shows the temporal evolution of the temperatures throughout a LOCA₁ with the PSS applied for the hot channel and the hottest elevation represented by Z_{hot} cm from the axial centerline of the fuel. The hottest channel in this transient (with the PSS applied) is channel 63 in row 2 (like the accidents discussed), where the hottest coolant temperature is reached at an elevation of 37 cm below the fuel core centerline. The hottest cladding temperatures are reached at an elevation of 17 cm below the centerline. For the majority of the LOCA₁, the temperatures remain below the saturation temperature; the one exception is the cladding temperatures rise ~7 K above the saturation temperature at ~94 seconds into the LOCA. At this ~94 seconds point, we expect the coolant would transition to two-phase flow. The peak's FWHM is ~1 second, implying that any local boiling should not last beyond a second. Note that the peak cladding temperature is

~405 K, which is much lower than the blistering temperature. The cladding temperature is only a few degrees different than fuel temperature which is the basis for concluding that temperatures remain much lower than the safety limit.

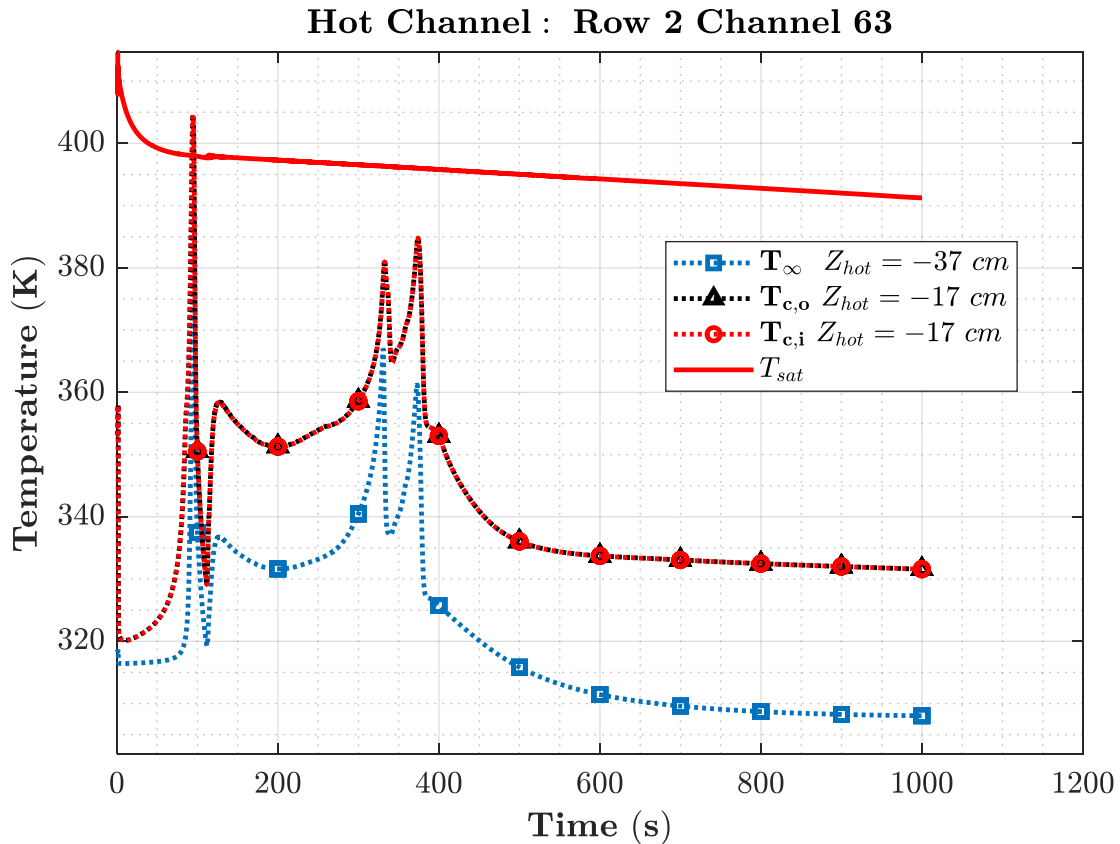


Figure 38. The temporal evolution of temperatures throughout a LOCA transient (0.1 m break) with the PSS applied. Note that usage of SSS instead of the PSS yields near identical results (no notable variations).

The mCHFR evolution throughout the LOCA₁ is shown in Figure 39 alongside the mass flow rate (\dot{m}). The \dot{m} evolution is relevant to understand the variations in the safety margin, where dips and rises in the mCHFR profile can be related to variations in \dot{m} . Due to \dot{m} switching between upflow and downflow throughout the LOCA₁, the Mirshak correlation is inappropriate for this incident. So, we used the Sudo-Kaminaga correlation assess the mCHFR behavior in the LOCA₁.

Three distinct periods were identified for the LOCAs: they are separated by vertical dashed lines and are color-coded. The first period is the coastdown period, spanning the first ~90 seconds of the LOCA₁. Following the coastdown period is a period of stagnant or reverse flow, spanning the period of ~90-330 seconds. After the stagnant flow period, natural circulation becomes the dominant form of cooling, allowing the safety margins to stabilize. Throughout the duration of the LOCA₁, mCHFR experiences the most limiting and unstable conditions in the stagnant flow period, where forced convection is lost or near lost, and natural circulation is still developing.

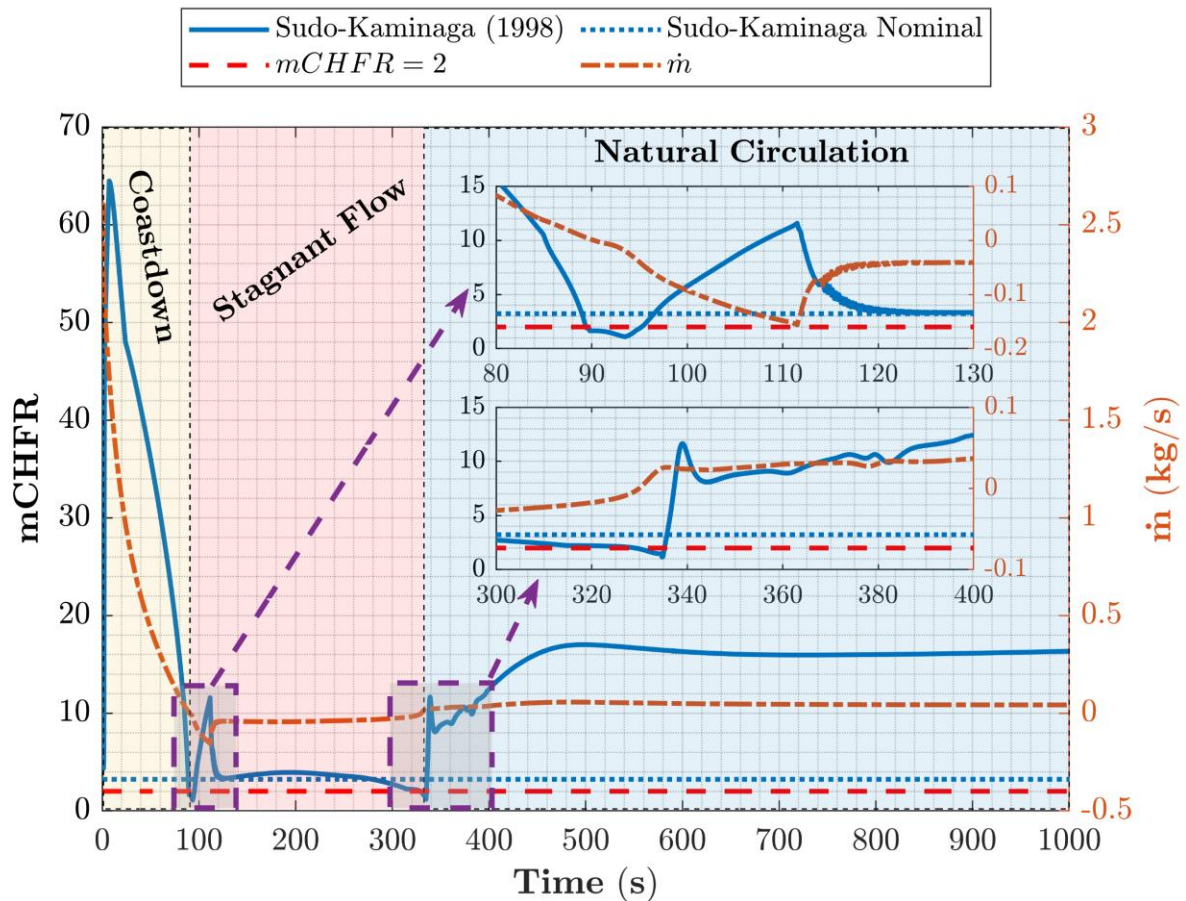


Figure 39. The temporal evolution of mCHFR and mass flow rate throughout a LOCA transient (0.1 m break) with the PSS applied. Note that usage of SSS instead of PSS yields near identical results (no notable variations).

Per Figure 39, mCHFR starts dropping ~7.5 seconds into the LOCA₁, where the flow coastdown begins. The mCHFR continues dropping throughout the coastdown period and into the stagnant flow period. At the start of the stagnant flow period, \dot{m} approaches zero, and at the ~90 second point, mCHFR dips below two. The flow remains stagnant (i.e., near-zero) in the 90-94 seconds period and the absolute mCHFR is reached at ~93.5 seconds (mCHFR~1.09), after which the flow accelerates in the reverse direction (i.e., $\dot{m} < 0$, or downflow) due to hydrostatic head. The accelerated downflow allows mCHFR to rise again in the ~94-110 seconds period. At the 110 second point, the flow decelerates (maintaining the downflow orientation). It settles at a minimal flow rate, signaling a stagnant flow period that lasts until ~330 seconds. At this point, the flow reverses again and returns to upflow conditions. In this flow reversal, \dot{m} approaches zero again and mCHFR dips back below two. At ~340 seconds, the natural circulation in the pool enables upflow to be maintained at ~0.04 kg/s, which enables mCHFR to rise back up and settle at a comfortable margin (Figure 39).

The mOFIR exhibits similar trends to the mCHFR, as shown in Figure 40, where the safety margin's behavior is again tied to the \dot{m} evolution throughout the LOCA₁. Note how Saha-Zuber

and Costa correlations show deviations in their predictions of mOFIR evolution. The variations between the correlations demonstrate a potential need for more detailed understanding of the q''_{NVG} for scenarios that involve transition from forced convection to natural convection. The Costa correlation yields the more limiting mOFIR, which occurs at the start of the stagnant flow period (at ~90 seconds into the accident). Around that same time, the Saha-Zuber predicts an mOFIR of ~50, which is too high considering the high-water temperature and low mass flow rate at that point. Saha-Zuber may struggle to predict q''_{NVG} in low-flow regimes.

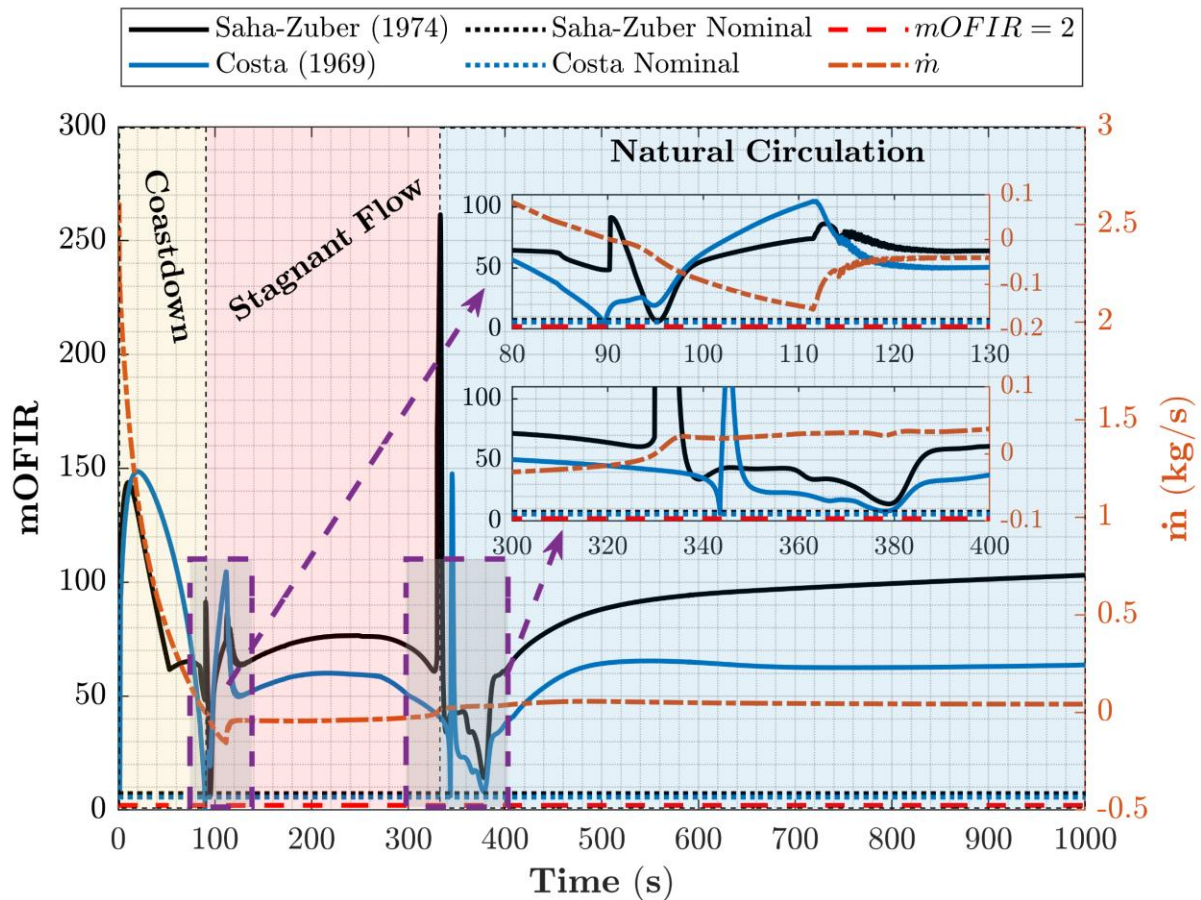


Figure 40. The temporal evolution of mOFIR and mass flow rate throughout a LOCA transient (0.1 m break) with the SSS applied. Note that usage of SSS instead of PSS yields near identical results, except the Costa correlation predicts a higher mOFIR peak at 350 s ($mOFIR_{SSS} \sim 40$; $mOFIR_{PSS} \sim 150$).

The mONBR evolution throughout the LOCA₁ is shown in Figure 41, which follows the same trends as the other safety margins for the LOCA₁. Being the most limiting of the safety margins, mONBR appears to remain above unity throughout the majority of the accident, except for a dip at ~90 seconds (the start of the stagnant flow region), yielding an absolute mONBR of ~0.69 at the 94.4 second point. The dip of mONBR below unity indicates that nucleate boiling occurred. Although some water boiling is anticipated during the LOCA₁, it is unlikely that the fuel cladding integrity would be compromised (given the maximum cladding temperature reached in Figure 38).

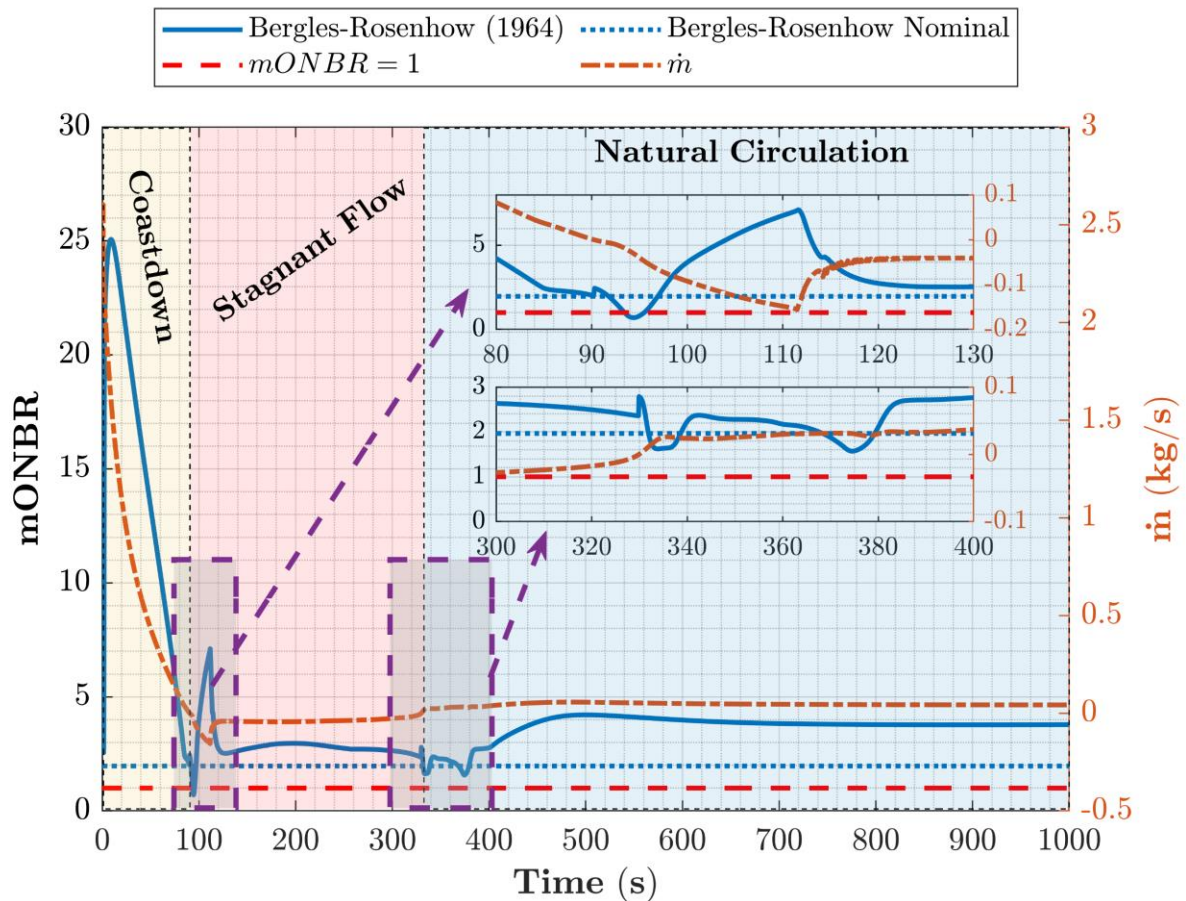


Figure 41. The temporal evolution of mONBR and mass flow rate throughout a LOCA transient (0.1 m break) with the SSS applied. Note that the usage of PSS instead of SSS yields a higher mONBR peak in the coast-down period (mONBR_{SSS}~21; mOFIR_{PSS}~25).

5.5.2. The 0.2 m break

The temporal evolution of temperatures in the hot channel for a LOCA₂ is shown in Figure 42. The hot channel is again found to be channel 63 in row 2 of the NNS, where the hottest coolant temperature is reached at an elevation of 23 cm above the fuel core centerline. The hottest cladding temperatures are reached at an elevation of 13 cm above the centerline. The LOCA₁'s maximum temperatures were all found below the fuel centerline, whereas the LOCA₂'s maximum temperatures are above the fuel centerline. This deviation is a consequence of the steep reduction in mass flow rate at the start of the transient, causing the hottest cladding temperatures in LOCA₂ to be reached at the start of the accident (note the peak at ~1.6 seconds in Figure 42). At this time, the forced convection is maintained by the flywheels, but less coolant is available towards the top of the pool due to the larger break size causing some water to be lost during this coastdown period. This reduction in upflow, which is most severely experienced in the first ~1.6 seconds of the transient, is the reason why the hot spot is at a higher elevation than the one reported in LOCA₁.

The maximum cladding temperature reached at ~1.6 seconds and ~408.7 K is lower than the blistering temperature. In Figure 42, three other peaks are at ~135 seconds, ~300 seconds, and

~341 seconds, similar to LOCA₁. The peak at ~341 seconds is the greatest of the three, yielding clad temperatures of ~392 K, exceeding the saturation temperature for 5 seconds. At each of those peaks, T_∞ does not exceed saturation temperature, where the maximum T_∞ is reached at ~137 seconds with a temperature of 382.4 K (~10 K lower than the saturation temperature at that time).

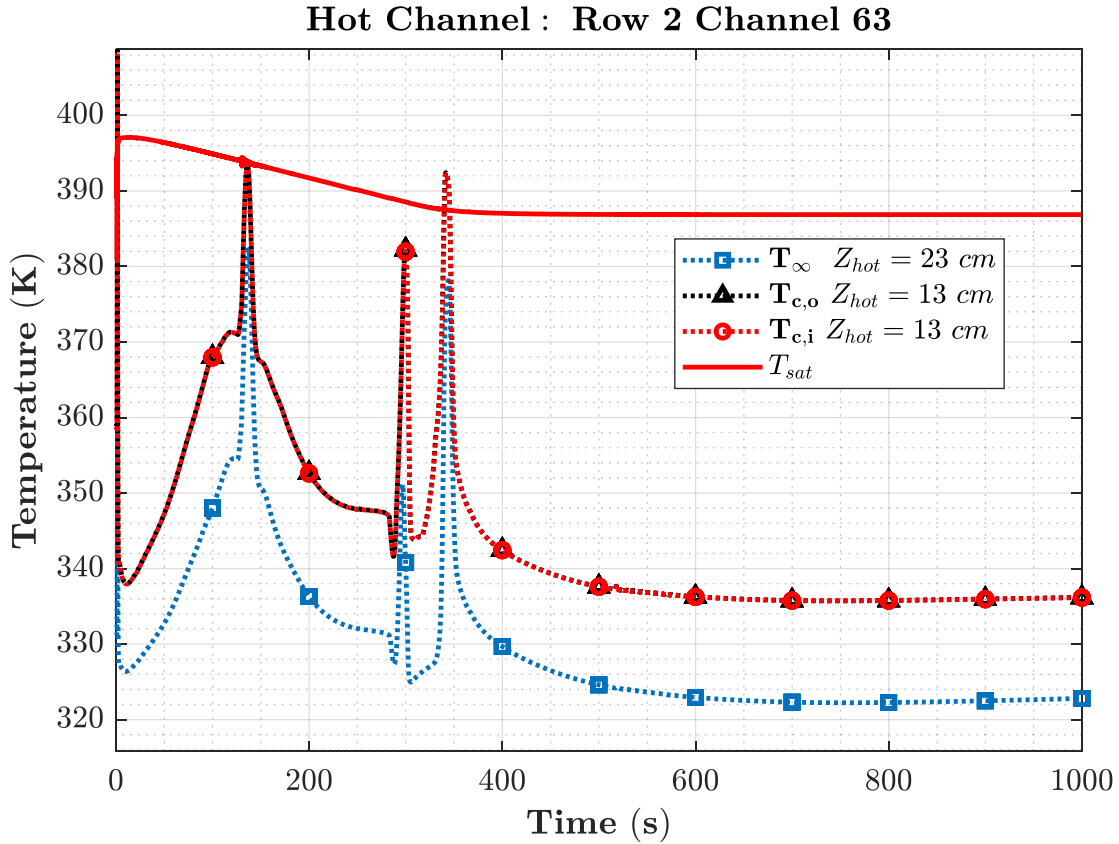


Figure 42. The temporal evolution of temperatures throughout a LOCA transient with the PSS applied.

The mCHFR evolution throughout the LOCA₂ is shown in Figure 43, where only the Sudo-Kaminaga correlation was utilized because it has greater flexibility compared to the Mirshak correlation. For each temperature peak in Figure 42, a corresponding dip in mCHFR is observable in Figure 43. Per Figure 43, the mCHFR dips appear to overlap with variations in \dot{m} , showing the same \dot{m} -dependent behavior observed for LOCA₁. An increase in the flow rate magnitude (in either flow direction) causes growth in mCHFR; the opposite is also true. The dips and rises in \dot{m} during the stagnant flow period occur because the flow switches directions (from upflow to downflow, then back to upflow). Every time the flow changes directions, \dot{m} approaches zero, which causes a peak in temperatures and a corresponding dip in mCHFR. Note that \dot{m} fluctuates early in the stagnant flow period (at ~130 seconds); this is also observable in LOCA₁ as shown in Figure 39. Much like the LOPA (Figure 15), \dot{m} fluctuations are due to flow instability occurring with the transition from forced to natural convection, which was observed in other cases in literature [47].

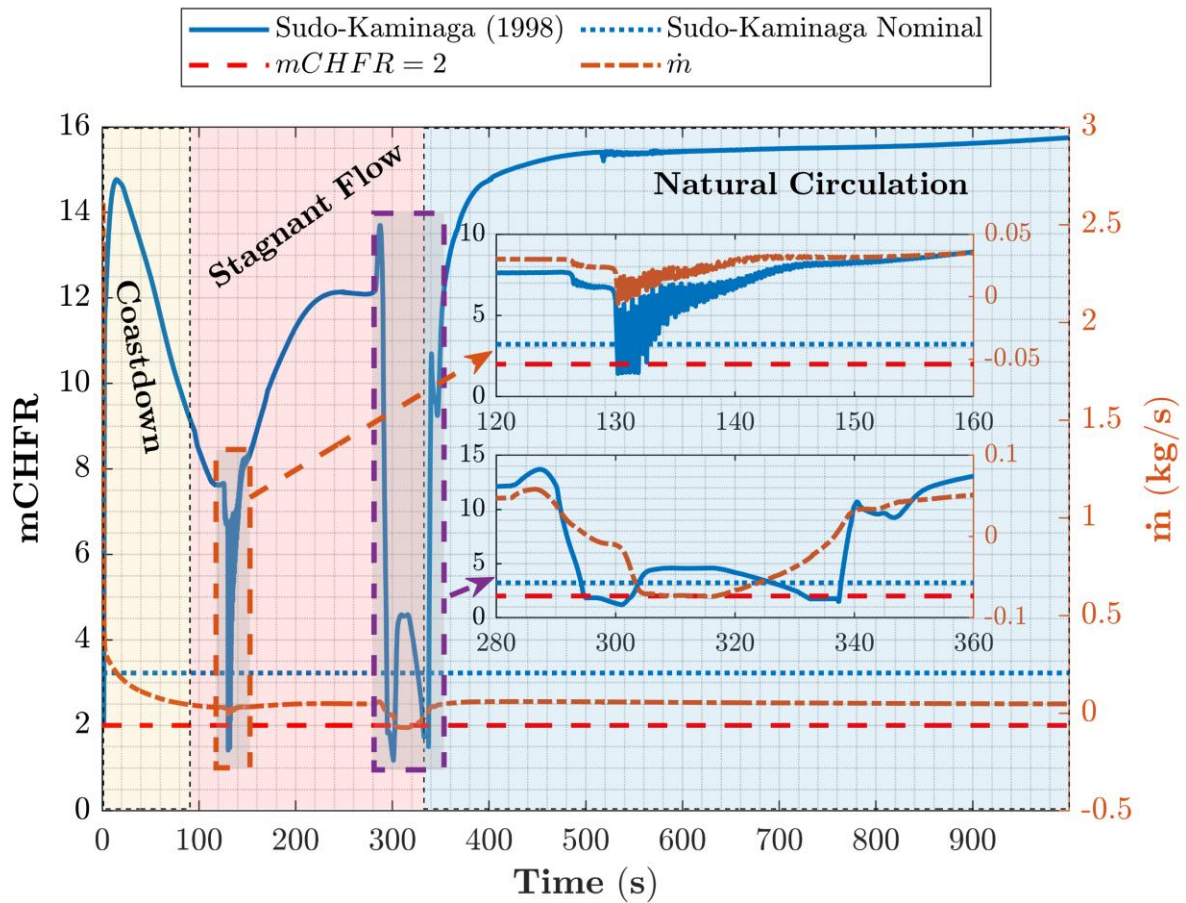


Figure 43. The temporal evolution of mCHFR and mass flow rate throughout a LOCA transient (0.2 m break) with the PSS applied.

The mOFIR evolution for LOCA₂ is shown in Figure 44, where both the Saha-Zuber and Costa correlations are shown throughout the accident. Like mCHFR, the mOFIR is tied to \dot{m} behavior, where both safety margins exhibit qualitative similarities. The fluctuations observed at ~130 seconds are also present for mOFIR, and the peaks and dips in the safety margin occur at the same times as mCHFR peaks and dips. The same observation from mCHFR persists for mOFIR: the safety margin dips as flow rate approaches zero (during flow-reversal), and vice-versa. The Costa correlation yields a more conservative estimate of mOFIR than the Saha-Zuber correlation, suggesting that Saha-Zuber struggles to predict q''_{NVG} in low-flow regimes. Note that mOFIR reaches unity at ~130 seconds into the accident, which is attributed to the fluctuations in \dot{m} . Due to the fluctuations, mOFIR does not remain at unity for more than an instant; it rises to higher values immediately after this dip. At ~294 seconds, mOFIR dips below two again, reaching 1.85 for an instant before rising as the flow reversal continues past $\dot{m} = 0$. The most drastic dip in mOFIR for LOCA₂ is observable at ~340 seconds, where it dips to the absolute minimum of 0.36. This drastic dip in mOFIR is attributed to flow reversal: the flow goes from downflow back to upflow.

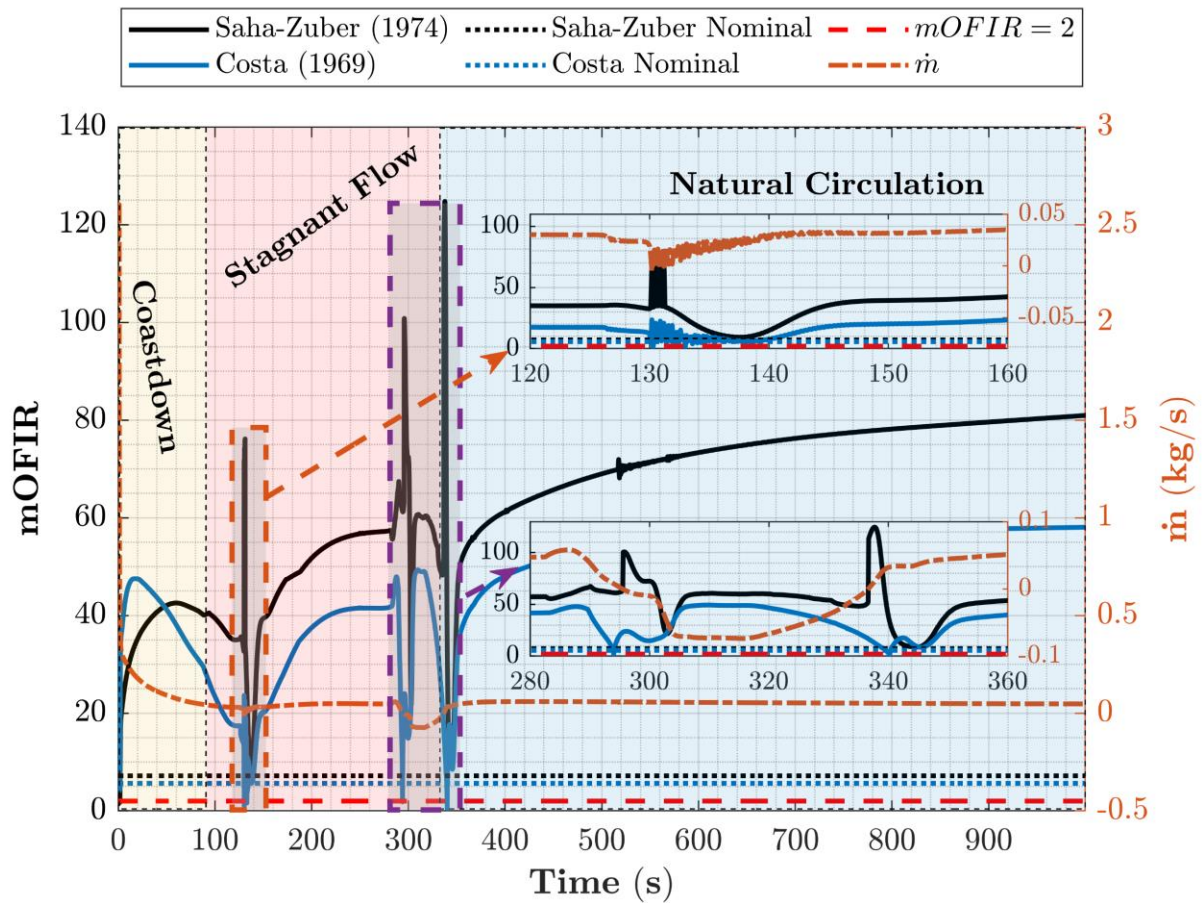


Figure 44. The temporal evolution of mOFIR and mass flow rate throughout a LOCA transient (0.2 m break) with the PSS applied.

The mONBR evolution throughout LOCA₂ is shown in Figure 45, where mONBR shows similar qualitative behaviors to mCHFR and mOFIR. An interesting deviation is the absence of oscillatory behavior in the safety margin during \dot{m} fluctuations at ~130 seconds, where mONBR shows a smooth dip in its value throughout that period. The absolute mONBR throughout LOCA₂ is also observed during that dip, where mONBR reaches a minimum value of 0.83 at ~137.8 seconds. The only other time that mONBR dips below unity is at ~345 seconds, where it reaches a minimum value of 0.88. This indicates that two-phase flow is expected every time \dot{m} reaches zero during a LOCA. Although some water boiling is anticipated during LOCA₂, it is unlikely that fuel cladding integrity would be compromised (given the maximum cladding temperature reached in Figure 42). This concludes our analyses of all accident scenarios for the current NNS preconceptual design.

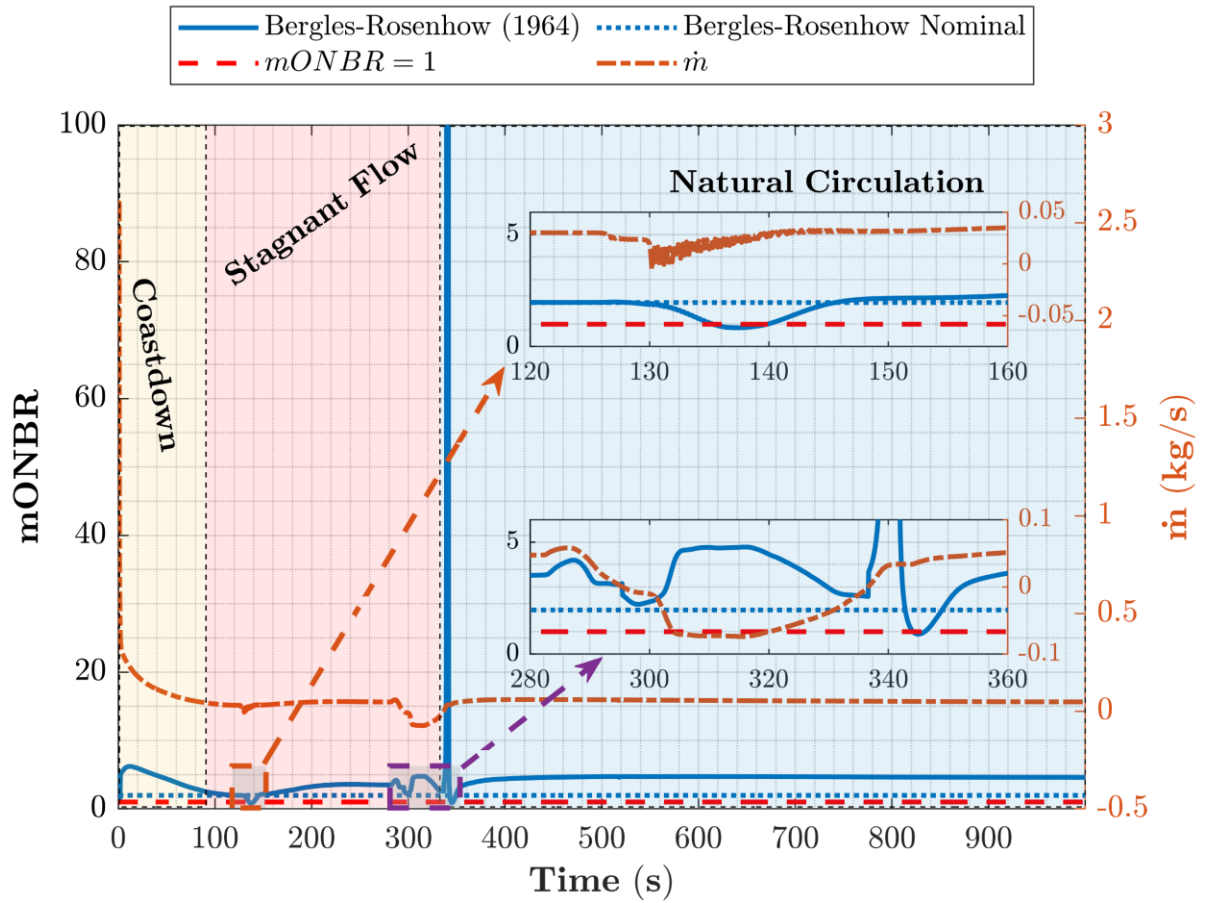


Figure 45. The temporal evolution of mONBR and mass flow rate throughout a LOCA transient (0.2 m break) with the PSS applied.

6. Flow Behavior Assessments

To understand flow behavior in the regions identified in subsection 3.6.1, several CFD models were developed using Reynolds-Averaged Navier-Stokes (RANS) turbulence models. Although Large Eddy Simulation (LES) models were considered for the current NNS design, RANS models are more appropriate. Note that all flow behavior assessments remain in progress by the team working on the NNS; the results in this report are preliminary.

6.1. Inlet Region Behavior & CFD Modeling

A demonstration of the flow phenomena is expected at the inlet region, specifically in the intermediate mixing region within the row window (Figure 10). Experiments in literature regarding triple-channel mixing [42] demonstrate reduced momentum for flow exiting the inner (middle) channel due to the presence of two mixing layers bounding the flow. Note that triple-channel mixing is unique from triple-jet mixing due to the availability of walls bounding the flows exiting from the outer channels. So, only triple-channel mixing experiments are relevant for development and validation of NNS inlet models because of the walls' presence around the flows leading-up to the outer fuel assemblies.

Preliminary CFD assessments for the inlet region flow phenomena [43, 48] yielded a qualitative understanding of the velocity and its expected behavior at the inlet of the core, shown in Figure 46. In Figure 46, the profile on the left represents the dimensionless streamwise velocity (V/V_∞); the profile on the right represents the dimensionless spanwise velocity (U/V_∞). Note that line traces of the respective velocities are overlaid on their respective profiles, where three RANS models are highlighted, showing slight variations between them. Note that all RANS models were able to predict counter-rotating pairs of vortical structures at the separation point prior to the flows entering the legs. Elevated streamwise velocities are observable in the legs due to the reduction in flow area, but no model captures mixing between the flows in the intermediate mixing region. Qualitatively, the RANS turbulence models we investigated yielded similar results. However, quantitative differences were observed. In particular, the largest variations between the models are observed at the point of flow separation, and in the intermediate mixing region.

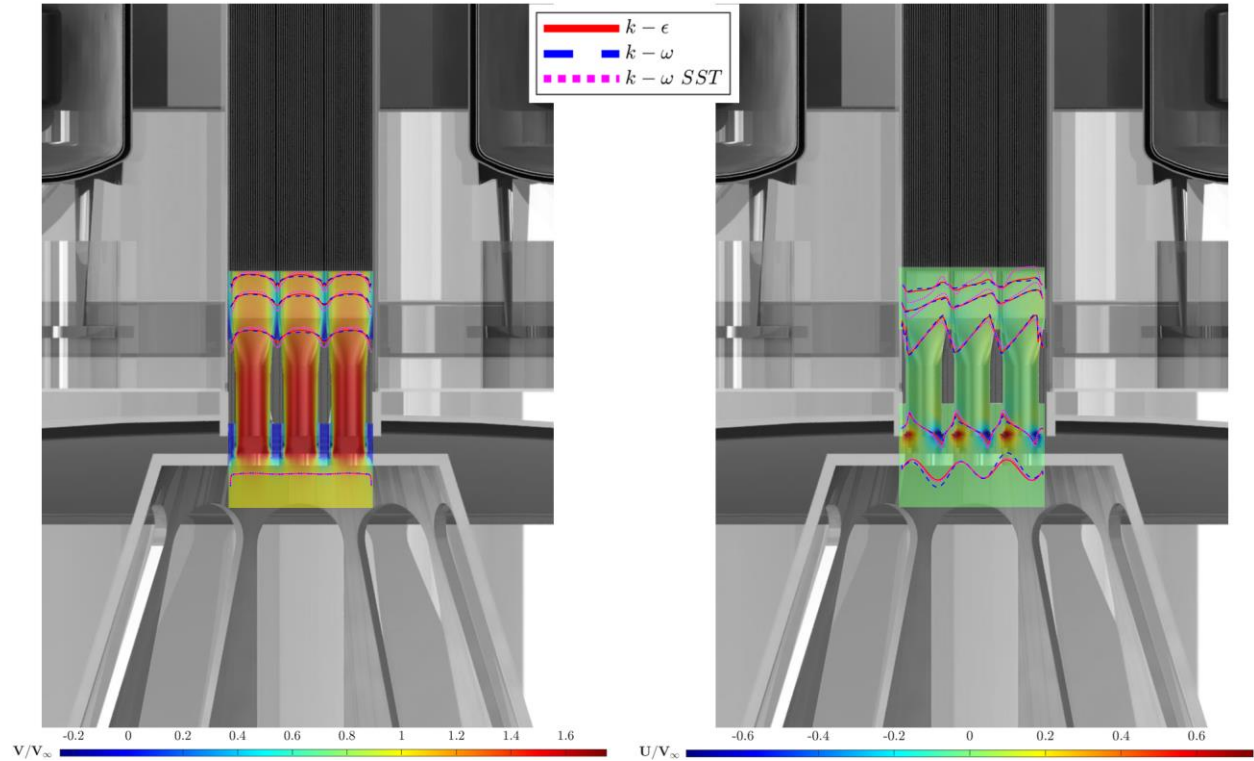


Figure 46. The streamwise and spanwise velocity profiles at the inlet according to the preliminary CFD assessments.

Model prediction of separation and mixing phenomena were sensitive to variations in the RANS turbulence model. The most dramatic difference in the results is clearest in the spanwise velocities, specifically in the intermediate mixing plenum and upstream of the FPs. Deviations in streamwise velocities are less dramatic; however, there are some variations. To understand the deviation between all models investigated in this work, the standard deviation in the profiles between each two models (σ_V or σ_U) is divided by their average (\bar{V} or \bar{U}) and represented by a percentage, yielding the graphical deviation matrices shown in Figure 47.

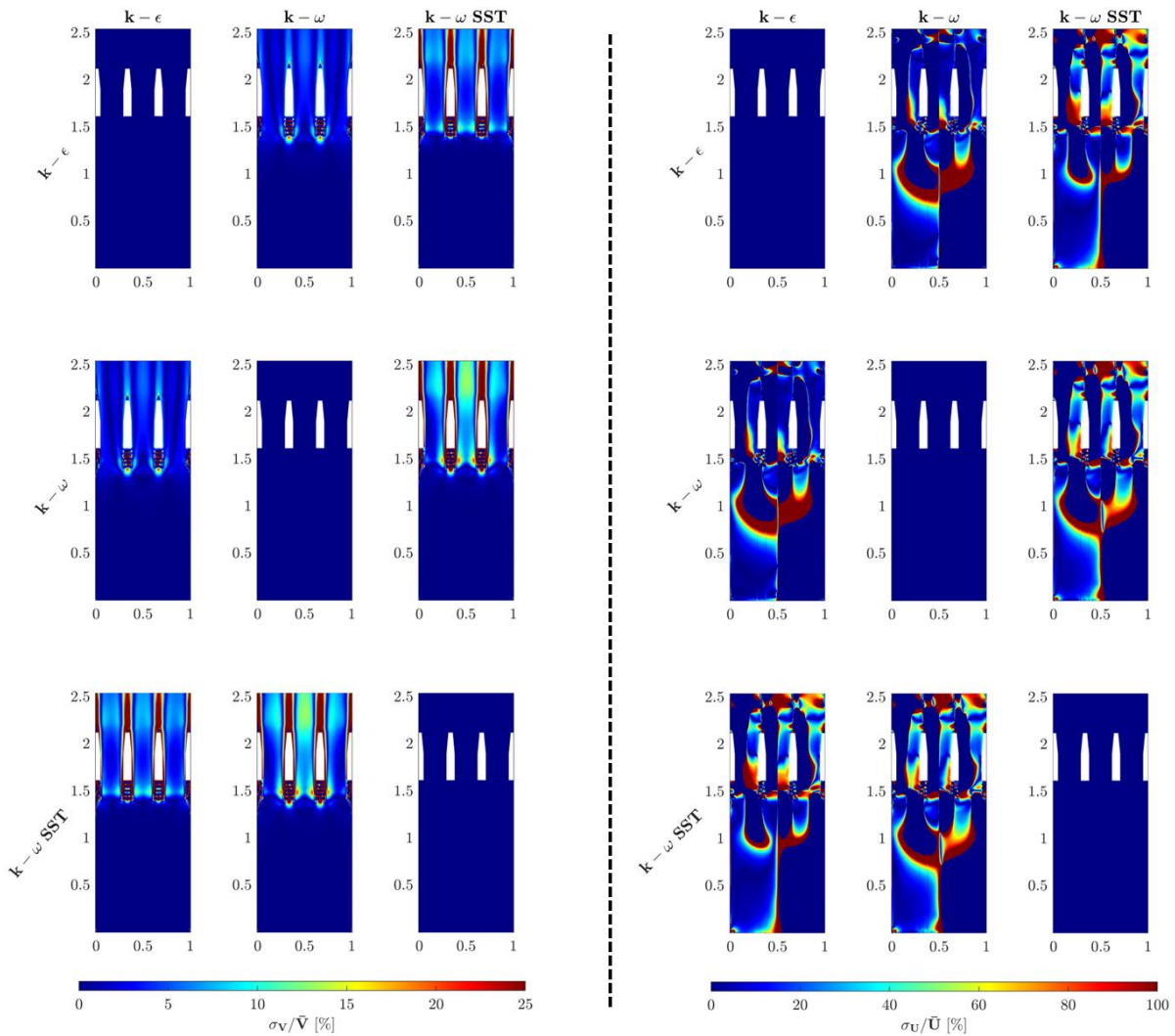


Figure 47. Graphical deviation matrices between different RANS models for predictions in streamwise velocity (left) and spanwise velocity (right). Here, deviation is the standard deviation between any two profiles divided by their average.

The left side of Figure 47 shows the covariance matrix for streamwise velocity (V), while the right side shows the covariance matrix for spanwise velocity (U). The first row of a matrix shows $k-\epsilon$ model deviation from the other models in each of the columns. The second row shows the $k-\omega$ deviation from the other models. The third row shows the $k-\omega$ SST model deviation from the other models. In covariance matrices, the deviation matrix yields zeros along the diagonal. Note how minimal-to-no deviation is encountered between the models' streamwise velocity predictions far upstream of the legs. But deviation rises upstream the flow separation into the separate legs. This deviation is exacerbated when considering the spanwise velocity profiles, which show deviations (in excess of 100%) as early as the inlet. This indicates that the effects of flow separation are perceived by the flow well upstream from the point of separation. The most notable deviations in the spanwise profiles appear ~ 0.75 diameters downstream of the inlet, or ~ 0.75 diameters upstream of the legs. This is consistent across all models. The deviations in both the U and V profiles worsen as the flow continues through the legs and into the mixing region. Observe the greatest deviations

in the V profiles in the intermediate mixing region (the window), particularly in-between the channels exiting the legs. These deviations indicate that the RANS models disagree on how the flow separates into the legs and how the flow mixes and separates again after it exits the legs. Considering the results of the simulations described in this work and considering results from literature [42] showing notable decreases in the central flow ($\geq 25\%$) due to shear layers, further analyses are relevant for calculating adequate inlet flow distributions. This demonstrates a need for additional studies on validating models for turbulent channel mixing and separation.

6.2. Active Height Behavior & CFD Modeling

The core is expected to have large bulk channel velocities based on the previous subchannel analyses [49–51], our analyses in section 3.5 and chapters 4-5. This may cause investigations into alternative approaches for estimating the thermal-hydraulics safety margins. Additionally, we know from previous subchannel analyses that the core will likely maintain favorable thermal-hydraulics safety margins during normal operation, which was verified by studies in this report. However, the NNS's behavior during accidents that involve the loss of forced convection require the NNS to rely on natural circulation for cooling the core, which is not accounted for in the existing safety margins correlations such as Sudo-Kaminaga [12]. CFD models of the coolant channels can be the first and easiest gateway into better understanding how the NNS flow conditions in both normal operations and transient scenarios affect the reactor's cooling effectiveness.

The first step towards this assessment is discussed in this work, which includes the development of a validated single-phase flow model and an exploration of the need to represent the 3-dimensionality of the channel. For the validation data set, the work of Ha et al. [52], where non-intrusive (i.e., no probes involved) velocity measurements were obtained in a test section emulating the geometry of a material test reactor (MTR) fuel element. Such MTR fuel elements include the curved FP design adopted for the NNS, making the Ha experiments applicable for validating CFD models of the FP-FP channels in the NNS. Two types of meshes were generated for the single channels (Figure 48), a 2D mesh that ignores the curvature of the channel, and a 3D mesh that includes the curvature of the channel show.

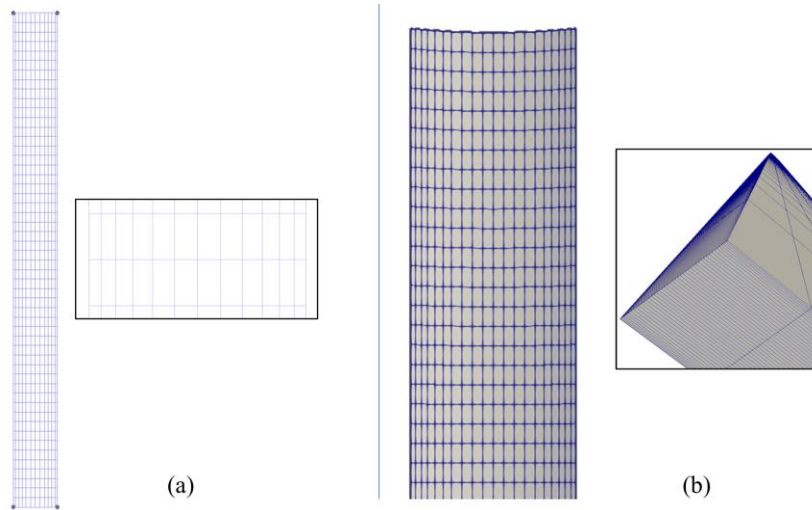


Figure 48. The (a) 2D mesh and (b) 3D mesh implemented for the single-channel validation studies.

Grid sensitivity analyses were conducted on both of the meshes by computing a grid convergence index with recommendations from the ASME V&V 20 standard [53], and in agreement with other recommendations [54] and CFD studies in literature [38, 55]. The 2D mesh was developed with a mesh resolution offering $2.5 \leq y^+ \leq 5$, whereas the 3D meshes were developed with a mesh resolution offering $2 \leq y^+ \leq 3$. The meshes were used to set up three separate models (a total of six models), where each model adopted a different RANS turbulence model. The three RANS models considered for this work were the standard $k-\epsilon$, Realizable $k-\epsilon$, and Spalart-Allmaras. The $k-\epsilon$ RANS models were considered because they were calibrated for channel flow, which makes them valid for usage in simulating the FP-FP channels. The Spalart-Allmaras RANS model was considered because of its reduced computational cost for this work's simulations. A summary of the results is presented in Figure 49. Experimental data from Ha et al. were used to validate the models. The selected experimental data is for curved fuel channels and includes the Re range expected for NNS. As such, it is deemed appropriate for comparison of normalized velocity data presented in Figure 49.

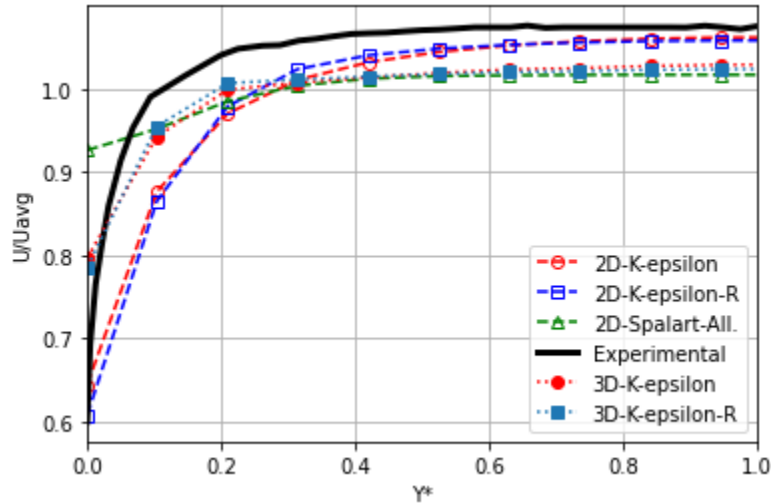


Figure 49. A summary of the validations from the findings of the single-channel study. Note the adoption of $Y^* = \frac{Y_{distance\ from\ wall}}{Width_{of\ channel}/2}$ to maintain consistency with the Ha et al. [52] presentation of results.

Per Figure 49, the 3D models offer closer agreement to the experimental results closer to the wall, but they interestingly underestimate the bulk flow (center of the channel). Considering y^+ values near the wall were maintained around two (near wall-resolved) for both meshes, much of this deviation between the 3D and 2D results is likely attributed to the curvature of the channel being considered in the 3D results. Note that the biggest deviation in the 2D results is near the walls, which is relevant considering the overall purpose of the CFD studies on the active height region of the NNS. This demonstrates that, for simulating nucleate boiling and departure from nucleate boiling, we should consider the curvature of the geometry due to the strong variation in the near-wall velocity behavior.

Considering the variations between the turbulence models, the 1-equation 2D model of Spalart-Allmaras yields close agreement to the 3D models in the bulk flow but demonstrates a notable deviation near the wall. This behavior is likely because the Spalart-Allmaras model was calibrated on flat-plate boundary layers, which contributes to the model's numerical forgiveness of near-wall mesh resolution enabling lower computational costs, at the expense of losing the effects of curvature at the walls. The $k-\epsilon$ models are very consistent with one another. Away from the walls, at the center of the channel ($Y^* = 1$), the variation between the 2D $k-\epsilon$ models is minimal, indicating that bulk velocity predictions in the channel are not sensitive to RANS model selection (based on the selected set of models). The variation between the 2D and 3D models' centerline velocity predictions is $\sim 10\%$, which promotes the requirement of accounting for curvature in the channel. It is not clear why the 3D models offer worse agreement with experimental values at the center of the channel in comparison to the 2D models. It is possible that the 3D RANS models are exaggerating the curvature effects in the channel centerline. This may be supported by the fact that the 2D channels, which lack the curvature representation, have much better agreement with the experimental results. Future studies would further investigate the findings and would focus on improving the implementations of the 3D meshes to better match the experimental results.

6.3. Outlet Region Behavior

The presence of the large hydrostatic force from the pool's water above the open chimney provides some buoyancy effects within few hydraulic diameters of the FA. This prompts questions on the mixing effectiveness at the outlet and the chimney's design (height of chimney and its connection to the hot leg). A design optimization would consider the effects of chimney and pool height on the retention of flow from the outlet towards the hot leg and the flow path during natural circulation or during a blockage of flow through the hot leg (via the siphon breaker). In particular, the design of the hot leg connection opening is interesting: its unique design presents manufacturing and quality assurance challenges. A simpler design may be investigated with an appropriate CFD model. The anticipated flow patterns at the outlet are illustrated in Figure 50.

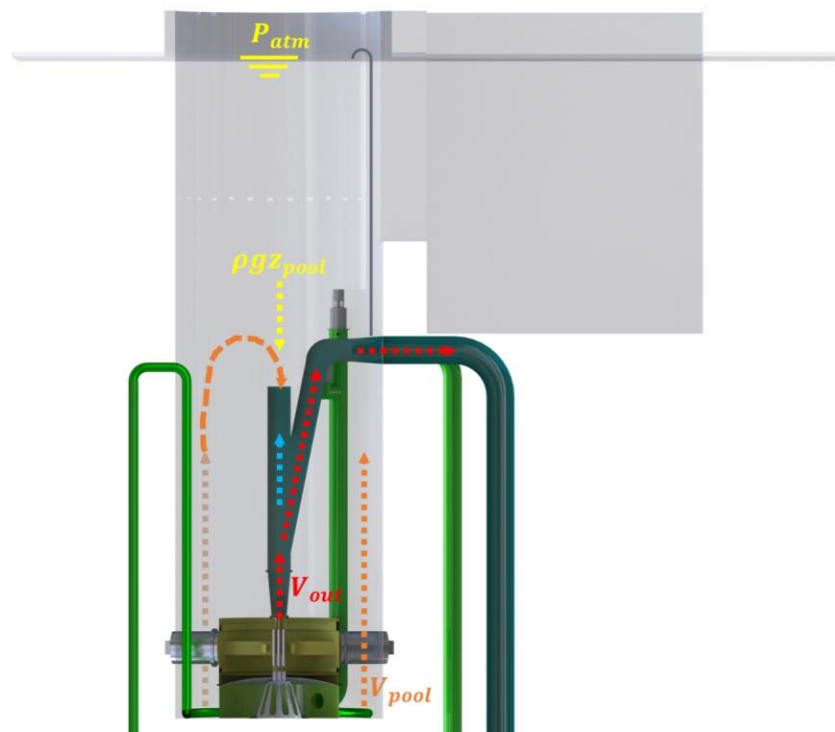


Figure 50. An illustration of the predicted flow patterns that could be encountered at the outlet of the NNS.

Per Figure 50, a holistic CFD model of the outlet region would consider the flow velocity from the pool cooling system (V_{pool}), the entire pool height (z_{pool}), the chimney, and the core's outlet velocity distribution (V_{out}). The sensitivity of the flow behavior (under forced or natural convection conditions) to each of the aforementioned considerations is unknown, but each of them plays a different role. The z_{pool} dictates the static pressure and hydrostatic force that counteracts any flow leaving the chimney's opening. The V_{out} informs the flow's mixing behavior downstream of the active height, and it dictates the total upward momentum of flow entering the hot leg and/or leaving through the chimney's opening. The V_{pool} may be the least relevant of the three considerations due to the minimal amount of bypass flow provided to the pool under normal conditions; but it is relevant when modeling the flow behavior during shutdown conditions, when

the shutdown system is turned on. Future studies should include scoping appropriate RANS models for simulating the flow under forced and/or natural convection conditions, and pursuing verification and validation activities in qualifying the CFD model(s) for design optimization studies.

7. Conclusions

A multi-scale assessment was conducted for the thermal-hydraulics characteristics of the NNS preconceptual design, including core-level, system-level, and finite-volume CFD simulations. Core- and system-level thermal-hydraulics analyses were conducted using TRACE, demonstrating the safety and reliability of the system in normal operating conditions and in various accident scenarios. In nominal conditions, a $m\text{CHFR} > 3$, $m\text{OFIR} > 5$, and $m\text{ONBR} \approx 2$ values were achieved, maintaining safety per recommendations from literature. The highest temperature reached under nominal conditions was for the cladding temperature with a value of ~ 365 K, remaining well below the blistering temperature.

Six accident categories were investigated. Eight accidents were simulated favorable cladding temperature results. No accident allowed the cladding temperature to exceed that of the blistering temperature. In some accidents (the one-pump seizure LOFA and the two LOCAs) demonstrated brief transitions to two-phase flow during the accident progression. In the LOCAs, we found that a large break would yield brief instances of departure from nuclear boiling or burnout. Due to the presence of the pool as a large heat sink, these unfavorable conditions do not extend beyond approximately one second, where the cooling offered by natural circulation becomes sufficient to counteract the effects of the LOCA.

CFD analyses sectioned the core into three distinct zones: the inlet region, the active height, and the outlet region. Each region demonstrated varying flow physics that required specialized treatment to capture. The inlet region offered a triple-channel mixing phenomenon found to be highly sensitive to the adopted RANS turbulence model. Such sensitivity requires additional validation of RANS models simulating this flow phenomenon. RANS models of the active height yielded favorable agreement with experimental data, where we found that 3D representation of the geometry is necessary to capture the behavior of the flow, particularly near the wall. In the future, additional refinements in the modeling approach are needed to better predict near-wall behavior. The outlet region flow evolution was hypothesized, leaving analyses towards this flow topology to future works.

8. Recommendations for Future Works

Pre-conceptual work has suitably analyzed NNS while later work will require incorporating uncertainties with an expectation to maintain substantial margins. We recommend independent verifications of the NNS steady-state and transient models by colleagues outside of the NCNR. Such verifications would help assess uncertainties in the analyses that are impossible to assess with a reference due to the lack of a current NNS facility. Such verifications would adopt similar inputs to the analyses in this work, but they would diverge from our set of conditions and assumptions to demonstrate uncertainties tied to said inputs. We recommended that both NCNR and non-NCNR parties pursue studies towards the identification of a maximum hypothetical accident in the NNS that would act as a limiting condition for the NNS.

Given the complexity of the flow physics identified throughout the NNS, we recommend an expansion on our CFD efforts by both internal-NCNR and external-NCNR groups. In particular, the verification and validation (V&V) of triple-channel mixing RANS models, the development and V&V of heated single-channel models, and the modeling and V&V of the buoyancy effects on the outlet conditions are all efforts recommended for future works. Note that each of those subjects can provide valuable inputs to further optimize the NNS design features including, but not limited to, the height of the pool, the chimney design, the inlet plenum design, the latching mechanism design, and the fuel assembly design. Such analyses do not dictate the safety of the NNS, but they do inform analysts of potential avenues for design and/or safety optimization work.

Both the TRACE and CFD models require notable computational costs for simulating a given case, which is not favorable if the models are needed for usage in non-conventional applications outside static safety analyses. Such non-conventional applications include the development of a digital twin, or for coupling to a dynamic adjusting model of the plant. Such applications would be valuable to developing a simulator for reactor operator training, or for active condition monitoring and risk assessment of the plant conditions. Development and refinement of low-order models of thermal-hydraulics (and even neutronics) behaviors would be valuable to ensure the continuous availability and reliability of the NNS in the future. Therefore, we recommended that future works investigate the applicability of low-order models to the aforementioned non-conventional applications, and further refining existing ones [51].

References

- [1] US Nuclear Regulatory Commission (2020) TRACE V5. 0 Theory Manual: Field Equations, Solution Methods, and Physical Models.
- [2] NIST (2023) Safety Analysis Report (SAR) for License Renewal for the National Institute of Standards and Technology Reactor - NBSR; NBSR 14.
- [3] Prepared by INVAP for ANSTO (2004) Safety Analysis Report (SAR) for Replacement Research Reactor Facility. (Australian Nuclear Science and Technology Organisation (ANSTO)).
- [4] Celikten, Osman Ş., Weiss, Abdullah G., Şahin, Dağistan (2024) Pre-conceptual Design Activities of the NIST Neutron Source: Preliminary Neutronics Assessments. NIST Technical Note. (National Institute of Standards and Technology, Gaithersburg, MD), NIST TN 2316. Available at <https://doi.org/10.6028/NIST.TN.2316>
- [5] Research Reactor Benchmarking Database: Facility Specification and Experimental Data (2015) (INTERNATIONAL ATOMIC ENERGY AGENCY, Vienna). Available at <https://www.iaea.org/publications/10578/research-reactor-benchmarking-database-facility-specification-and-experimental-data>
- [6] American National Standard: for decay heat power in light-water reactors (1979) Available at <https://www.osti.gov/biblio/5517356>
- [7] Wachs DM, Glagolenko I, Rice FJ, Robinson AB, Rabin BH, Meyer MK (2012) Blister Threshold Based Thermal Limits for the U-Mo Monolithic Fuel System. Available at <https://www.osti.gov/biblio/1060991>
- [8] Jamison L, Stillman J, Jaluvka D, Mohamed W, Kim YS, Wilson E (2020) Review of the Technical Basis for Properties and Fuel Performance Data Used in HEU to LEU Conversion Analysis for U-10Mo Monolithic Alloy Fuel. (Argonne National Lab. (ANL), Argonne, IL (United States)), ANL/RTR/TM-17/19-Rev.01. <https://doi.org/10.2172/1663207>
- [9] Shiro N (1984) The maximum and minimum values of the heat Q transmitted from metal to boiling water under atmospheric pressure. *International journal of heat and mass transfer* 27(7):959–970.
- [10] Ledinegg M (1938) Instability of flow during natural and forced circulation. *Die Wärme* 61.
- [11] Mirshak S, Durant WS, Towell RH (1959) *Heat flux at burnout* (EI du Pont de Nemours & Company, Explosives Department, Atomic Energy ...), Vol. 355.
- [12] Kaminaga M, Yamamoto K, Sudo Y (1998) Improvement of Critical Heat Flux Correlation for Research Reactors using Plate-Type Fuel. *Journal of Nuclear Science and Technology* 35(12):943–951. <https://doi.org/10.1080/18811248.1998.9733966>

- [13] Şahin D, Çelikten OŞ, Gurgen A, Weiss AG, Cheng L-Y, Kohut P, Lu C, Varuttamaseni A, Newton T (2023) NBSR Alternative Fuel Management Schemes Analysis Procedure. (National Institute of Standards and Technology, Gaithersburg, MD), NBSR-0018-DOC-00.
- [14] MITR STAFF (2011) Safety Analysis Report for the MIT Research Reactor.
- [15] Costa J (1969) Friction coefficient measurement in turbulent flow, simple phase with heat transfer, in a rectangular channel. (France), Note CEA-N-1142, p 21. Available at http://inis.iaea.org/search/search.aspx?orig_q=RN:49041845
- [16] Saha P, Zuber N (1974) Point of Net Vapor Generation and Vapor Void Fraction in Subcooled Boiling. *Proceeding of International Heat Transfer Conference 5* (Begellhouse, Tokyo, Japan), pp 175–179. <https://doi.org/10.1615/IHTC5.430>
- [17] Bergles A, Rohsenow W (1964) The determination of forced-convection surface-boiling heat transfer.
- [18] ISL (2019) RELAP5/MOD3.3 Code Manual. (Information Systems Laboratories, Inc., Rockville, MD and Idaho Falls, ID).
- [19] Wilcox DC (1998) *Turbulence modeling for CFD* (DCW industries La Canada, CA), Vol. 2.
- [20] Versteeg HK, Malalasekera W (2007) *An introduction to computational fluid dynamics: the finite volume method* (Pearson Education Ltd., Harlow, England), 2nd ed.
- [21] Kolmogorov AN (1941) The local structure of turbulence in incompressible viscous fluid for very large Reynolds. *Numbers In Dokl Akad Nauk SSSR* 30:301.
- [22] Kolmogorov AN (1941) On degeneration (decay) of isotropic turbulence in an incompressible viscous liquid., Vol. 31, pp 538–540.
- [23] Kolmogorov AN (1941) Dissipation of energy in the locally isotropic turbulence., Vol. 32, pp 19–21.
- [24] Kolmogorov AN (1962) A refinement of previous hypotheses concerning the local structure of turbulence in a viscous incompressible fluid at high Reynolds number. *Journal of Fluid Mechanics* 13(1):82–85.
- [25] Girimaji SS (2006) Partially-averaged Navier-Stokes model for turbulence: A Reynolds-averaged Navier-Stokes to direct numerical simulation bridging method.
- [26] Girimaji SS, Jeong E, Srinivasan R (2006) Partially averaged Navier-Stokes method for turbulence: Fixed point analysis and comparison with unsteady partially averaged Navier-Stokes.

- [27] Launder BE, Sharma BI (1974) Application of the energy-dissipation model of turbulence to the calculation of flow near a spinning disc. *Letters in heat and mass transfer* 1(2):131–137.
- [28] Pope SB (2000) *Turbulent Flows* (Cambridge University Press).
- [29] Launder BE, Spalding DB (1974) The numerical computation of turbulent flows. *Computer Methods in Applied Mechanics and Engineering* 3(2):269–289.
[https://doi.org/10.1016/0045-7825\(74\)90029-2](https://doi.org/10.1016/0045-7825(74)90029-2)
- [30] El-Tahry SH (1983) K-epsilon equation for compressible reciprocating engine flows. *J Energy;(United States)* 7.
- [31] Wilcox DC (1988) Reassessment of the scale-determining equation for advanced turbulence models. *AIAA journal* 26(11):1299–1310.
- [32] Kolmogorov AN (1941) Equations of turbulent motion in an incompressible fluid., Vol. 30, pp 299–303.
- [33] Menter FR (1994) Two-equation eddy-viscosity turbulence models for engineering applications. *AIAA journal* 32(8):1598–1605.
- [34] Menter FR, Kuntz M, Langtry R (2003) Ten years of industrial experience with the SST turbulence model. *Turbulence, heat and mass transfer* 4(1):625–632.
- [35] Johnson DA, King L (1985) A mathematically simple turbulence closure model for attached and separated turbulent boundary layers. *AIAA journal* 23(11):1684–1692.
- [36] Shih T-H, Zhu J, Lumley JL (1994) A new Reynolds stress algebraic equation model.
- [37] Shih T-H, Zhu J, Lumley JL (1995) A new Reynolds stress algebraic equation model. *Computer methods in applied mechanics and engineering* 125(1–4):287–302.
- [38] Fradeneck AD, Kimber ML (2020) Applicability of Common RANS Models for the Calculation of Transient Forced to Natural Convection. *Journal of Verification, Validation and Uncertainty Quantification* 5(2).
- [39] Spalart P, Allmaras S (1992) A one-equation turbulence model for aerodynamic flows., p 439.
- [40] Dacles-Mariani J, Zilliac GG, Chow JS, Bradshaw P (1995) Numerical/experimental study of a wingtip vortex in the near field. *AIAA journal* 33(9):1561–1568.
- [41] Schlichting H, Gersten K (2016) *Boundary-layer theory* (springer).
- [42] Weiss AG, Kristo PJ, Gonzalez JR, Kimber ML (2022) Flow regime and Reynolds number variation effects on the mixing behavior of parallel flows. *Experimental Thermal and Fluid Science* 134:110619.

- [43] Weiss AG, Shen JS, Gurgun A (2023) A Turbulence Model Sensitivity Analysis on the Hydraulic Behavior in the Inlet Plenum of the Proposed NIST Neutron Source Design. *Proceedings of NURETH-20* (American Nuclear Society, Washington, DC), pp 794–807.
- [44] Diamond DJ, Baek JS, Hanson AL, Cheng L-Y, Brown N, Cuadra A (2015) Conversion Preliminary Safety Analysis Report for the NIST Research Reactor., BNL--107265-2015-IR, 1169032, p BNL--107265-2015-IR, 1169032. <https://doi.org/10.2172/1169032>
- [45] Mauricio E. Tano (2022) Margin to Onset of Nucleate Boiling studies for MITR and NBSR Design Demonstration Elements. (Idaho National Lab.(INL), Idaho Falls, ID (United States)), INL/RPT-22-69810.
- [46] Nuclear Regulatory Commission, Washington, DC (United States). Office of Nuclear Reactor Regulation (1996) Guidelines for preparing and reviewing applications for the licensing of non-power reactors: Standard review plan and acceptance criteria., NUREG-1537 Pt.2, 211545. <https://doi.org/10.2172/211545>
- [47] Xu Y, Peng M, Xia G, Shang H (2021) Optimization of forced circulation to natural circulation transition characteristics of IPWR. *Annals of Nuclear Energy* 157:108249.
- [48] Shen J, Weiss AG, Gurgun A, Baroukh IR (2023) A Turbulence Model Sensitivity Analysis of Thermal-Hydraulic Properties on the Pre-conceptual NIST Neutron Source Design. *Proceedings of the International Conference on Nuclear Engineering* (The Japan Society of Mechanical Engineers (JSME), Kyoto, Japan). <https://doi.org/10.1299/jsmeicone.2023.30.1211>
- [49] Baroukh IR, Gurgun A, Shen JS, Weiss AG (2022) A Preliminary Thermal-hydraulics Analysis for the NIST Neutron Source. *Transactions of the American Nuclear Society* (Phoenix, AZ).
- [50] Weiss, Abdullah G., Gurgun, Anil, Baroukh, Idan R., Shen, Joy (2023) Sensitivity Analyses of the Thermal-hydraulics Safety Margins in the Proposed NIST Neutron Source Design. *Proceedings of the International Conference on Nuclear Engineering* (The Japan Society of Mechanical Engineers (JSME), Kyoto, Japan). <https://doi.org/10.1299/jsmeicone.2023.30.1223>
- [51] Gurgun A, Weiss A, Shen J (2023) Thermal-hydraulic Assessment of the Proposed NIST Neutron Source Design. *Proceedings of NURETH-20* (American Nuclear Society, Washington, DC), pp 1382–1393.
- [52] Ha T, Garland WJ (2006) Hydraulic study of turbulent flow in MTR-type nuclear fuel assembly. *Nuclear Engineering and Design* 236(9):975–984.
- [53] ASME (2021) ASME V&V 20-2009 (R2021) - Standard for Verification and Validation in Computational Fluid Dynamics and Heat Transfer.
- [54] Oberkampf WL, Roy CJ (2010) *Verification and validation in scientific computing* (Cambridge university press).

- [55] Weiss AG, Zaidan LJ, Bani Ahmad MT, Abdoelatef MG, Peterson JW, Lindsay AD, Kong F, Ahmed K, Kimber ML (2022) Characterization of the Finite Element Computational Fluid Dynamics Capabilities in the Multiphysics Object Oriented Simulation Environment. *Journal of Nuclear Engineering and Radiation Science* 9(2):021402.

Appendix A. Pump Characteristics

The following equations are used by TRACE to model pump head and adapted from TRACE V5.0 Theory Manual (REF HERE):

$$H = \text{the pump head, } (\Delta P)/\rho_m \text{ (Pa} - \frac{m^3}{kg}, \frac{m^2}{s^2}, \text{ or } N - m/kg)$$

$$Q = \text{the impeller-interface volumetric flow rate (} m^3/s)$$

$$\Omega = \text{the pump-impeller angular velocity (rad/s)}$$

where ΔP is the pressure rise across the pump-impeller interface and ρ_m is the impeller-interface upstream coolant-mixture density. The normalized quantities are

$$h = H/c$$

$$q = Q/Q_R$$

$$\omega = \Omega/\Omega_R$$

where H_R is the rated head, Q_R is the rated volumetric flow, and Ω_R is the rated pump-impeller rotational speed. The pump similarity relations are

$$h/\omega^2 = f(q/\omega)$$

and

$$h/q^2 = f(\omega/q)$$

for small ω values.

Based on the values, the pump curve is divided into four segments. Each segment has its own curves to calculate the similarity relation.

Table 21. Pump curve segments for homologous curves (Adapted from [1])

Curve Segment	$ \frac{q}{\omega} $	ω	q	Correlation
1	≤ 1	> 0	N/A	$h/\omega^2 = f(q/\omega)$
4	≤ 1	< 0	N/A	
2	> 1	N/A	> 0	$h/q^2 = f(\omega/q)$
3	> 1	N/A	< 0	

To account for the effects of two-phase coolant on pump performance, the pump curves are separated into two distinct regimes. For single-phase coolant, the pump performance is defined by a void fraction of 0.0 or 1.0. At intermediate void fractions, the pump performance is defined at fully degraded conditions. For the NNS pumps, the homologous curves for the pump head are given in Figure 51, where SP is single phase and FD is fully degraded.

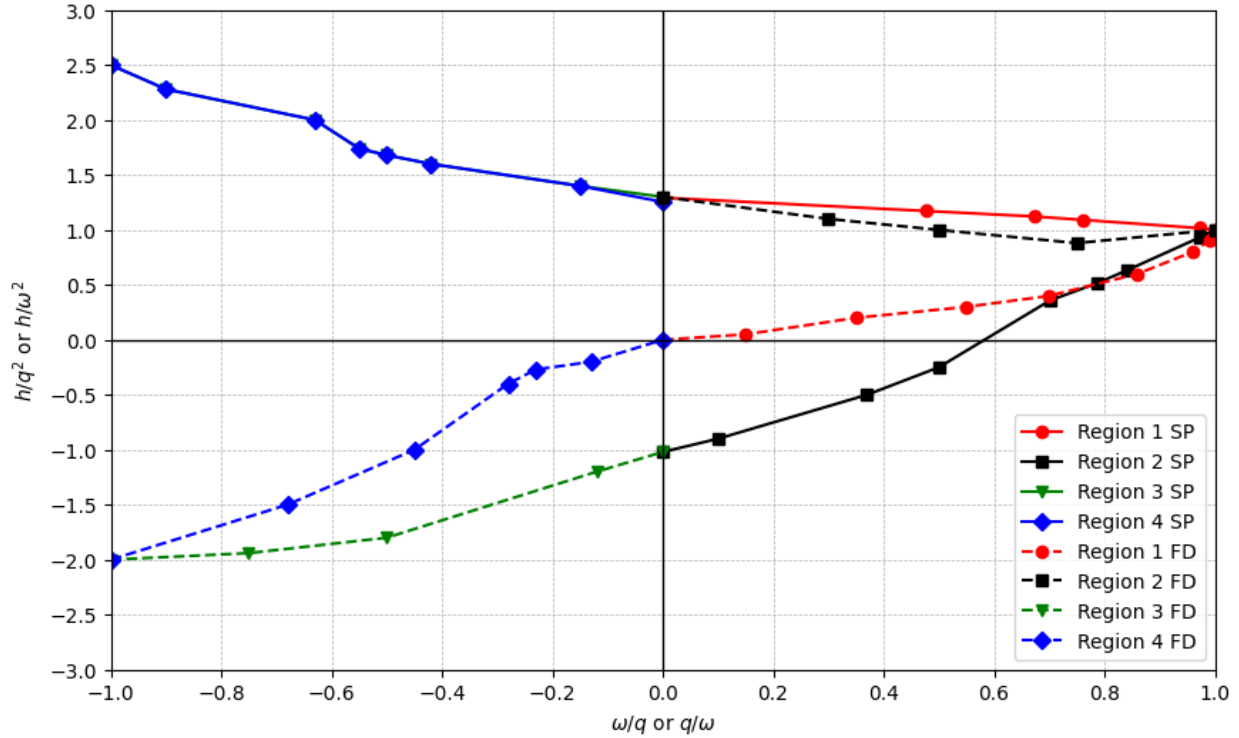


Figure 51. NNP Pumps Homologous Curves for Pump Head

The pump head at any void fraction is calculated from the relationship

$$H = H_{1\phi} - M(\alpha)[H_{1\phi} - H_{2\phi}]$$

where

H = the total pump head,

$H_{1\phi} = h_{1\phi}H_R$ = the single phase pump head,

$H_{2\phi} = h_{2\phi}H_R$ = the two phase pump head,

$M(\alpha)$ = the head degradation multiplier, and

α = the upstream void fraction.

Similar to the homologous head curves, there are homologous torque curves to calculate the pump torque. The dimensionless hydraulic curve is defined by

$$\beta = T_{hy}/T_R.$$

The hydraulic torque is represented by T_{hy} and the rated torque is represented by T_R . The dimensionless torque β can be correlated as either β/ω or β/q , like the dimensionless head h was correlated. Therefore, the similarity relations are

$$\beta/\omega^2 = f(q/\omega)$$

and

$$\beta/q^2 = f(\omega/q).$$

The same four segments and two conditions (SP and FD) are also valid for homologous curves for pump torque. For the NNS pumps, the homologous curves for the pump torque are given in Figure 52.

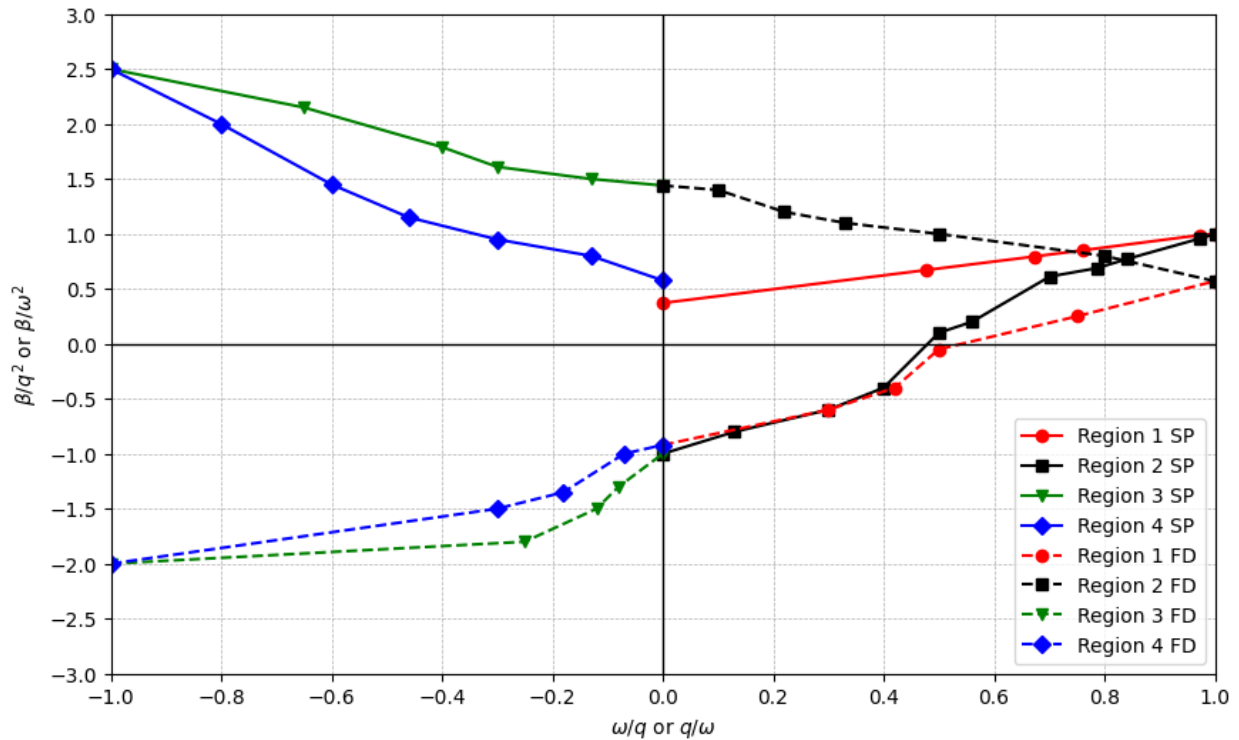


Figure 52. NNP Pumps Homologous Curves for Pump Torque.

Then the pump torque is calculated by

$$T = T_{1\phi} - N(\alpha)[T_{1\phi} - T_{2\phi}]$$

where

T = the total pump – impeller torque,

$T_{1\phi} = \beta_{1\phi}T_R(\rho_m/\rho_R)$ = the single phase pump torque,

$T_{2\phi} = \beta_{2\phi}T_R(\rho_m/\rho_R)$ = the two phase pump torque,

ρ_m = the pump upstream mixture density,

ρ_R = the rated density,

$N(\alpha)$ = the torque degradation multiplier, and

α = the upstream void fraction.

For nominal conditions, the pump-impeller angular velocity Ω is a constant value. After the pump is tripped, Ω changes as a function of the sum of moments acting on the pump. The rate of change is calculated by

$$I \frac{\partial \Omega}{\partial t} = -(T_{hy} + T_f)$$

where I is the combined moment of inertia and T_f is the torque caused by friction (bearing and windage).

The rated values of the NNS pumps are given in Table 22.

Table 22. Rated values for the NNS pumps.

Parameter	Value	Unit
H_R	476.8	m^2/s^2
T_R	425.67	$N * m$
Q_R	0.1375	m^3/s
ρ_R	1000.0	kg/m^3
Ω_R	183.3	rad/s
T_f	45.0	$N * m$

Appendix B. Behavior of NNS for Accident Scenarios with SSS Applied

B.1. Loss of Heat Sink Accident with SSS

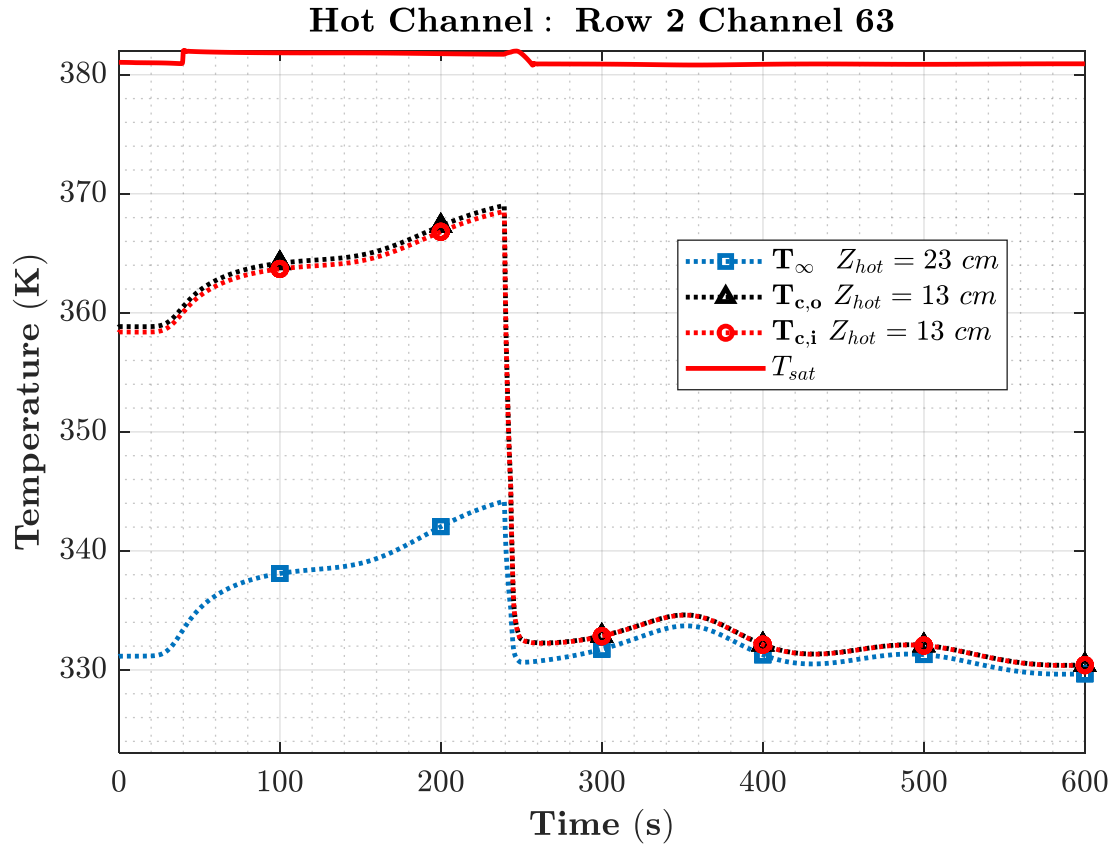


Figure 53. The temporal evolution of temperatures throughout a loss of heat sink transient with the SSS applied.

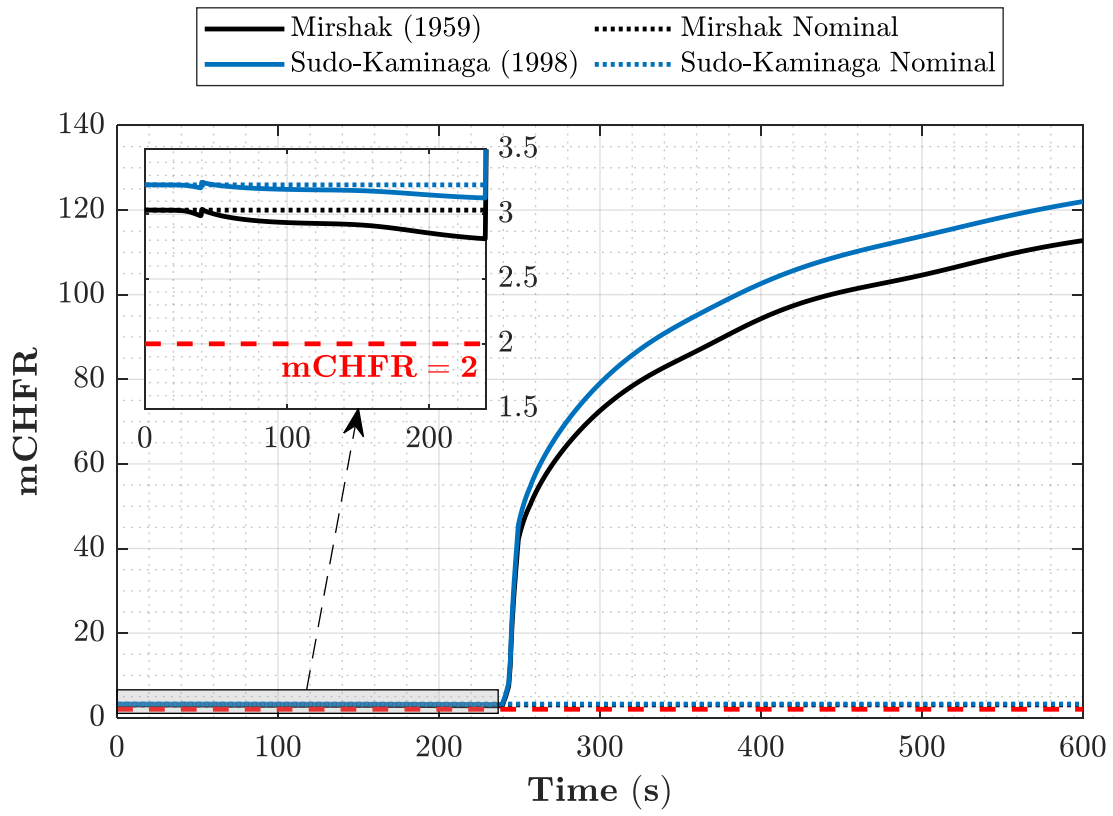


Figure 54. The temporal evolution of mCHFR throughout a loss of heat sink transient with the SSS applied.

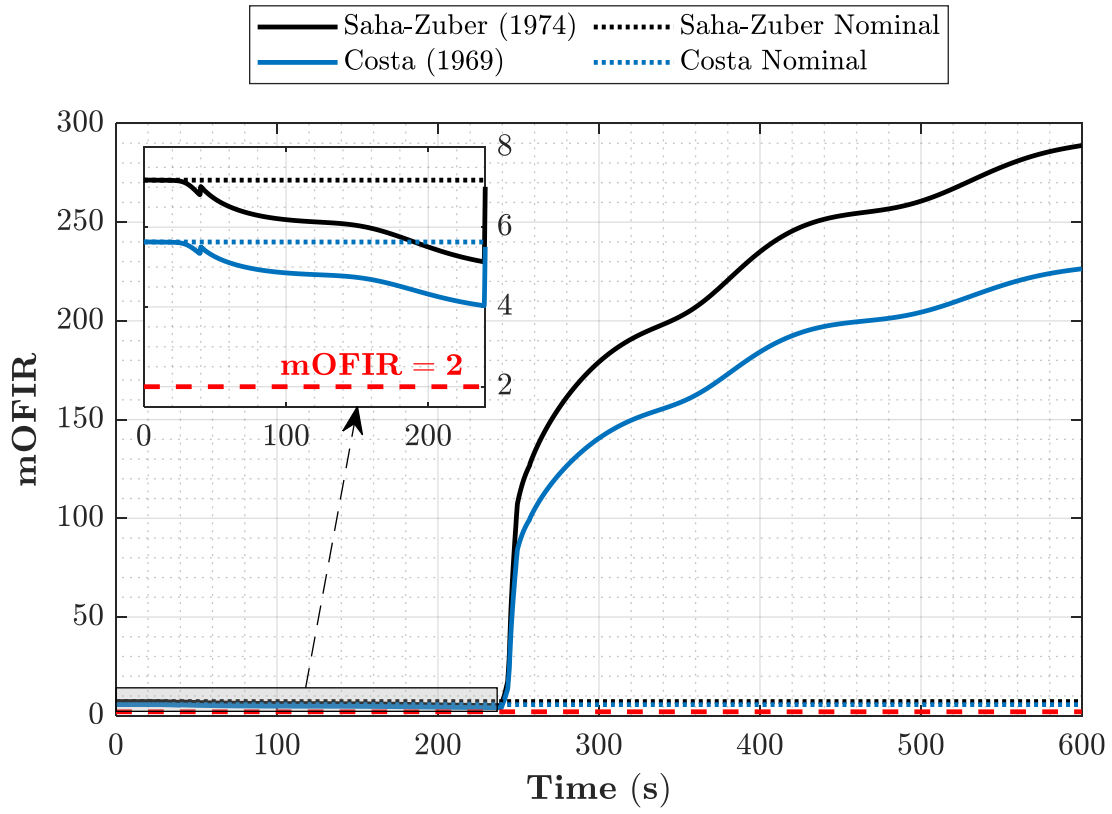


Figure 55. The temporal evolution of mOFIR throughout a loss of heat sink transient with the SSS applied.

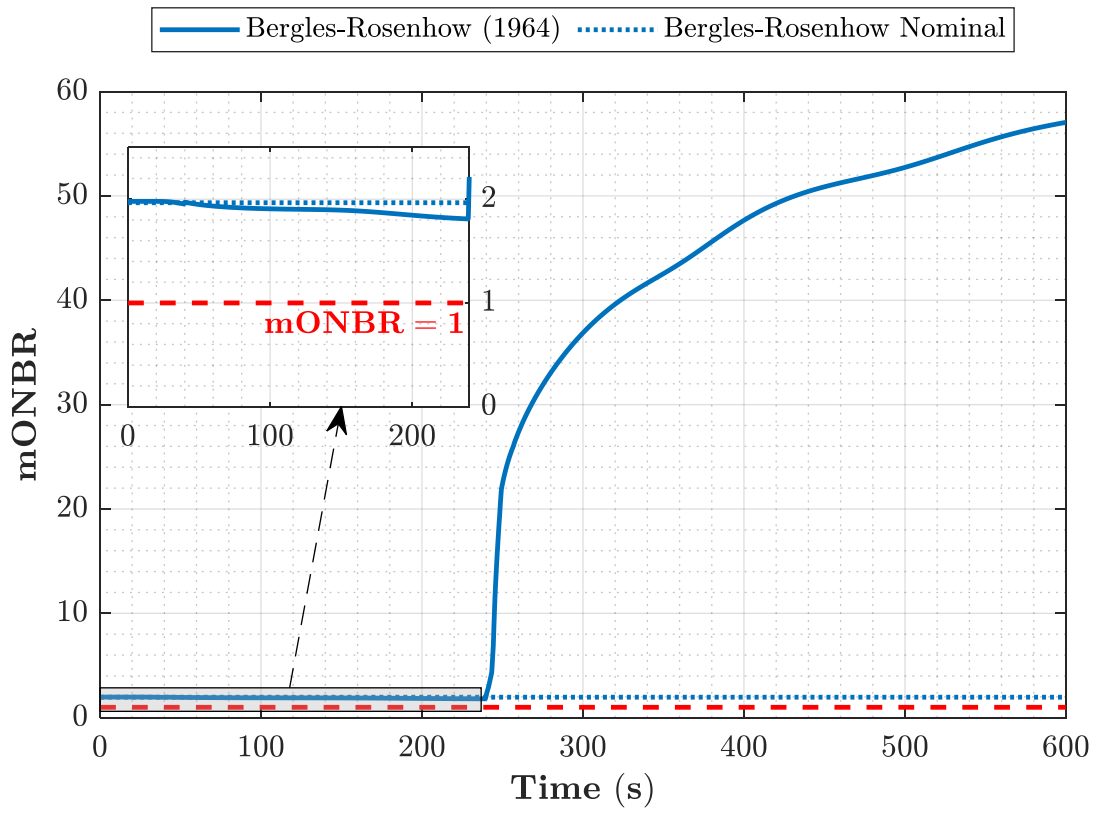


Figure 56. The temporal evolution of mONBR throughout a loss of heat sink transient with the SSS applied.

B.2. Reactivity Insertion Accident with SSS

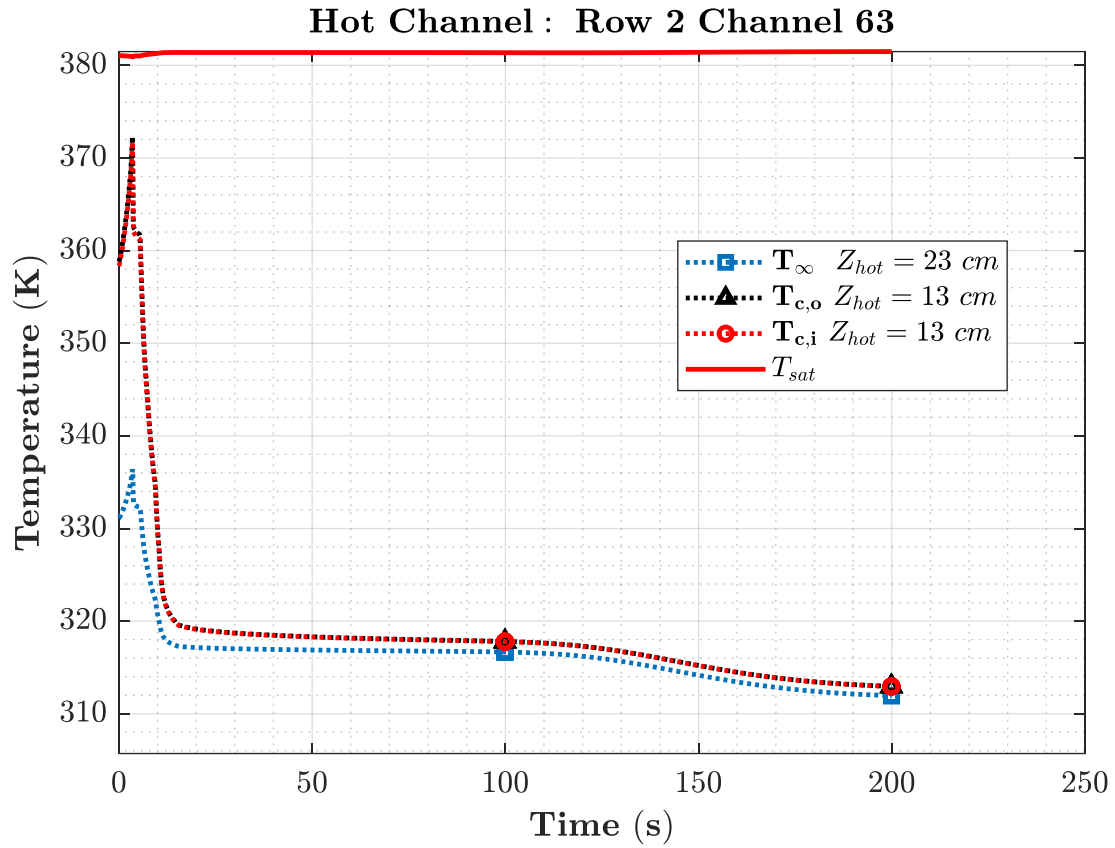


Figure 57. The temporal evolution of temperatures throughout a reactivity insertion transient with the SSS applied.

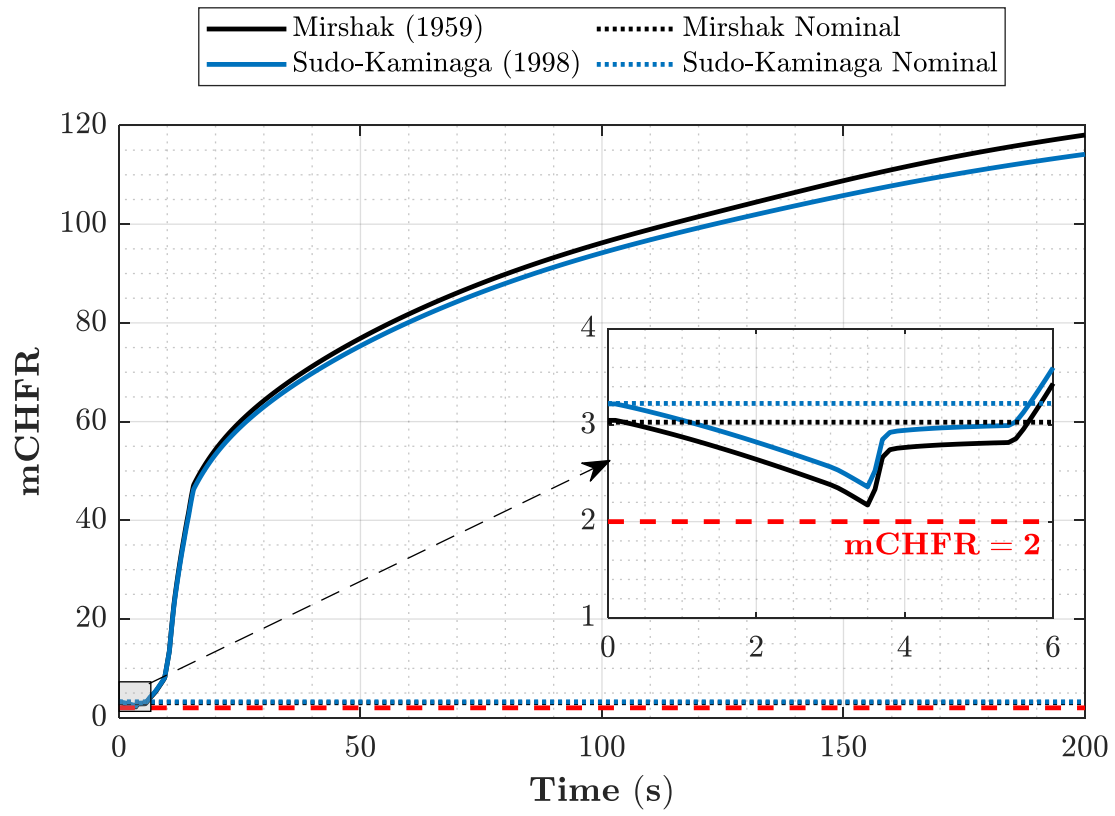


Figure 58. The temporal evolution of mCHFR throughout a reactivity insertion transient with the SSS applied.

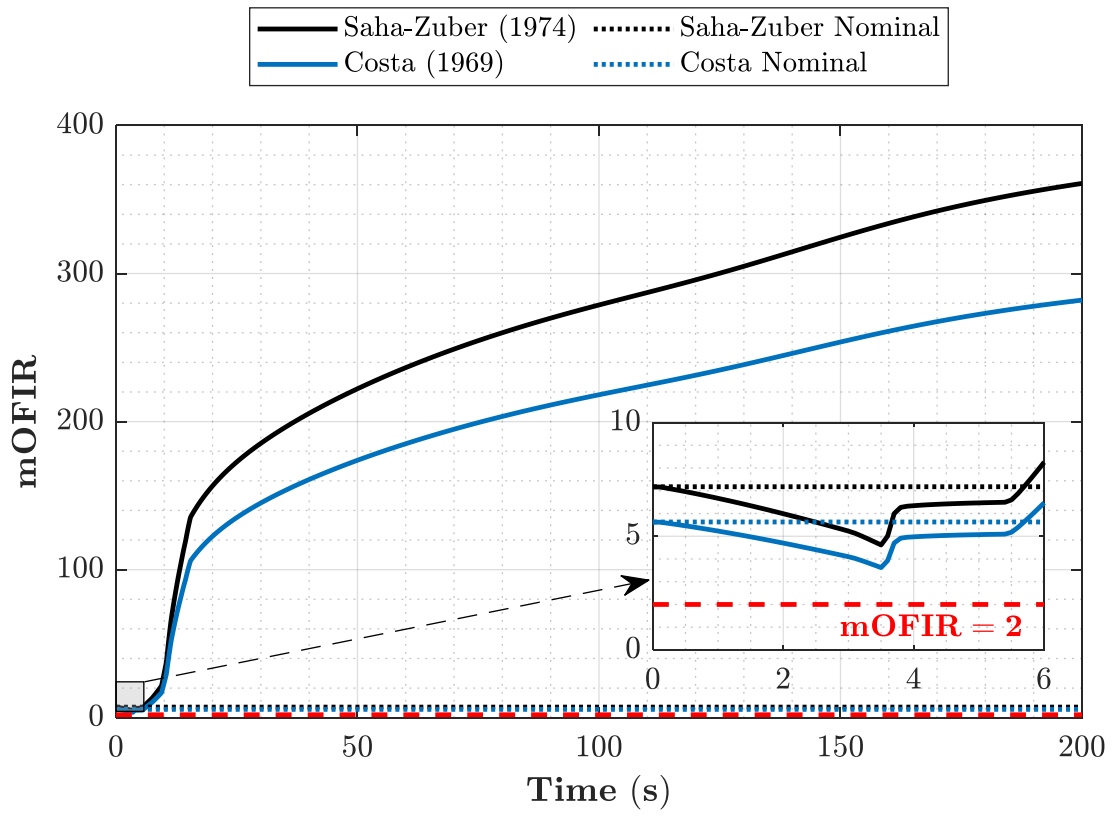


Figure 59. The temporal evolution of mOFIR throughout a reactivity insertion transient with the SSS applied.

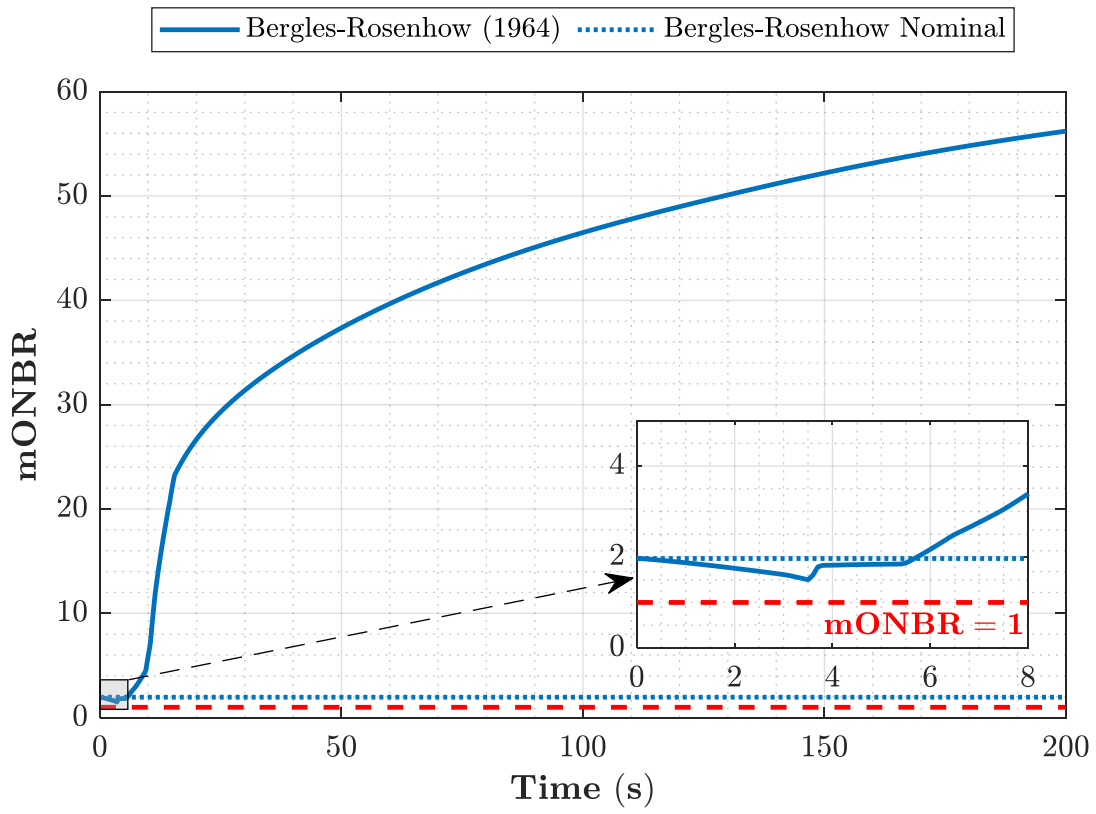


Figure 60. The temporal evolution of mONBR throughout a reactivity insertion transient with the SSS applied.

B.3. Loss of Flow Accidents with SSS

B.3.1. Seizure of One Pump

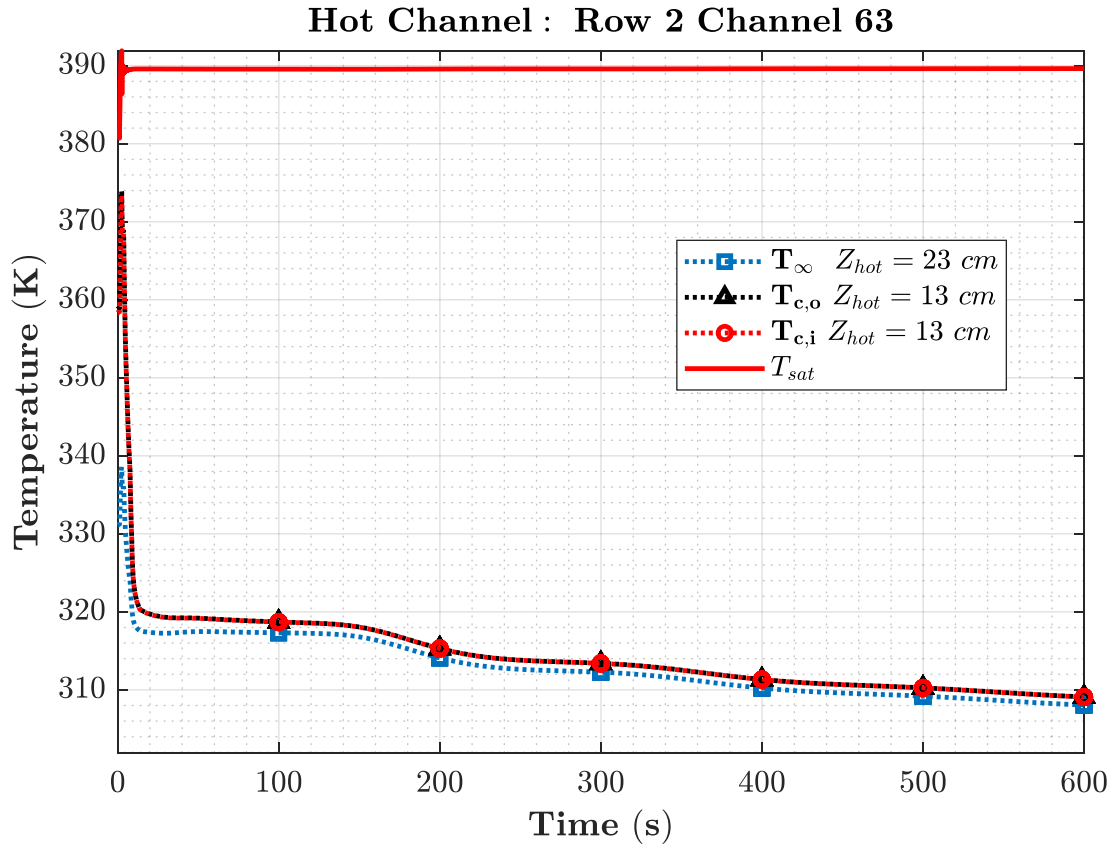


Figure 61. The temporal evolution of temperatures throughout a seizure of one pump LOFA transient with the SSS applied.

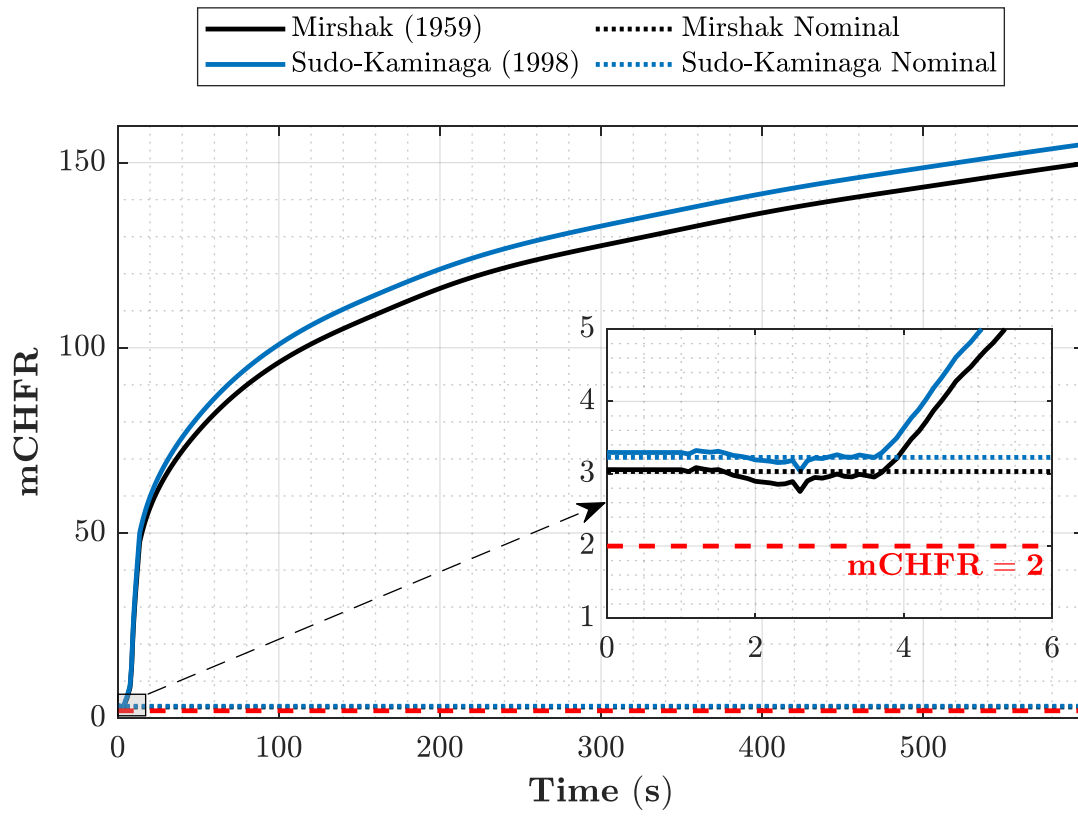


Figure 62. The temporal evolution of mCHFR throughout a seizure of one pump LOFA transient with the SSS applied.

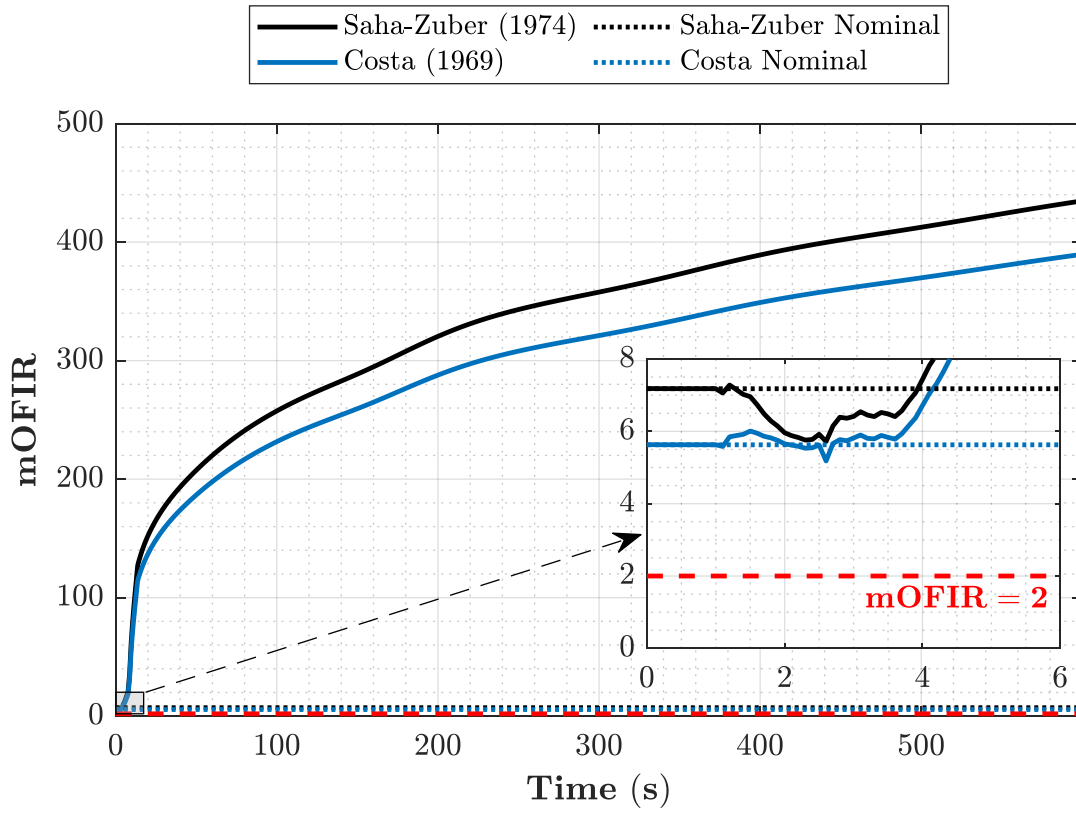


Figure 63. The temporal evolution of mOFIR throughout a seizure of one pump LOFA transient with the SSS applied.

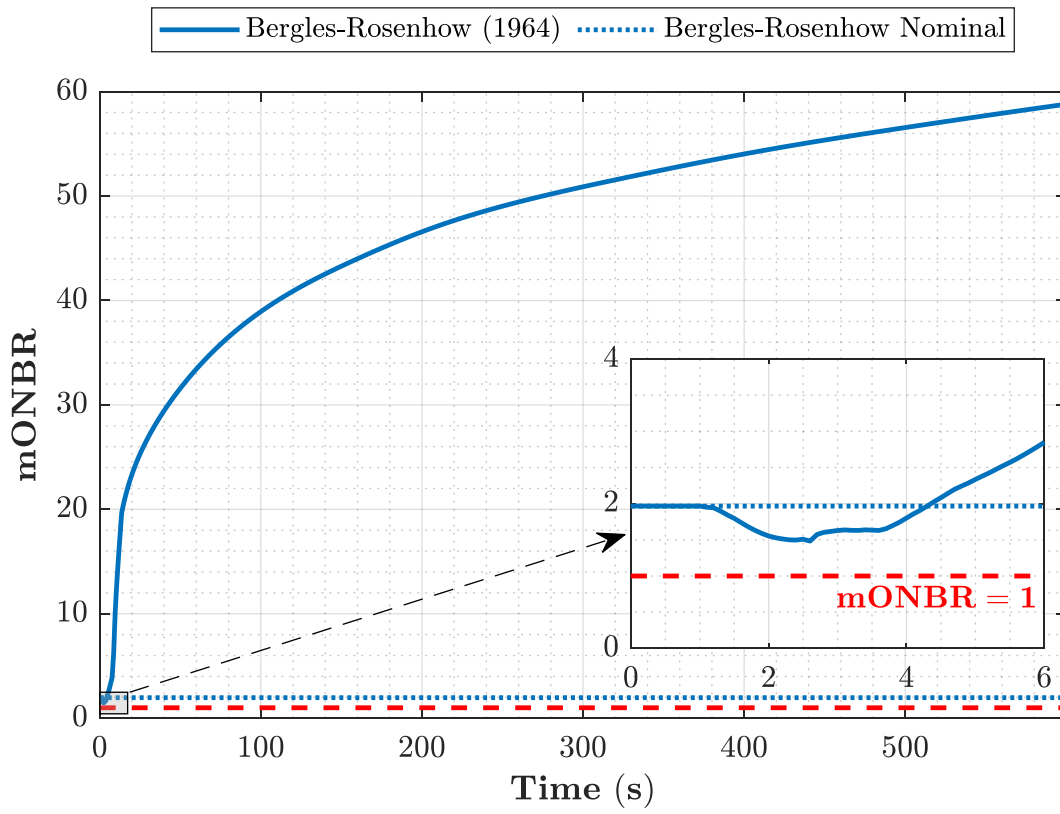


Figure 64. The temporal evolution of mONBR throughout a seizure of one pump LOFA transient with the SSS applied.

B.3.2. Loss of Two Pumps

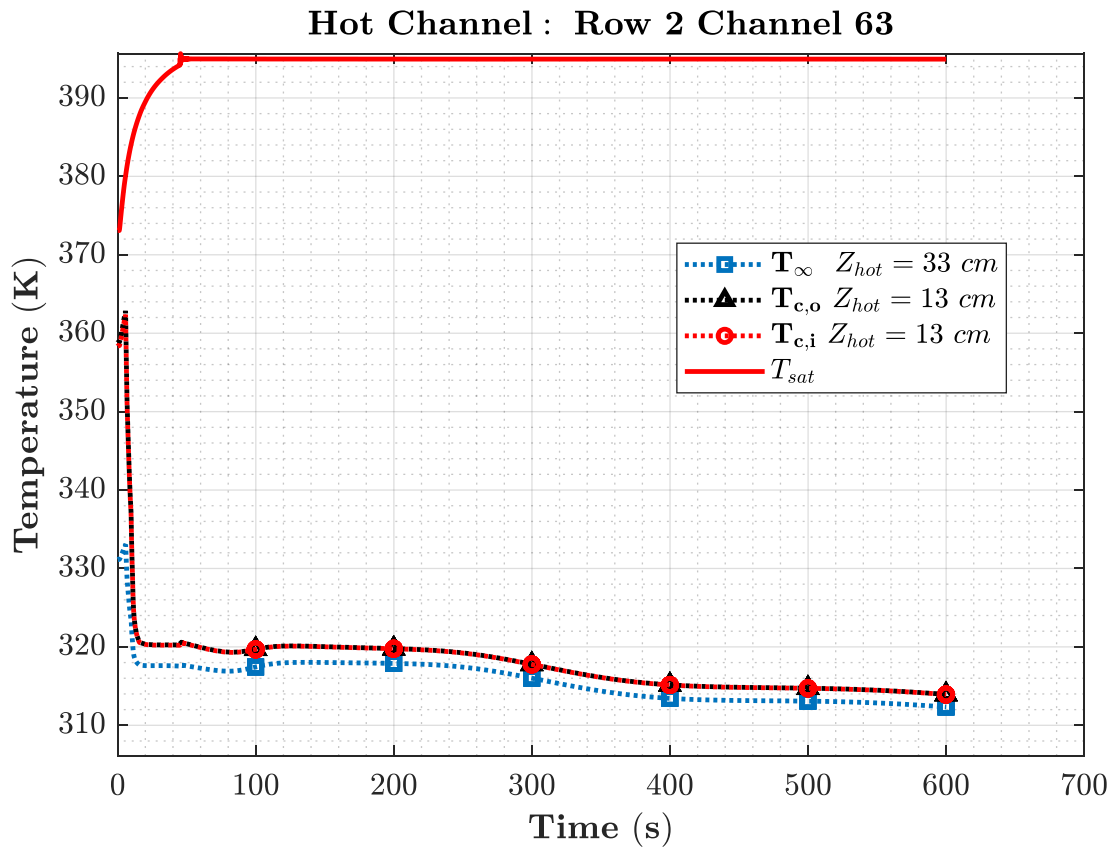


Figure 65. The temporal evolution of temperatures throughout a loss of two pumps LOFA transient with the SSS applied.

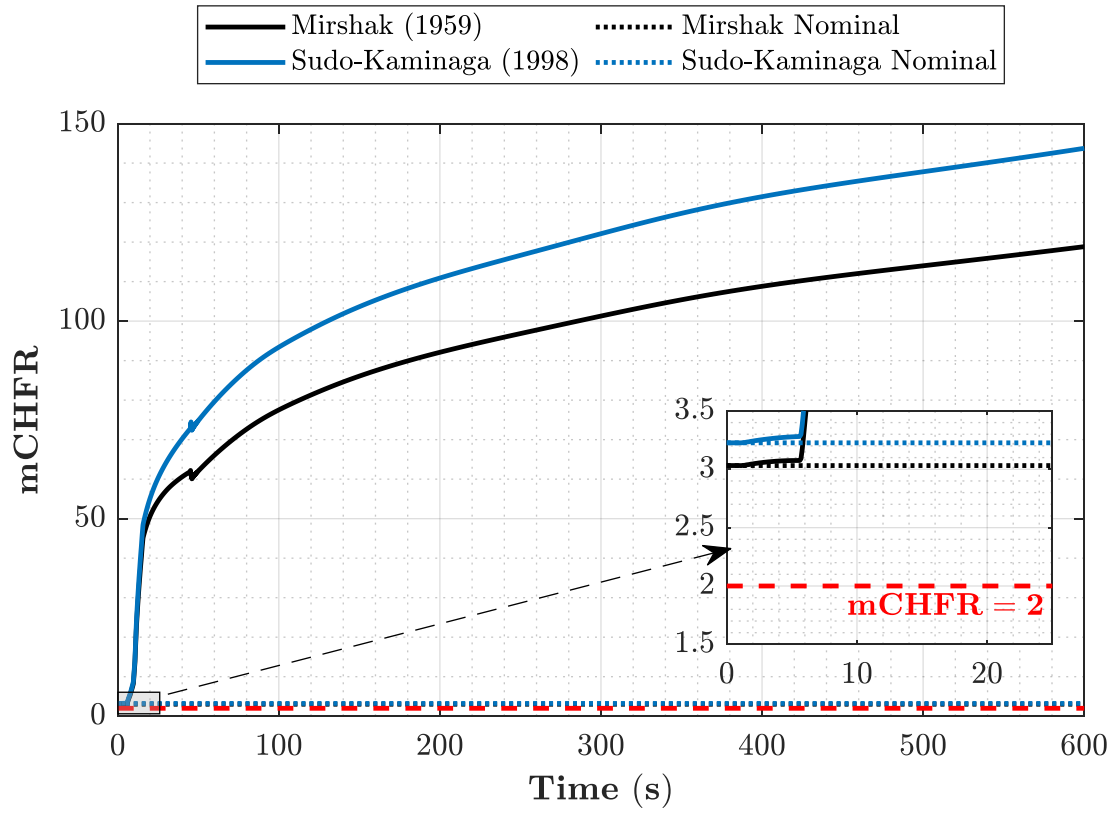


Figure 66. The temporal evolution of mCHFR throughout a loss of two pumps LOFA transient with the SSS applied.

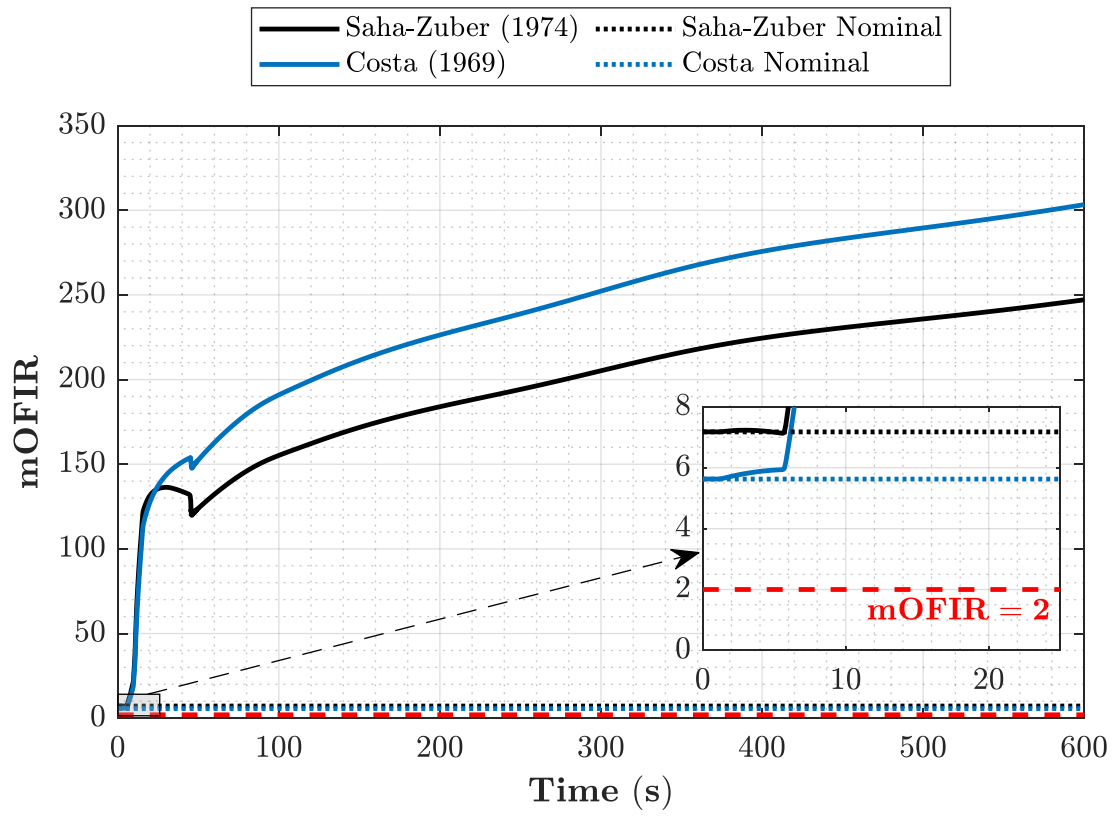


Figure 67. The temporal evolution of mOFIR throughout a loss of two pumps LOFA transient with the SSS applied.

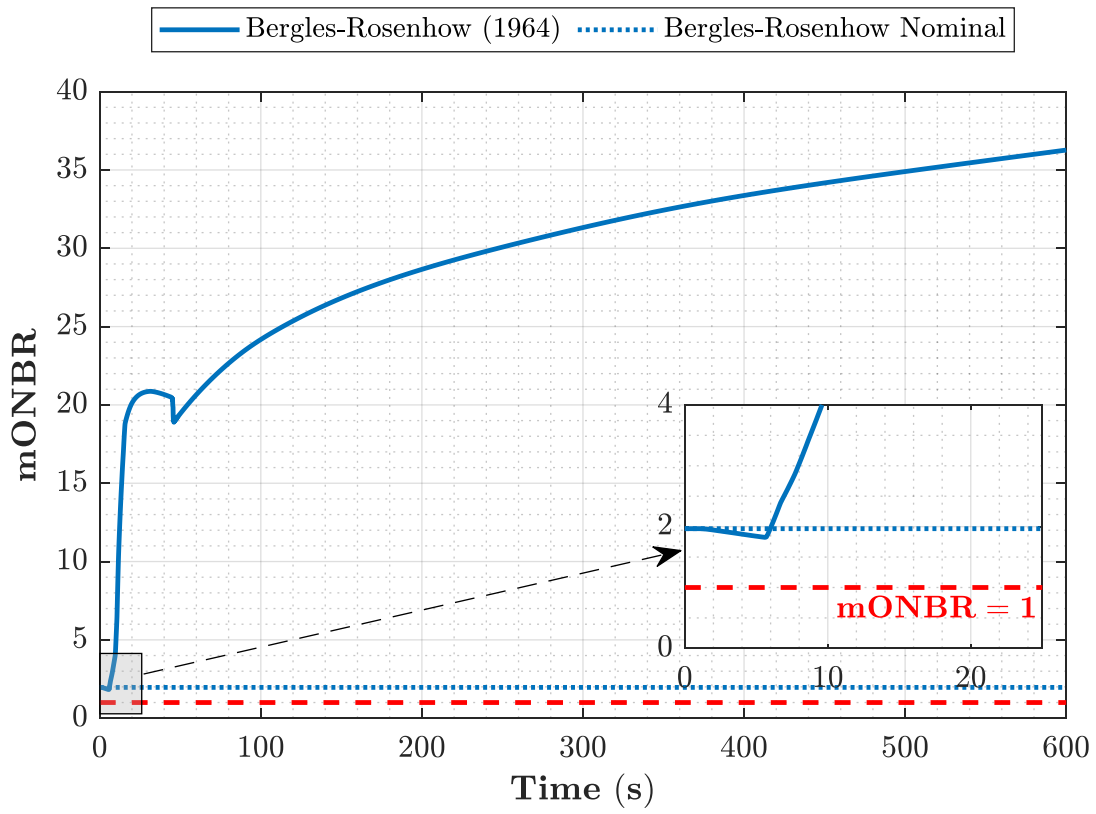


Figure 68. The temporal evolution of mONBR throughout a loss of two pumps LOFA transient with the SSS applied.

Appendix C. Mass Flow Rate in the Hot Channel for the Accidents

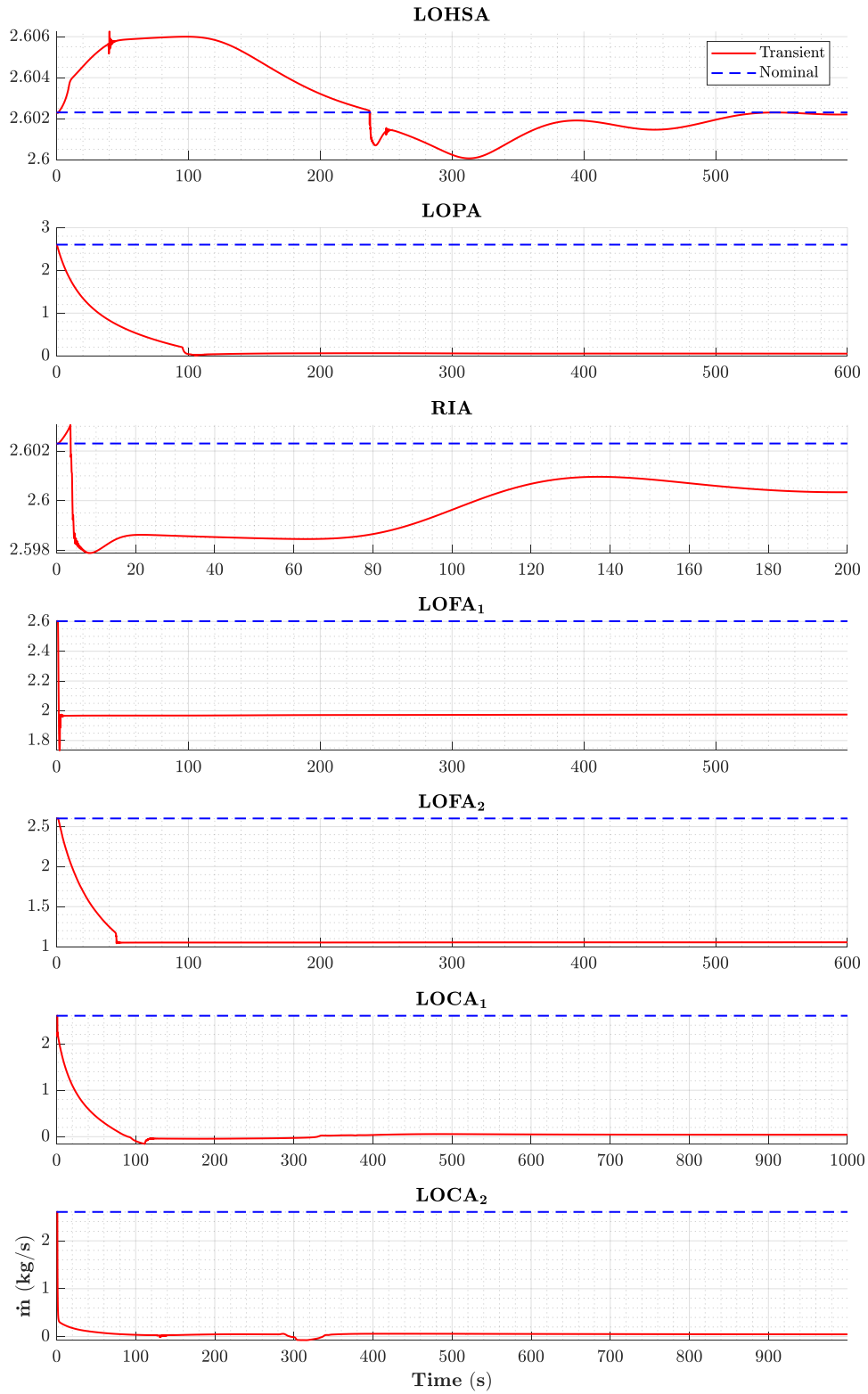


Figure 69. The mass flow rate evolution in each of the analyzed accidents with PSS applied.

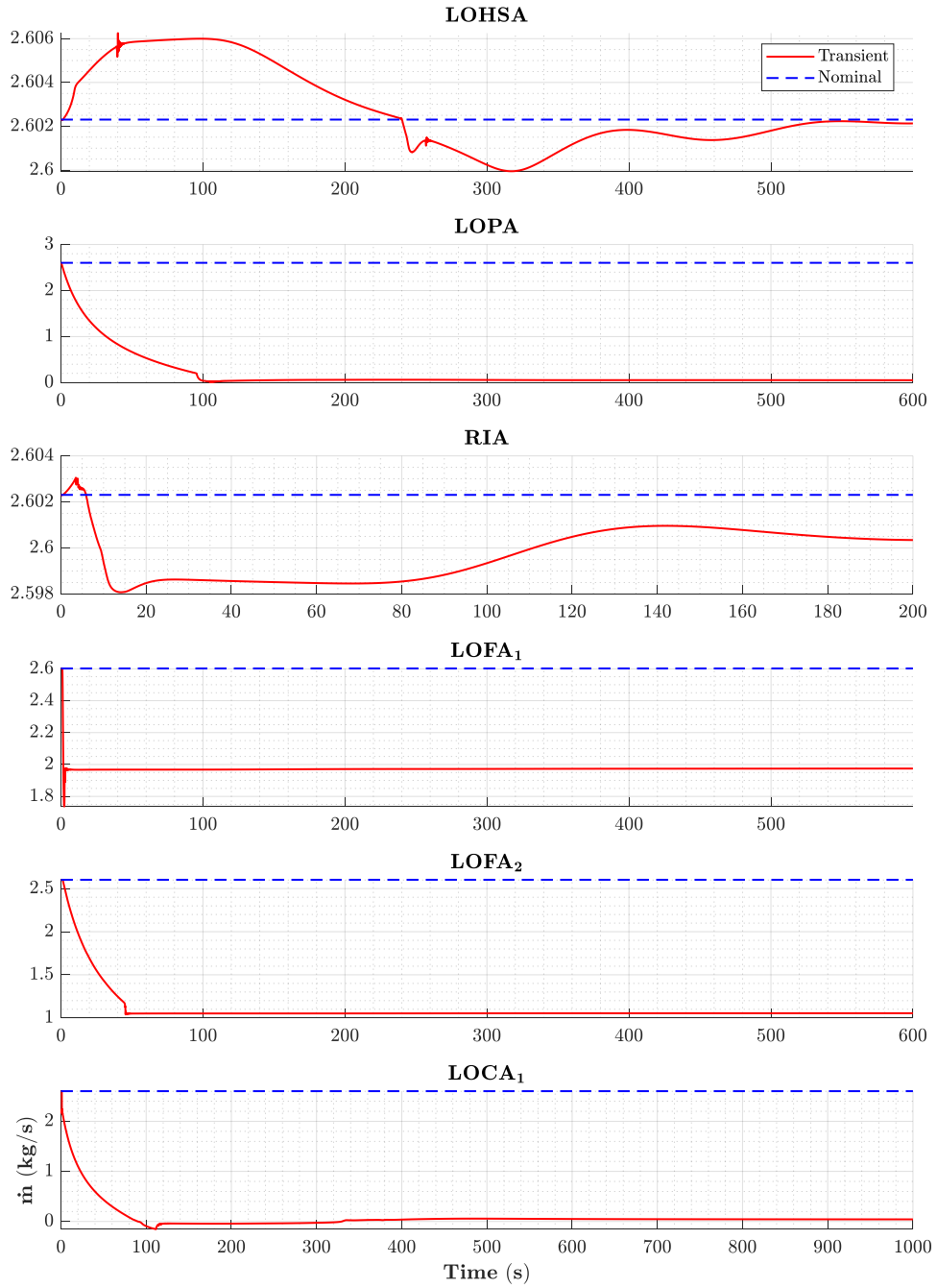


Figure 70. The mass flow rate evolution in each of the analyzed accidents with SSS applied.

Appendix D. Power Evolution for the Accidents

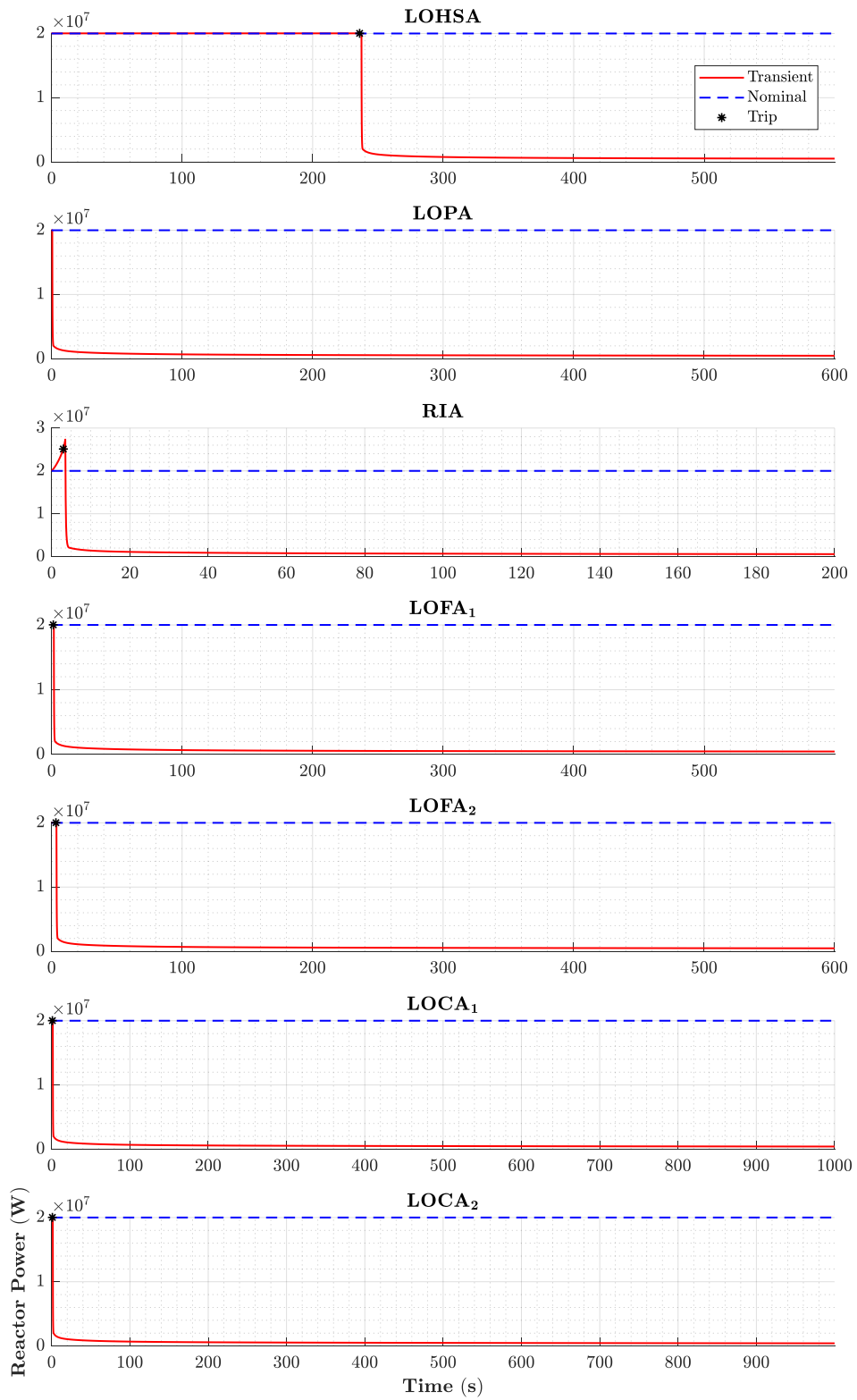


Figure 71. The reactor power evolution in each of the analyzed accidents with PSS applied.

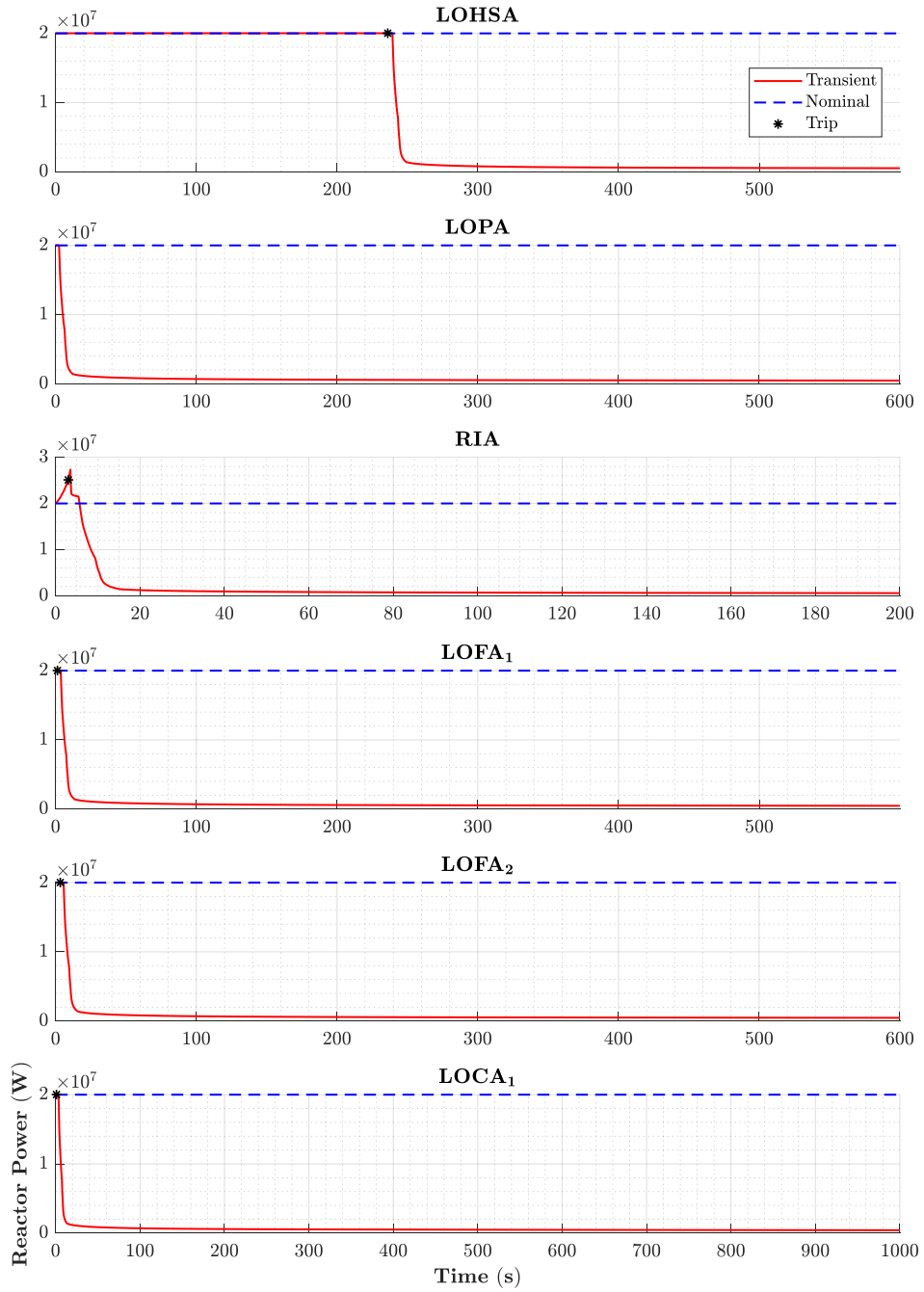


Figure 72. The reactor power evolution in each of the analyzed accidents with SSS applied.